

# Observing Simulations in the Far-Infrared

A dissertation submitted in satisfaction of the final requirement for the degree of

Doctor of Philosophy

Astronomy Program

School of Earth and Environmental Sciences

Seoul National University

Candidate:

Woong-Seob Jeong

Supervisor:

Hyung Mok Lee

June 2004



## Abstract

One of the key questions regarding the performance of space missions is the estimation of the effective detection limit for faint sources. Since the size of the sources becomes much larger in longer wavelength band, the detection limits will depend on the nature of the sources. There have been a number of simple estimates of detection limits based on the available laboratory data and the specifications of the space missions. Clearly, more realistic estimation can be made by using numerical simulations. We will carry out simulations of the observations under several different circumstances in order to obtain still more reliable detection limits which can be used to design scientific projects.

We describe the observing simulation for present or incoming infrared missions, e.g., Spitzer, ASTRO-F, Herschel, and SPICA. The observing simulation has two purposes: one is to check the specifications and performances of the mission as a whole; the other is to prepare input data sets for the data analysis softwares prior to launch. We develop the optimal algorithm for reducing the computation time of inevitable, but time-consuming, convolution processes. With the optimal algorithm, we reduce the computation time by an order of magnitude.

We investigate the instrumental noise and the confusion in the far-infrared which are most important factors contributing to the detection limits. The instrumental noise is determined by the sensitivity of the detectors and the entire telescope system. The detector used in far-infrared exhibit many characteristics. We examine the effects of the sampling, transients, glitches caused by cosmic ray hits, and the crosstalk of the far-infrared detector arrays. We used simple model fits to laboratory measurements for the transients and glitch profiles. On the other hand, confusion noise is dependent upon the astronomical observations and makes the fluctuations of the background brightness caused by the intrinsically discrete extragalactic sources (source confusion) and the structures of the Galactic cirrus (sky confusion). The confusion plays important roles in limiting the astronomical observations, even though we extend the exposure time indefinitely.

In order to quantitatively assess the effect of this background emission on the detection of point sources for current and future far-infrared observations, we have extended the Galactic emission map to higher resolution than the currently accessible scale. Using this high resolution map, we estimate the sky confusion noise due to the emission from interstellar dust clouds or cirrus, based on fluctuation analysis as well as carrying out photometry over realistically simulated images. We find that the confusion noise derived by this fluctuation analysis agrees well with the result from realistic simulations, when we take the parameter in the fluctuation analysis related to background estimation parameter in the photometry to be the same value. Though the confusion noise becomes dominant in long wavelength bands ( $> 100 \mu\text{m}$ ) for each space mission, the confusion due to cirrus structure is expected to be much less significant for the next generation of the space missions with larger aperture sizes (e.g. Herschel and SPICA) than the estimate from the observation data.

In addition to the instrumental noise and the sky confusion, we probe the source confusion, which mainly depends on the source distribution and the telescope beam size. In the source distribution, we obtain the model including no evolution, weak evolution, and the strong evolution. We estimate the expected redshift distributions for each space mission. From the power spectrum analysis on the simulated images including the faint unresolved sources and the cirrus background as well, we show the fluctuation for the Poissonian source distribution and cirrus structure below the detection limit, and estimate the predicted cosmic far-infrared background.

*Keywords:* cosmology: observations — infrared: galaxies — galaxies: evolution — methods: data analysis — techniques: image processing — ISM: structure — galaxies: photometry — Infrared: ISM

# Contents

<b>Abstract</b>	<b>i</b>
<b>1 Overview of the Observing Simulations</b>	<b>1</b>
1.1 Introduction . . . . .	1
1.2 Optimal Algorithm for Observing Simulations . . . . .	2
1.3 Observing Simulation for Survey Mode . . . . .	3
1.4 Sky Confusion Due to Cirrus . . . . .	3
1.5 Source Confusion . . . . .	5
1.5.1 Source Counts and Evolution Model . . . . .	7
1.5.2 Cosmic Far-Infrared Background . . . . .	8
References . . . . .	9
<b>2 ASTRO-F/FIS Observing Simulation: Detection Limits for Point Sources<sup>†</sup></b>	<b>11</b>
Abstract . . . . .	11
2.1 Introduction . . . . .	12
2.2 Structure of FISVI Software . . . . .	14
2.3 Image Reconstruction . . . . .	16
2.4 Estimations of FIS Performance . . . . .	16
2.4.1 Detection Limits for a Single Point Source . . . . .	18
2.4.2 Simulations with Distributed Point Sources and Realistic Detector Configurations . . . . .	22
2.4.3 Realistic Simulations . . . . .	25

2.5	Summary . . . . .	36
	References . . . . .	39
<b>3</b>	<b>Change of Sampling Rate in Scan Mode Observation<sup>‡</sup></b>	<b>41</b>
	Abstract . . . . .	41
3.1	INTRODUCTION . . . . .	42
3.2	THE FIS VIRTUAL INSTRUMENT PROGRAM (FISVI) . . . . .	42
3.2.1	Overview . . . . .	42
3.2.2	Optics and Detector Response . . . . .	44
3.2.3	Input Data . . . . .	45
3.2.4	Detector and Readout . . . . .	49
3.3	RESULTING IMAGES . . . . .	49
3.4	DISCUSSIONS . . . . .	50
3.4.1	Effects of Sampling Rate . . . . .	50
3.4.2	Future Work . . . . .	52
	References . . . . .	55
<b>4</b>	<b>ASTRO-F/FIS Observing Simulation Including Detector Characteristics<sup>§</sup></b>	<b>57</b>
	Abstract . . . . .	57
4.1	INTRODUCTION . . . . .	57
4.2	DETECTOR RESPONSE . . . . .	58
4.3	MODELING OF DETECTOR RESPONSE . . . . .	59
4.3.1	Transients . . . . .	59
4.3.2	Stationary Crosstalk . . . . .	61
4.3.3	Glitches . . . . .	61
4.4	RESULTS . . . . .	62
4.4.1	Simulation Data . . . . .	62
4.4.2	Correction for the Detector Characteristics . . . . .	63
4.5	SUMMARY . . . . .	67
	References . . . . .	69

<b>5</b>	<b>Simulations of Cosmological Observations with ASTRO-F/FIS<sup>a</sup></b>	<b>71</b>
	Abstract . . . . .	71
	5.1 INTRODUCTION . . . . .	72
	5.2 SOFTWARE STRUCTURE . . . . .	73
	5.3 POINT SOURCE CATALOGUE . . . . .	73
	5.3.1 Galaxy Evolution Models . . . . .	73
	5.3.2 Source Distribution . . . . .	75
	5.4 GALAXY SOURCE COUNTS RESULTS . . . . .	77
	5.5 DISCUSSION . . . . .	80
	References . . . . .	83
<b>6</b>	<b>Sky Confusion Due to Galactic Cirrus<sup>b</sup></b>	<b>85</b>
	Abstract . . . . .	85
	6.1 INTRODUCTION . . . . .	86
	6.2 CONFUSION DUE TO SKY FLUCTUATION . . . . .	87
	6.3 GENERATION OF CIRRUS MAP . . . . .	90
	6.3.1 Fluctuations at Higher Spatial Resolution . . . . .	90
	6.3.2 Dust Emission at Other Wavelengths . . . . .	95
	6.4 STATISTICAL ANALYSIS FOR SKY CONFUSION NOISE . . . . .	98
	6.4.1 Selected Regions . . . . .	100
	6.4.2 Estimation of Sky Confusion Noise . . . . .	103
	6.5 PHOTOMETRIC MEASUREMENTS OF SKY CONFUSION NOISE . . . . .	114
	6.5.1 Source Distribution . . . . .	115
	6.5.2 Source Detection . . . . .	116
	6.6 INCLUSION OF INSTRUMENTAL NOISE . . . . .	121
	6.7 SUMMARY AND DISCUSSION . . . . .	122
	References . . . . .	127
<b>7</b>	<b>Probing Confusion Including Source Confusion<sup>#</sup></b>	<b>131</b>
	Abstract . . . . .	131
	7.1 INTRODUCTION . . . . .	132

7.2	SOURCES OF CONFUSION FOR EXTRAGALACTIC SURVEYS . . .	133
7.2.1	Confusion due to Infrared Cirrus . . . . .	133
7.2.2	Confusion due to Extragalactic Sources . . . . .	134
7.3	THE INPUT CATALOGUES AND SIMULATED IMAGES . . . . .	137
7.4	SIMULATION RESULTS FOR CONFUSION . . . . .	141
7.4.1	Definition by ‘Beams per Source’ . . . . .	141
7.4.2	Definition by Fluctuation . . . . .	145
7.4.3	Definition by Composition of Fluctuation and Photometry . . .	146
7.4.4	Predicted Confusion Limits for Current and Future Missions . .	148
7.5	EXPECTED RESULTS . . . . .	151
7.5.1	Expected Redshift Distribution . . . . .	151
7.5.2	Expected Cosmic Far-Infrared Background . . . . .	152
7.6	CONCLUSIONS . . . . .	156
	References . . . . .	161
<b>8</b>	<b>Conclusions</b>	<b>165</b>
<b>A</b>	<b>Optimal Convolution</b>	<b>169</b>
A.1	Compiled PSF . . . . .	169
A.1.1	PSF Convolution . . . . .	169
A.1.2	Filter Transmittance and Detector Response . . . . .	171
A.1.3	Improved PSF Convolution . . . . .	172
A.1.4	Compiled PSF . . . . .	177
A.1.5	Spectral Energy Distribution of the Sources . . . . .	177
<b>B</b>	<b>Simulation for Scan Mode Observation</b>	<b>183</b>
B.1	Procedures of Scanning and Data Sampling . . . . .	183
B.2	Integrating over the Detector Pixel . . . . .	184

# List of Figures

1.1	All-sky dust map at 100 $\mu\text{m}$ . . . . .	4
2.1	Flow charts of Simulation Software . . . . .	15
2.2	Example of a series of readout values . . . . .	17
2.3	Schematic figure for image reconstruction . . . . .	18
2.4	Assumed background emissions . . . . .	20
2.5	Comparison between the Compiled PSF and the beam pattern . . . . .	26
2.6	Simulated images for ASTRO-F/FIS . . . . .	28
2.7	Flux ratio in LW bands without noise . . . . .	29
2.8	Flux ratio in LW bands with noise . . . . .	30
2.9	Source counts in LW bands with noise . . . . .	32
2.10	Detection correctness with noise . . . . .	35
3.1	Structure of software . . . . .	43
3.2	The total response function . . . . .	46
3.3	Virtual input data . . . . .	47
3.4	PSF convolved image . . . . .	48
3.5	$\lambda$ - coadded image . . . . .	51
3.6	The brightness distribution along one-dimensional cut . . . . .	53
4.1	Profiles of the point source in simulated scans . . . . .	60
4.2	Reconstructed image including transients, crosstalk and glitches . . . . .	64
4.3	Simulated $1^\circ \times 1^\circ$ images . . . . .	65
4.4	Ratio of the output flux to the input flux . . . . .	66

5.1	Structure of the simulation software . . . . .	74
5.2	Spectral energy distribution and luminosity function . . . . .	76
5.3	Flux ratio between the input and the output fluxes . . . . .	78
5.4	Integrated source count results . . . . .	79
5.5	Predicted redshift distribution. . . . .	82
6.1	Schematic outline of the reference aperture configurations . . . . .	88
6.2	Measured power spectrum of dust emission . . . . .	91
6.3	Simulated dust emission map and the profile of map . . . . .	93
6.4	Patch of SFD98 dust map, regenerated patch and the estimated power spectrum . . . . .	94
6.5	Comparison between the two dust models for one small patch . . . . .	97
6.6	PSF-convolved patch of the dust map . . . . .	101
6.7	The fraction of the sky brightness for all sky . . . . .	104
6.8	Estimated sky confusion noise for the ISO mission . . . . .	107
6.9	Estimated sky confusion noise for the ASTRO-F mission . . . . .	108
6.10	Estimated sky confusion noise for the Spitzer mission . . . . .	109
6.11	Estimated sky confusion noise for the Herschel and SPICA mission . . .	110
6.12	The relation between $P_0$ and $B_0^3$ . . . . .	111
6.13	Dependency of the sky confusion noise on separation . . . . .	113
6.14	Source distribution in the SW band and LW band . . . . .	117
6.15	Simulated images including point sources in the LW band for ISO and ASTRO-F . . . . .	118
6.16	Simulated images including point sources in the LW band for Spitzer, and Herschel and SPICA . . . . .	119
6.17	Estimated detection limit by photometry . . . . .	120
6.18	The comparison between the photometric results and the estimated sky confusion noise . . . . .	123
6.19	Detection limits due to Galactic cirrus as a function of Galactic latitude	124
6.20	Detection limits due to Galactic cirrus at mean and low sky brightness	126

7.1	Model input spectral energy distributions . . . . .	138
7.2	$S_c/\sigma$ ratio as a function of $S_c$ for Spitzer and Herschel & SPICA missions	146
7.3	Expected redshift distribution for ASTRO-F mission . . . . .	153
7.4	Expected redshift distribution for Spitzer mission . . . . .	154
7.5	Expected redshift distribution for Herschel & SPICA mission . . . . .	155
7.6	Expected CFIRB fluctuation for each mission and burst evolution model	158
A.1	PSF of the ASTRO-F/FIS at 200 $\mu\text{m}$ . . . . .	170
A.2	Filter transmission and detector's response function (SW band) . . . . .	173
A.3	Filter transmission and detector's response function (LW band) . . . . .	174
A.4	Total response function for Spitzer mission . . . . .	175
A.5	Cloud-In-Cell scheme . . . . .	176
A.6	Normalised Compiled PSFs . . . . .	179
A.7	Variation of FWHM in SW bands for ASTRO-F/FIS mission . . . . .	180
A.8	Variation of FWHM in LW bands for ASTRO-F/FIS mission . . . . .	181
A.9	Variation of FWHM for Spitzer . . . . .	182
B.1	Layout of the detector array . . . . .	184
B.2	Passage of the detector . . . . .	185
B.3	Schematic figure for subsamples . . . . .	186



# List of Tables

2.1	Specifications of the FIS . . . . .	12
2.2	Simple estimates of $5\sigma$ detection . . . . .	21
2.3	$5\sigma$ detection limits of FIS bands . . . . .	23
2.4	$5\sigma$ detection limits due to theoretical confusion noise . . . . .	26
2.5	Detection limits for distributed point sources without noise . . . . .	34
2.6	Detection limits for distributed point sources with noise . . . . .	36
4.1	Time-constants and contributions of transient component . . . . .	61
4.2	Parameters for four types of glitches . . . . .	63
5.1	$5\sigma$ detection limits . . . . .	80
6.1	Instrumental parameters for various space missions. . . . .	99
6.2	Normalization constant $\zeta$ of HB90 formula for each space mission. The instrumental parameters for each mission are given in Table 6.1. The mean brightness here is fixed to be $1 \text{ MJy sr}^{-1}$ . . . . .	100
6.3	Properties of the selected regions. The Galactic longitude of all patches is $0^\circ$ . $B_0$ is a mean sky brightness, $\alpha$ is the power index of the power spectrum, and $P_0$ is the power estimated at $0.01 \text{ arcmin}^{-1}$ and $100 \mu\text{m}$ . . . . .	102
6.4	Ratio $\psi$ of the sky confusion noise for the different power indices. . . . .	115
7.1	Parameters for the No Evolution Model . . . . .	142
7.2	Parameters for the Luminosity Evolution Model . . . . .	143
7.3	Parameters for the Burst Evolution Model . . . . .	144

7.4	Source confusion estimated by the definition of 40 beams per source . . .	145
7.5	Source confusion estimated by the definition of fluctuation . . . . .	147
7.6	Source confusion estimated by the definition of the composition of fluctuation and photometry . . . . .	148
7.7	Estimated confusion limits due to Galactic cirrus for each mission . . .	149
7.8	Ratio of source confusion to sky confusion for no evolution model . . .	149
7.9	Ratio of source confusion to sky confusion for luminosity evolution model	150
7.10	Ratio of source confusion to sky confusion for burst evolution model . .	150
7.11	Final confusion limit . . . . .	151
7.12	Expected CFIRB intensity . . . . .	156
7.13	Expected CFIRB fluctuation . . . . .	157
7.14	Comparison of CFIRB fluctuation . . . . .	157

# Chapter 1

## Overview of the Observing Simulations

### 1.1 Introduction

Since the observations in the far-infrared are difficult on the ground due to the Earth's atmosphere, the far-infrared observation projects are mostly performed in the space. Generally speaking, the hardware characteristics of each component in a space mission can be measured in the laboratory. However, it is very difficult to make end-to-end tests of the mission in the laboratory. Hence, on the basis of the data measured for each component, numerical simulations are frequently used in order to understand the instrument performances as a whole. Moreover, the complicated interplay between the celestial sources and hardware specifications can be studied only by the simulation prior to the launch. Many valuable data in the far-IR wavelength range will be available within or around this decade by a multitude of IR space projects such as Spitzer (formerly known as SIRTF, the Space Infrared Telescope Facility) (Gallagher et al. 2003), ASTRO-F (Murakami 1998; Shibai 2000; Nakagawa 2001; Pearson et al. 2004), Herschel Space Observatory (HSO) (Pilbratt 2003; Poglitsch et al. 2003) and the Space Infrared Telescope for Cosmology and Astrophysics (SPICA) (Nakagawa 2004). Therefore, we need to expect the performance for the present / incoming space missions

in order to design the proper scientific projects.

Most important question regarding the performance of space projects is the estimation of the effective detection limit for faint sources. Depending on the size of the sources compared to the beam size of telescope, the source can be either extended or point-like, and detection limits will depend on the nature of the sources. In the present work, we will only consider point sources. Among several factors contributing to the detection limits, two major noise, the instrumental noise and the confusion noise, make the main limitation to the source detection. The instrumental noise represents the sensitivity of the detectors and the entire telescope system which can be determined by the readout process of the system and the photon noise with Poisson nature. The ‘confusion noise’ makes the fluctuations of the background sky brightness; these fluctuations are caused by intrinsically discrete extragalactic sources and the structure of the Galactic cirrus. The confusion noise sets the fundamental limit to the astronomical observations. Since the sources below the fluctuation by confusion noise can not be detected individually, we can not reduce the confusion noise even though we extend the exposure time indefinitely. Therefore, confusion is unavoidable even with arbitrarily high resolution because of the finite sizes of sources on the sky.

## 1.2 Optimal Algorithm for Observing Simulations

Based upon the background emission, infrared source crowding, and detector performance, there have been many simple estimates for the expected performance of the space missions. The purpose of the estimates is to evaluate the effects of variations in basic mission system parameters for typical operation over the given wavelength range. Since the detectors used in the infrared missions have the non-ideal characteristics, it is important to check the pipeline of the data reduction before the prior to launch. Moreover, in order to check the complicated interaction between various parameters and the space environments, the analysis from realistically simulated data is essential to find the optimal observation strategy and compare with the results obtained from real data. However, since it requires the considerable computing power, we should

think over how to reduce the computation time and obtain the appropriate accuracy of the simulation with limited memory and CPU powers. In section 2 and appendix B, we describe the structure of our observing simulations and propose the algorithms to optimise inevitable, but time-consuming, convolution processes.

### 1.3 Observing Simulation for Survey Mode

In order to obtain the image data through the space infrared observation, the space telescope are designed to have the survey mode or the pointing mode (or both of them). In the survey mode, a spacecraft performs continuous scan of the sky. The signal from the detectors is the time-series data over the sampling sequence. Since the sensitivity of the detectors is changed according to the space environments, e.g., cosmic ray hitting, continuous change of the background, complicated correction routines in the data reduction pipeline are required. In addition, we have to perform the image reconstruction with the corrected time-series signal. The survey mode is proper to carry out the observation for the vast of sky, while it is difficult to reduce the data. On the other hand, the pointing mode observation is to observe the programmed sky position according the observation strategy.

We present the detection limits for the survey mission, ASTRO-F/FIS by using the simple power-law model for the source distribution in section 2. The expected observing data for three different sampling rate in the survey mode observation are described in section 3. We present the effects of the detector characteristics in section 4 and in section 5, the expected source count results from the FIS survey by introducing a point source catalogue generated from the models of Pearson & Rowan-Robinson (1996), Pearson (2001), and Rowan-Robinson (2001).

### 1.4 Sky Confusion Due to Cirrus

Galactic emission in the far-infrared sky affects the detection of the faint infrared sources. The amount of emission acts as the photon noise for each time-series signal

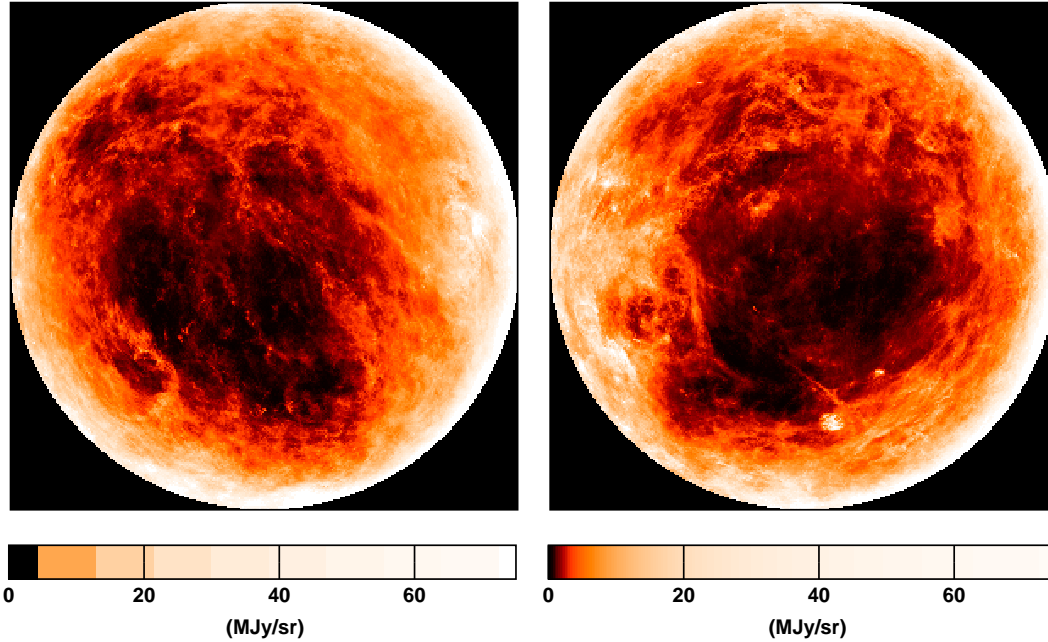


FIG. 1.1: All-sky dust map at  $100 \mu\text{m}$  (Schlegel et al. 1998). Left panel is for north hemisphere and right panel is for south hemisphere in Galactic coordinate.

of a detector pixel. In addition, sky confusion noise by the cirrus emission causes an uncertainty in the determination of the source flux, due to the variation of the sky brightness, which is originated from the dust emission of interstellar clouds, ‘Galactic cirrus’ (see figure 1.1). Therefore, we have to consider this Galactic emission depending on the sky position for the realistic observing simulation.

The sky confusion depends upon both the variation of the surface brightness in the background structure and the resolution of the telescope. Consequently, the noise becomes less significant for larger aperture sizes such that the next generation of space telescopes (e.g., Herschel and SPICA) should not be severely affected by sky confusion over most of the sky. In many cases, the power spectrum of the dust emission which represents the structure of the cirrus, can be expressed as a simple power-law. Using the IRAS data at  $100 \mu\text{m}$ , Gautier et al. (1992) computed the power spectrum of the spatial fluctuations of cirrus emission and estimated the sky confusion noise with the

empirical relationship,  $P_0 \propto \langle B_0 \rangle^3$  and  $\alpha = -3$ , where  $P_0$  is the power at the reference scale length,  $B_0$  is the mean brightness of cirrus emission, and  $\alpha$  is the power index of the power spectrum. Helou & Beichman (1990) extended the work of 100  $\mu\text{m}$  by Gautier et al. (1992) in order to estimate the sky confusion at all wavelengths. They found an approximation for the cirrus confusion noise as follows:

$$\frac{N_{\text{HB90}}}{1 \text{ mJy}} = 0.3 \cdot \left( \frac{\lambda}{100 \mu\text{m}} \right)^{2.5} \left( \frac{D_t}{1 \text{ m}} \right)^{-2.5} \left( \frac{\langle B_\lambda \rangle}{1 \text{ MJy sr}^{-1}} \right)^{1.5}, \quad (1.1)$$

where  $\lambda$  the wavelength of the measurement,  $D_t$  the diameter of the telescope, and  $\langle B_\lambda \rangle$  is the mean brightness at the observation wavelength.

Since we will observe the sky with high resolution, we should check the detection capability of the point sources in the Galactic emission map of the whole sky with this resolution. Although Schlegel, Finkbeiner, and Davis (1998) presented the full-sky 100  $\mu\text{m}$  dust map, the spatial resolution of this map is  $\sim 6.1$  arcmin which is not sufficient to apply to our simulation in order to check the effect of small-scale fluctuation of dust emission in the source detection. In our work, we estimate the sky confusion noise by cirrus for various space missions with higher resolution compared with IRAS mission in section 6.

## 1.5 Source Confusion

The source confusion resulted from the overlapping of many faint extragalactic sources and mainly depends on the source distribution and the beam pattern of the telescope. First, we define a differential number count per square degree with flux  $S \sim S + dS$ ,  $n(S)$ ,

$$n(S) = \frac{dN}{dS}, \quad (1.2)$$

where  $N = N(> S)$  is the integrated number count. Let  $h(\theta, \phi)$  be the beam pattern (normalized to unity at the beam center), and  $x = Sh(\theta, \phi)$ , the response of the telescope to a source of flux density  $S$  located at an angular position  $(\theta, \phi)$  from the

beam axis. The mean number of source responses of intensity  $x$  in a beam is

$$R(x)dx = \int_{\Omega_{\text{beam}}} n \left( \frac{x}{h(\theta, \phi)} \right) \frac{dx}{h(\theta, \phi)} d\Omega . \quad (1.3)$$

The beam pattern  $h(\theta, \phi)$  is usually approximated as an ideal circular aperture Airy pattern corresponding to the aperture size of telescopes. We assume that the number count is described by a power-law:

$$n(S) = \alpha S^{-\gamma} . \quad (1.4)$$

Then we have

$$n \left( \frac{x}{h(\theta, \phi)} \right) = \alpha \left( \frac{x}{h(\theta, \phi)} \right)^{-\gamma} = \alpha h(\theta, \phi)^{\gamma} x^{-\gamma} . \quad (1.5)$$

The mean number of  $x$ ,  $R(x)$  is

$$R(x) = \int_{\Omega_{\text{beam}}} \alpha h(\theta, \phi)^{\gamma} x^{-\gamma} \frac{d\Omega}{h(\theta, \phi)} = \alpha \Omega_{\text{eff}} x^{-\gamma} , \quad (1.6)$$

where  $\Omega_{\text{eff}}$  is

$$\Omega_{\text{eff}} \equiv \int_{\Omega_{\text{beam}}} h(\theta, \phi)^{\gamma-1} d\Omega . \quad (1.7)$$

We obtain the confusion limit flux to a cutoff deflection  $x_c$ :

$$\sigma(x_c)^2 = \int_0^{x_c} x^2 R(x) dx . \quad (1.8)$$

This formula is used very frequently, probably because it is expressed in a simple analytic function. However, we should set a certain cutoff in the integration in the real calculation. In addition, though the clustering of sources could also affect the confusion noise, we can ignore such a possibility for simplicity.

The source confusion depends on the the source distribution by the cosmological models obtained from the source counts results. We check the source confusion with both the theoretical approach and the photometric approach, and the expected contribution from Cosmic Far-Infrared Background (CFIRB) by the observing simulation in section 7.

### 1.5.1 Source Counts and Evolution Model

To produce the input source distributions we calculate the total number of sources per steradian at observation wavelength,  $\lambda_o$ , down to some flux limit  $S_{\lambda_o}$ ;

$$N(S_{\lambda_o}) = \int_0^\infty \int_0^{z(L,S)} \phi(L/f(z)) \frac{dV(z)}{dz} e(z) dl g L dz, \quad (1.9)$$

where  $f(z)$  &  $g(z)$  are evolutionary factors. The integration is made over the luminosity function (number density of objects as a function of luminosity),  $\phi(L)$  and the cosmological volume  $V$ , enclosed inside a limiting redshift  $z(L, S)$  defined as the redshift at which a source of luminosity,  $L$ , falls below the sensitivity,  $S(\lambda_o)$  of a given observation, where  $S(\lambda_o)$  is given by;

$$S(\lambda_o) = \frac{d\lambda_e}{d\lambda_o} \frac{L_{\lambda_e}}{4\pi D_L^2} = \frac{L_{\lambda_o}}{4\pi D_L^2} \frac{\lambda_e L_{\lambda_e}}{\lambda_o L_{\lambda_o}} f(z), \quad (1.10)$$

where the suffix  $o$  &  $e$  correspond to the observation frame and emission rest frame respectively and  $D_L$  is the luminosity distance in a flat, vacuum energy dominated universe ( $\Omega_m = 0.3, \Omega_\Lambda = 0.7$ ) given by;

$$D_L(z) = \left( \frac{c}{H_o} \right) \int_0^z \frac{(1+z) dz}{\sqrt{(1+z)^2(1+\Omega_m z) - z(2+z)\Omega_\Lambda}}, \quad (1.11)$$

corresponding to differential volume per steradian required in equation 7.12 of;

$$\frac{dV(z)}{dz} = \left( \frac{c}{H_o} \right) \frac{(1+z)^{-2} D_L^2}{\sqrt{(1+z)^2(1+\Omega_m z) - z(2+z)\Omega_\Lambda}}, \quad (1.12)$$

Luminosity functions are determined from the IRAS PSCz catalogue at  $60\mu\text{m}$  (Saunders et al. 2000). Saunders et al. (1990) subdivided the luminosity function of IRAS galaxies into *warm* and *cool* components following colour criteria akin to those of Rowan-Robinson & Crawford (1989). Similarly, the *hot* AGN population is well represented by the  $12\mu\text{m}$  sample of Rush, Malkan & Spinoglio (1993) using the luminosity function of Lawrence et al. (1986). From this population and luminosity function, we can make various scenarios of the evolution.

We have to test various source count models including the evolution models. From the analysis of source count results, we can check whether the theoretical estimates

are realistic and discuss the competing necessities of reliability and completeness. In addition, these source count results can be compared with the source counts obtained from real observations in the future.

### **1.5.2 Cosmic Far-Infrared Background**

One of the outstanding challenges in modern cosmology is to explain the formation of structure in the universe. The cosmic infrared background records much of the radiant energy released by processes of structure formation that have occurred since the decoupling of matter and radiation following the Big Bang. In the past study from infrared missions, the measurements of this background are carried out. At the same time, there has been a rapid progress in resolving a significant fraction of this background with the deep galaxy counts at infrared wavelengths.

The suggestions that the CFIRB mostly originates from the discrete unresolved extragalactic sources are proposed (Schlegel, Finkbeiner & Davis 1998; Guiderdoni et al. 1997; Juvela, Mattila & Lemke 2000). The number of unresolved sources produces the fluctuations in the measured background brightness. Hence, the measurement of fluctuations in the extragalactic background reveals information about the number and distribution of contributing sources.

# REFERENCES

- Gautier III, T. N., Boulanger, F., Péroult, M., & Puget, J. L., 1992, *AJ*, 103, 4
- Guiderdoni B. et al., 1997, *Nature*, 390, 257
- Helou G., Beichman C. A., 1990, *Proc. of the 29th Liege International Astrophysical Coll.*, ESA Publ., 117 (HB90)
- Juvela M., K. Mattila, D. Lemke, 2000, *A&A*, 360, 813
- Lawrence A., Walker D., Rowan-Robinson M., Leech K.J., Penston M.V., 1986, *MNRAS*, 219, 687
- Nakagawa T., 2001, in the *Proc of The Promise of the Herschel Space Observatory*, ed. G. L. Pilbratt, J. Cernicharo, A. M. Heras, T. Prusti, & R. Harris, *ESA-SP*, 460, pp. 67-74
- Nakagawa T., 2004, *Adv. Space Res.*, in press
- Pearson, C. P., and M. Rowan-Robinson, 1996, *MNRAS*, 283, 174
- Pearson, C. P., 2001, *MNRAS*, 325, 1511
- Rowan-Robinson M., Crawford P., 1989, *MNRAS*, 238, 523
- Rowan-Robinson M., 2001, *ApJ*, 549, 745
- Rush B., Malkan M., Spinoglio L., 1993, *ApJSS*, 89, 1

Saunders W., Rowan-Robinson M., Lawrence A., Efstathiou G., Kaiser N., Ellis, R.S.,  
1990, MNRAS, 242, 318

Saunders W., et al., 2000, MNRAS, 317, 55

Schlegel, D. J., Finkbeiner, D. P., & Davis, M., 1998, ApJ, 500, 525

## Chapter 2

# ASTRO-F/FIS Observing Simulation: Detection Limits for Point Sources<sup>†</sup>

### Abstract

We describe the observing simulation software FISVI (FIS Virtual Instrument), which was developed for the Far-Infrared Surveyor (FIS) that will be on the Japanese infrared astronomy mission ASTRO-F. The FISVI has two purposes: one is to check the specifications and performances of the ASTRO-F/FIS as a whole; the other is to prepare input data sets for the data analysis softwares prior to launch. In the FISVI, special care was taken by introducing the “Compiled PSF (Point Spread Function)” to optimise inevitable, but time-consuming, convolution processes. With the Compiled PSF, we reduce the computation time by an order of magnitude. The photon and readout noises are included in the simulations. We estimate the detection limits for point sources from the simulation of virtual patches of the sky mostly consisting of distant galaxies. We studied the importance of source confusion for simple power-law models for  $N(> S)$ , the number of sources brighter than  $S$ . We found that source

---

<sup>†</sup>W.-S. Jeong, S. Pak, H. M. Lee, T. Nakagawa, J. Sohn, I. Ahn, I. Yamamura, M. Watanabe, M. Kawada, & H. Shibai, PASJ, 55, 717

TABLE 2.1: Specifications of the FIS.

Band	Wavelength range ( $\mu\text{m}$ )	Array size (pixel)	Pixel size (arcsec)	Pitch size (arcsec)	Sampling rate (Hz)
WIDE-L	110 – 200	$15 \times 3$	44.2	49.1	15.2
N170	150 – 200	$15 \times 2$	44.2	49.1	15.2
WIDE-S	50 – 110	$20 \times 3$	26.8	29.5	22.8
N60	50 – 75	$20 \times 2$	26.8	29.5	22.8

confusion plays a dominant role in the detection limits only for models with rapid luminosity evolution for the galaxy counts, the evolution of which is suggested by recent observations.

## 2.1 Introduction

The FIS (Far-Infrared Surveyor) is one of the focal plane instruments of the ASTRO-F mission (previously known as IRIS) (Murakami 1998; Shibai 2000; Nakagawa 2001). The ASTRO-F satellite will be launched into a sun-synchronous orbit at an altitude of 750 km, which corresponds to an orbital period of 100 min. The telescope, which is cooled down to 5.1–5.8 K, has a 67 cm primary mirror. The major task of this mission is to carry out an all-sky survey across the 50–200  $\mu\text{m}$  range. The basic parameters of the ASTRO-F/FIS are summarized in table 2.1 (see also Kawada 2000).

ASTRO-F/FIS will bring data with much higher sensitivity and angular resolution than those of IRAS (see Kawada 2000 for detailed comparison). Such data sets will be of great value for many areas of astrophysics, including cosmology, galaxy evolution, interstellar medium, and asteroids.

Generally speaking, the hardware characteristics of each component in a space mission can be measured in the laboratory. However, it is very difficult to make end-to-end tests of a mission in the laboratory. Hence, based on data measured for each

component, numerical simulations are frequently used to understand the instrument performances as a whole (e.g., Garcia et al.(1998); Boggs, Jean(2001)). Moreover, the complicated interplay between the celestial sources and hardware specifications can be studied only by a simulation prior to the launch.

We have constructed a software simulator called the FISVI representing Virtual Instrument of the FIS, that can simulate the data stream of ASTRO-F/FIS (Jeong et al. 2000). This work is an extension of initial work by Matsuura (2001). The purposes of the FISVI are : (1) to confirm the performance of the hardware as a whole and (2) to generate simulated FIS survey data sets as inputs for data-reduction software prior to launch.

One of the key questions regarding the performance of ASTRO-F is the effective detection limit for faint sources. Depending on the size of the sources compared to the beam size of ASTRO-F, the source can be either extended or point-like, and the detection limits depend on the nature of the sources. In the present work, we only consider point sources.

There are several factors contributing to the detection limits. The sensitivity of the detectors and the entire telescope system allows only sources brighter than a certain threshold to be reliably measured. Since the photons follow Poisson statistics, the background photons due to the sky brightness as well as the telescope emission should fluctuate, and a meaningful detection of a source can be made only if the signal from the source exceeds the level of the fluctuations. The sky confusion noise by the cirrus emission causes an uncertainty in the determination of the source flux, due to the variation of the sky brightness (Herbstmeier et al. 1998; Kiss et al. 2001). The readout process also adds more fluctuations. Moreover, the measurement of the brightness of a source can be further influenced by neighboring sources if more than one source lies within a single beam of the telescope. The final detection limit should thus depend on the performance of the entire system, the brightness of sky and telescope emission, readout process, and the distribution of sources as a function of the flux.

There have been a number of estimates of detection limits based on the available laboratory data (e.g., Kawada 1998, 2000) using simple calculations. Clearly, a more

realistic estimation can be made by using numerical simulations. In the present work, we carried out simulations of the ASTRO-F/FIS observations under several different circumstances in order to obtain still more reliable detection limits which can be used to design scientific projects.

The present paper is organised as follows. In section 2.2, we briefly describe the design and the structure of the FISVI. In section 2.3, we explain how we obtain the observed images based on the simulated data set. In section 2.4, we make estimate on the detection limits of the ASTRO-F/FIS under various circumstances. First, we estimate the detection limits of a single isolated point source while considering only photon and readout noises. Also, we estimate the confusion noise (Condon 1974; Franceschini et al. 1989) for distributed sources using a simple formula. By carrying out aperture photometry to the simulated images, we finally obtain combined detection limits that include photon, readout, and confusion noises. The final section summarises our conclusions.

## 2.2 Structure of FISVI Software

The algorithm of the FISVI software is shown in figure 2.1. The input data file provides the coordinates and fluxes of the sources in the sky. Although the sources would appear either point-like or extended, we concentrate on point sources in this paper. The software first makes images on the focal plane by convolving the point sources and the Point Spread Function (PSF) of the telescope and the instrument. The software generates time-series data for each pixel by simulating the scanning procedure of the ASTRO-F/FIS survey mode observations.

Since the PSF, the filter transmission, and the detector response depend on the wavelength of incoming photons, we need to do repeated calculations (procedures boxed in the left panel of figure 2.1) for different wavelengths within the individual FIS bands, as shown in the left panel of figure 2.1. To elude this and speed up the procedure, we introduce the Compiled PSF in this work, with which we can perform this scanning procedure at once, as shown in the simplified flow chart in the right panel of figure 2.1.

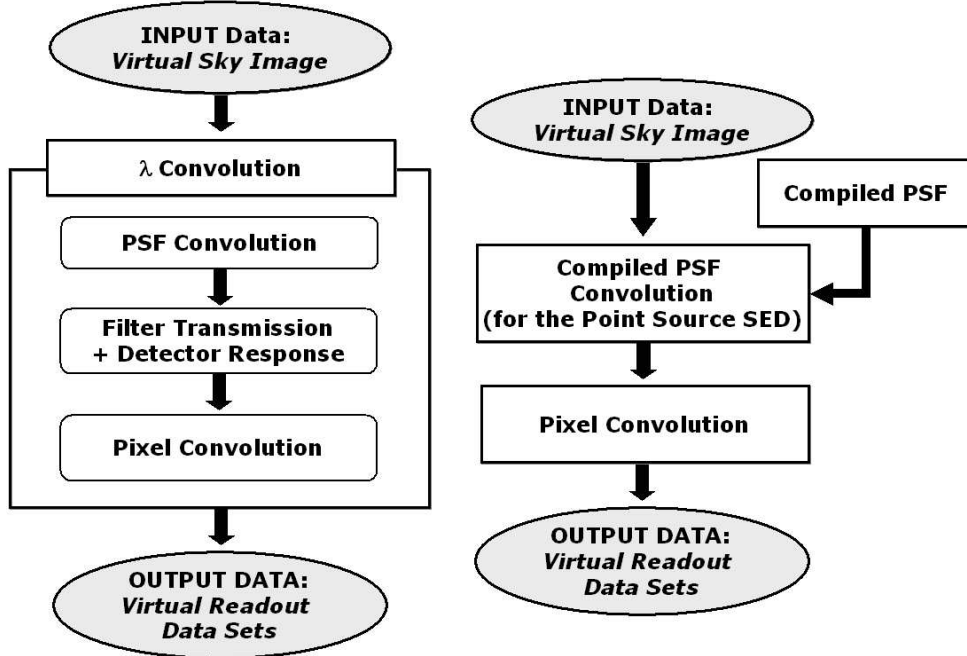


FIG. 2.1: Flow charts of FISVI. The left chart shows a straightforward procedure based on the realistic photon path, where repeated calculations would be necessary over the wavelength grids (“ $\lambda$  Convolution”). The right chart, on the other hand, shows the accelerated algorithm using the Compiled PSF for the FISVI.

A more detailed discussion on the gains in the computational time and possible errors due to the use of the Compiled PSF are presented in appendix A.

The readout values for each pixel are represented by a series of integrated charges taken over the area covered by the pixel, sampled at regular time intervals. The integrated charges are set to zero at every reset interval. The time series of the integrated charges are differentiated to obtain the charges accumulated during the sampling interval (see appendix B for detailed process). We also generate the photon and readout noise and include them to be part of readout values. A more detailed discussion on the implementation of noise is presented in subsection 2.4.1. The time-series data are converted into the brightness distribution on the sky, and are used to reconstruct the images, as described in section 2.3.

## 2.3 Image Reconstruction

The FISVI generates time-series data for each pixel. In figure 2.2, we show a series of readout values of a pixel that scans across a point source. No reset was applied during the readout sequence shown in this figure because the reset time interval is usually much longer than the passage of a Compiled PSF over a point source. The differentiation (subtraction of adjacent sampling points) of this curve gives the signal obtained during a sampling interval by one detector pixel, which is shown in the lower panel of figure 2.2.

The pixel readouts can be used to reconstruct the images. In the current implementation of the FISVI, following method was used to generate the image. In order to reconstruct the image, we assume that pixel value represents the uniform intensity over the pixel surface. This means that a particular point can be covered by more than one readout. We always take the average values of multiple readouts in order to construct images (see figure 2.3). Due to the convolution of the image with the pixel size, the output image will be blurred slightly.

Since we have to obtain “average” intensity in overlapped areas, we keep in counting the number of overlaps. This is done by employing additional array with very small mesh sizes. The accuracy reconstructing the flux and the position of source depends on the mesh size. The error of grid value becomes smaller in smaller mesh size. We use the mesh size of  $4'' \times 4''$  to achieve  $< 1\%$  error levels.

## 2.4 Estimations of FIS Performance

An estimation of the detection limits for the planned mission is very important. For ASTRO-F, the detection limits were estimated by using analytic methods (Kawada 1998, 2000). In the present work, we made a numerical estimate for a single point source using the latest information for the detectors and filters, and compared them with the photometric results on the FISVI generated images that contain a large number of point sources.

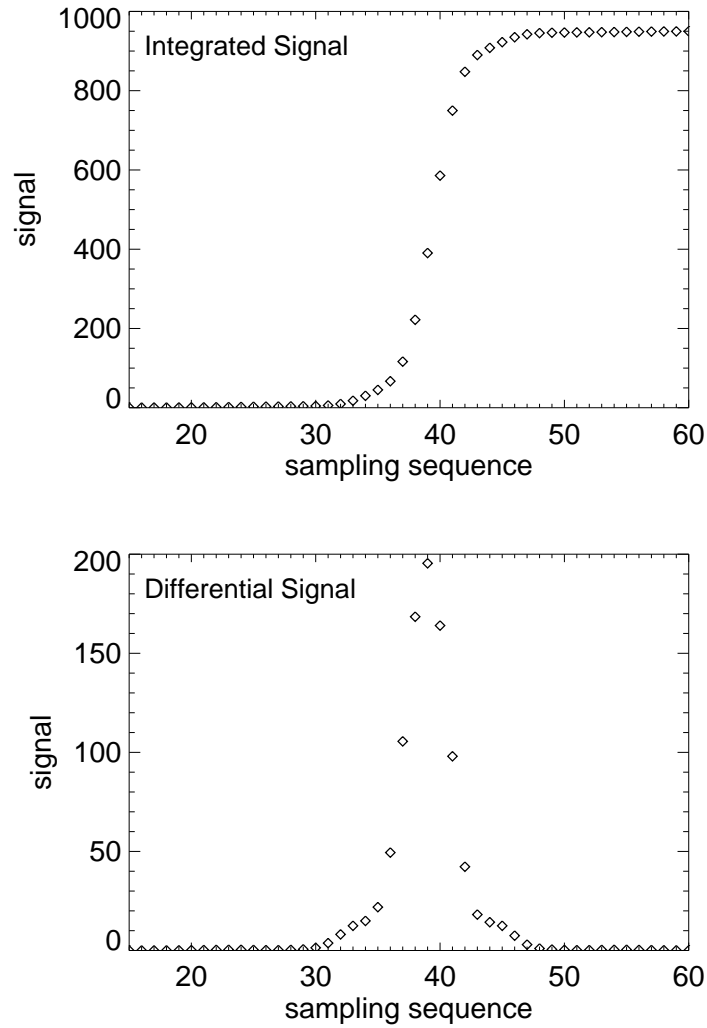


FIG. 2.2: Example of a series of readout values, which corresponds to the integrated charges since the last reset [see equation (A.5)], of a WIDE-L pixel that scans through a point source (upper panel). The differentiation of the integrated charges as shown in the lower panel corresponds to the signal obtained during a sampling interval by one detector pixel passing the image of a point source. The sampling interval was  $14''.2$ , corresponding to the 15.2 Hz readout (see table 2.1).

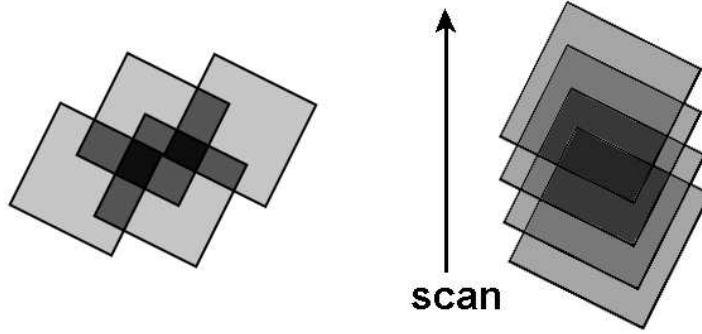


FIG. 2.3: Schematic figure for image reconstruction by pixel averages. At any given point, we take the average of the pixel readouts that were covered by those pixels. In the figure, the darker area means the area that was covered more.

### 2.4.1 Detection Limits for a Single Point Source

The detection limits for a single point source depend on the level of noise. There are several sources of noise: photon noise due to the sky background and thermal emission from the telescope, and readout noise. The sky background varies significantly from place to place in the sky. On average, the infrared sky becomes brighter in the Galactic plane, and diminishes toward the Galactic poles. Within the Galactic plane, the emission from the Galactic center direction appears to be brighter than towards the anti-center direction. Because of thermal emission by interplanetary dust particles, the ecliptic plane is also brighter than the ecliptic pole region. In figure 2.4, we show the assumed surface brightness distribution of background emissions from the interstellar dust, the interplanetary dust and the telescope, for the purpose of generating photon noises. These background emissions from the sky are assumed to correspond to the dark part of the sky and the sky confusion noise due to the structure of the cirrus emission is not considered. The telescope temperature is assumed to be 6 K, as a conservative number. In figure 2.4, we also plotted the thermal emission from the 6.5 K telescope as a comparison. Evidently, the contribution from the telescope is smaller than that from the interplanetary or interstellar dust as long as the telescope temperature is

lower than 6.5 K for the entire FIS bands. The sky brightness throughout the spectral region of the FIS varies from 5 to 7 MJy sr<sup>-1</sup>. Obviously, we would need to apply a position-dependent background brightness for more realistic sky simulations, which affects the photon noise. The incoming photon stream on pixels due to background emission is assumed to follow Poisson statistics.

The readout circuit also generates uncertainties of the output values, called readout noise. This type of noise is independent of the sampling rate and the integration time, and we assumed the total noise in the effective bandwidth at the first stage of the field effect transistor (FET) gate to be 3  $\mu$ V. In the simulation, we assumed that the readout noise follows Gaussian statistics.

### Simple estimation

The sky brightness throughout the spectral region of the FIS varies from 5 to 7 MJy sr<sup>-1</sup>. The integrated photons fluctuate following the Poisson statistics while the readout process adds readout noise, which is assumed to follow Gaussian statistics. The r.m.s. fluctuation of voltage across the integrating charge due to readout noise can be converted to the fluctuation in the number of charges by

$$D_{\text{rms}} = \frac{C V_{\text{rms}}}{e}, \quad (2.1)$$

where  $C$  is the capacitance of the charge integrators [7 pF for SW (short wavelength) and 10 pF for LW (long wavelength) bands, respectively], and  $e$  is the elementary charge. The total noise is a combination of photon and readout noise.

If we assume that a single pixel detector receives the entire photon flux of the point source, we can obtain the accumulated charge during ‘the effective integration time’ that elapses until the detector pixel passes through one point. For a photoconductor, the noise by this photon flux arises from the sequence of generations and recombinations of photoelectrons. We calculated this generation-recombination noise (G-R noise),  $I_{\text{G-R}}$  (Rieke 1994) using

$$\langle I_{\text{G-R}}^2 \rangle = 4e^2 \varphi \eta G^2 df, \quad (2.2)$$

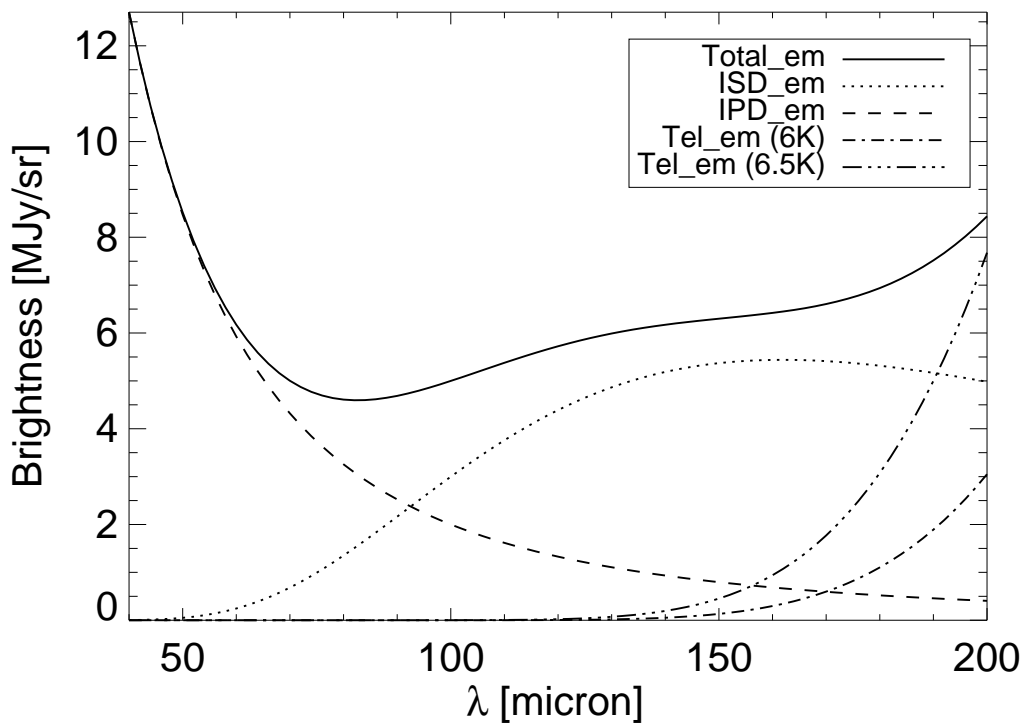


FIG. 2.4: Assumed background emissions. We consider three components for the background emission, i.e., interstellar dust (dotted), interplanetary dust (dashed) and telescope emission assuming 6 K (dot-dashed line) or 6.5 K black body (long dot-dashed line). In our simulations, the telescope temperature is always assumed to be 6 K.

TABLE 2.2: Simple estimates of  $5\sigma$  detection of single pixels and the ratios of photon-to-readout noises.

	$5\sigma$ Det. Limit (mJy)*	$\sigma_r/\sigma_{\text{ph}}^\dagger$
WIDE-L	39	1.3
N170	76	1.8
WIDE-S	20	1.6
N60	52	2.5

\* Average flux density in the bandwidth.

† Readout-to-photon noise ratio.

where  $\varphi$  is the photon flux,  $\eta$  is the quantum efficiency,  $G$  is the photoconductive gain, and  $df$  is the effective bandwidth. We assumed that the source has the SED of a 40 K blackbody. The  $5\sigma$  detection limits computed in this way for all FIS bands are shown in table 2.2. Also shown in this table is the relative importance of the photon and readout noise. In all cases, the readout noise is more important than the photon noise, with narrow bands (N170 and N60) being more dominated by readout noise.

### Estimation using scanning simulations of a single pixel

We also estimate the detection limits from the detector scanning routines in the FISVI for a single pixel. The behavior of the readout values as a function of the sampling sequence is shown in figure 2.2. The contribution due to background can be obtained by subtracting the contribution from the source alone. The expected amount of the fluctuation is proportional to  $G\sqrt{\varphi\eta}$  for a given span of the scanning period of  $t_1$  to  $t_2$  [see equation (2.2)]. The total amount of fluctuation of the readout value due to noises during the same scanning span,  $\sigma_{\text{tot}}$ , is

$$\sigma_{\text{tot}} = \sqrt{\sigma_{\text{ph}}^2 + \sigma_r^2}, \quad (2.3)$$

where  $\sigma_{\text{ph}}$  and  $\sigma_{\text{r}}$  are the fluctuation due to the photon and readout noise, respectively. Here, we assume that the readout noise is always a constant while the amount of charge fluctuation due to the photon noise increases as  $G\sqrt{\varphi\eta}$ , as dictated by the Poisson nature. For a given brightness of a source, we can obtain the  $S/N$  ratio if we specify  $t_1$  and  $t_2$ . Since the signal (photocurrent) and the photon noise are proportional to  $G$ ,  $S/N$  depends on  $\sqrt{\eta}$  on the condition that the photon noise is the dominant case. From equation (A.7) and the assumption  $G = 0.9$ , we can obtain the quantum efficiency,  $\eta$ , as 0.17 for SW and 0.27 for LW detectors, respectively. The determination of  $t_2$  and  $t_1$  was done to maximize the  $S/N$ . We find that this can be done when we start the scanning at a distance of  $2W_{\text{H}}$  and continue until the same distance in the opposite side, where  $W_{\text{H}}$  is the full width at half maximum of the beam patterns (see subsection 2.4.2 for details). The  $5\sigma$  detection limits determined in this way for all FIS bands are listed in table 5.1. These estimates also assume a blackbody source with a temperature of 40 K. We find that the estimates using the simple method described in subsection 2.4.1 and here agree very well each other. The largest discrepancy occurs for the N60 band, where the estimated detection limit using scanning simulation is lower by around 10%. The instrumental noise in ISO observation is estimated to be 15–45 mJy (Herbstmeier et al. 1998; Dole et al.(2001)). Assuming our background brightness of  $\sim 5$  MJy  $\text{sr}^{-1}$ , this noise level is similar with our estimation in the wide bands. We analyse the photometric accuracy of point sources in more realistic simulations with distributed sources below.

### 2.4.2 Simulations with Distributed Point Sources and Realistic Detector Configurations

The FISVI takes into account the full configuration of FIS detector arrays. We now discuss the simulations over a finite patch of the sky with randomly distributed sources. By carrying out the photometry of simulated images, we should be able to determine more realistic detection limits.

Most faint sources to be observed by the ASTRO-F/FIS are expected to be distant

TABLE 2.3:  $5\sigma$  detection limits of FIS bands from scanning simulations with a single pixel.

Detection Limits (mJy)	
WIDE-L	40
N170	80
WIDE-S	20
N60	47

galaxies. Since the size of the PSFs at far-infrared wavelengths is relatively large, we expect that the number of sources overlapped within a given PSF will be larger. In such a situation, the source confusion would be important for faint sources. In this section, we consider how the source confusion would affect the observations by the ASTRO-F/FIS.

### Source distribution

The effect of confusion depends on the distribution of sources in the sky and the PSF. We assume that  $N(> S)$ , the number of sources whose flux is greater than flux  $S$ , as a power-law on  $S$ ,

$$N(> S) = N_0(> S_0) \left( \frac{S}{S_0} \right)^{-\gamma}, \quad (2.4)$$

for  $S_{\min} < S < S_{\max}$ , where  $N_0$  and  $S_0$  are normalisation constants. For uniformly distributed sources in Euclidean space,  $\gamma$  is 1.5. If the galaxies experience strong luminosity evolution from active to less active star formation with time,  $\gamma$  will become greater than 1.5. The curved space could also give  $\gamma$  different from 1.5. The analysis of IR galaxy counts by ISO and SCUBA suggests that  $\gamma$  would be greater than 1.5 but lower than 2.5 at around  $\sim 150$  mJy (Puget et al 1999; Franceschini et al.(2001); Pearson(2001); Dole et al.(2001)). Matsuhara et al. (2000) suggested that  $\gamma$  could be steeper than 2.5 based on the fluctuation analysis due to the strong evolution. In

this paper, we examine three cases:  $\gamma = 1.5$ , 2.5, and 3.0. We fixed  $S_{\min} = 10$  mJy throughout the paper. Since there is no divergence due to  $S_{\max}$ , we do not fix this number.

We need to specify the normalisation constants,  $N_0$ , at a given flux  $S_0$ , which is set to be 100 mJy. These constants are determined from IR galaxy counts normalised to Euclidean law [ $N(> S) \propto S^{-1.5}$ ] at 90  $\mu\text{m}$  based on the IRAS survey and the European Large Area ISO Survey (Efstathiou et al.(2000); Franceschini et al.(2001)). In the following cases, though the source count results are different for different bands and galaxy evolution, we assumed that there are 10 sources brighter than 100 mJy per square degree, i.e.,  $N_0(> 100 \text{ mJy}) = 10$ , in every observational band and the SED of all sources are flat within a given FIS band. The number density of sources was estimated to be 316 per square degrees corresponding to 0.2 within a circle of radius of  $W_H$  in LW bands for  $\gamma = 1.5$  with the above normalisation. The density becomes 10-times larger for the case of  $\gamma = 2.5$  and the case of  $\gamma = 1.5$  and  $N_0 = 100$ , and 19 times larger for the case of  $\gamma = 3.0$  and  $N_0 = 60$ . We expect that source confusion becomes important for these distribution. The distribution of sources in the sky is assumed to be uniform Poisson. In this work, we want to check the pure confusion effect for the same distributed galaxies by excluding other factors, e.g., various types of SED, the redshift distribution, the luminosity function and the galaxy evolution. For a comparison, we also check other cases: the Euclidean space with a large normalisation constant ( $N_0 = 100$ ) and an extreme case ( $\gamma = 3.0$ ,  $N_0 = 60$ ) (Matsuhara et al.(2000)).

### Simple estimate of the confusion noise

Although the clustering of sources could also affect the confusion noise, we ignore such a possibility for simplicity. Following Condon (1974) and Franceschini (1989), we obtain the noise due to confusion as

$$\sigma_{\text{confusion}}^2 = \int_0^{x_c} x^2 R(x) dx, \quad (2.5)$$

where  $x [= S h(\theta, \phi)]$  is the intensity,  $x_c$  is a cutoff value, and  $R(x)$  is the mean number of sources within the normalised beam pattern,  $h(\theta, \phi)$ :

$$R(x) = \int_{\Omega_{\text{beam}}} n \left( \frac{x}{h(\theta, \phi)} \right) \frac{d\Omega}{h(\theta, \phi)}, \quad (2.6)$$

where  $n(S)$  is a differential number count.

In this calculation, we use the beam pattern (see figure 2.5), which is obtained from a simulated image of an isolated point source using the FISVI without noises. The beam pattern obtained in this way is somewhat wider than the Compiled PSF due to pixel convolution. We also use the differential number count obtained from the same source distribution assumed in subsection 2.4.2. These considerations are for the purpose of comparing with the results from the photometry in subsection 2.4.3. We list the  $5\sigma$  confusion noise in table 2.4, obtained by using equation (2.5) for  $\gamma = 1.5$ ,  $\gamma = 2.5$ , and  $\gamma = 3.0$ . We also estimated the crowded fields for  $\gamma = 1.5$  by simply increasing  $N_0$  by a large factor, i.e.,  $N_0(> 100 \text{ mJy}) = 100$ . The  $5\sigma$  confusion noise is the same for the wide and narrow bands, because the beam patterns are similar for two bands. Because of differences in the size of beam profiles between long and short wavelengths, the detection limits for LW are higher than those of SW bands. The detection limit by confusion is approximately proportional to  $N_0^{1/\gamma}$ .

The confusion noise in FIRBACK survey by ISO is estimated to be around  $\sigma_c \simeq 45 \text{ mJy}$  (Dole et al.(2001)). In our case, we used the slope of the source distribution as  $\gamma = 1.5$  or  $\gamma = 2.5$  and set the normalisation constant as  $N_0(> 100 \text{ mJy}) = 10$  by using the  $90 \mu\text{m}$  source count result (Efstathiou et al.(2000)). Though the slope of the source count by Dole et al. (2001) is similar to the Euclidean space ( $\gamma = 1.5$ ), the normalisation constant should be different because the source density and the galaxy evolution is different in other bands. Therefore, these discrepancies result from the different normalisation and the cutoff flux ( $S_{\text{min}} = 10 \text{ mJy}$ ).

### 2.4.3 Realistic Simulations

The assumed source distribution of equation (2.4) can be used to simulate the observed sky by the ASTRO-F/FIS. By analysing the simulated images, we can address the

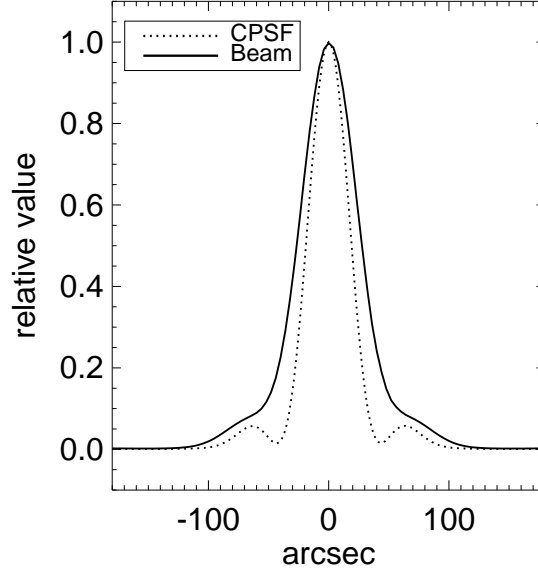


FIG. 2.5: Comparison between the Compiled PSF (dotted) and the beam pattern (solid line) used in calculating the theoretical confusion (WIDE-L). Because we assumed a flat SED for all sources in this simulation, we used one Compiled PSF in the PSF-convolution.

TABLE 2.4:  $5\sigma$  detection limits due to confusion noise based on theoretical estimates.

Band	$\gamma = 1.5$	$\gamma = 1.5$	$\gamma = 2.5$	$\gamma = 3.0$
	$N_0^* = 10$	$N_0^* = 100$	$N_0^* = 10$	$N_0^* = 60$
	(mJy)	(mJy)	(mJy)	(mJy)
WIDE-L	23	108	50	196
N170	24	115	52	204
WIDE-S	12	54	35	123
N60	11	52	34	121

\*  $N_0(> 100 \text{ mJy})$ . Number per square degree.

effects of the various sources of noises to the observation in a more realistic way.

### Realistic simulations

Using the FISVI, we generated two-dimensional images in the FIS bands for two different virtual sky data with different  $\gamma$ . We made two different sets of simulations. One was with the noise levels described in earlier in this section; the other was with the noise reduced to almost a negligible level in order to separate the effects of confusion. The image size for the distributed source simulation is  $8192'' \times 8192''$ . As mentioned in the previous section, we expect that the confusion is important, especially for the cases that  $\gamma$  is greater than 2.5. In figure 6.16, we show an example of the simulated images with the normal level of noise.

We carried out aperture photometry on the simulated images using SExtractor software *v2.0.0* (Bertin & Arnouts 1996). Some influential parameters were optimised for better detection of the source, while the remaining were left intact as default values. We set the threshold in the source detection and the analysis as 3, the size of the photometric aperture as FWHM of beam pattern, and we did not apply a filter for detection. In order to calibrate the output flux, we used the five brightest input sources.

Figure 2.7 shows the distribution of the  $S_{\text{out}}/S_{\text{in}}$  as a function of  $S_{\text{in}}$ , where  $S_{\text{in}}$  and  $S_{\text{out}}$  denote the input flux and the flux obtained by photometry. In the upper-left panel of figure 2.7, we assumed that it is for the case with  $\gamma = 1.5$  and  $N_0 = 10$ , and negligible contribution of photon and readout noise. We also assumed that detected source corresponds to the input source if the position of the detected source lies within  $9''$  for SW bands and  $15''$  for LW bands from the input source location. We found very good correlation between the input and output fluxes, and hence can conclude that the confusion noise is also negligible for this case.

The noise added results for the case with  $\gamma = 1.5$  are shown in the upper-left panel of figure 2.8. The flux uncertainty becomes significant near the estimated detection limits due to photon and readout noise. Below the detection limit, most of the detected sources have an output flux greater than the input flux: This is simply because detection can be possible only when positive noises have been added to the source.

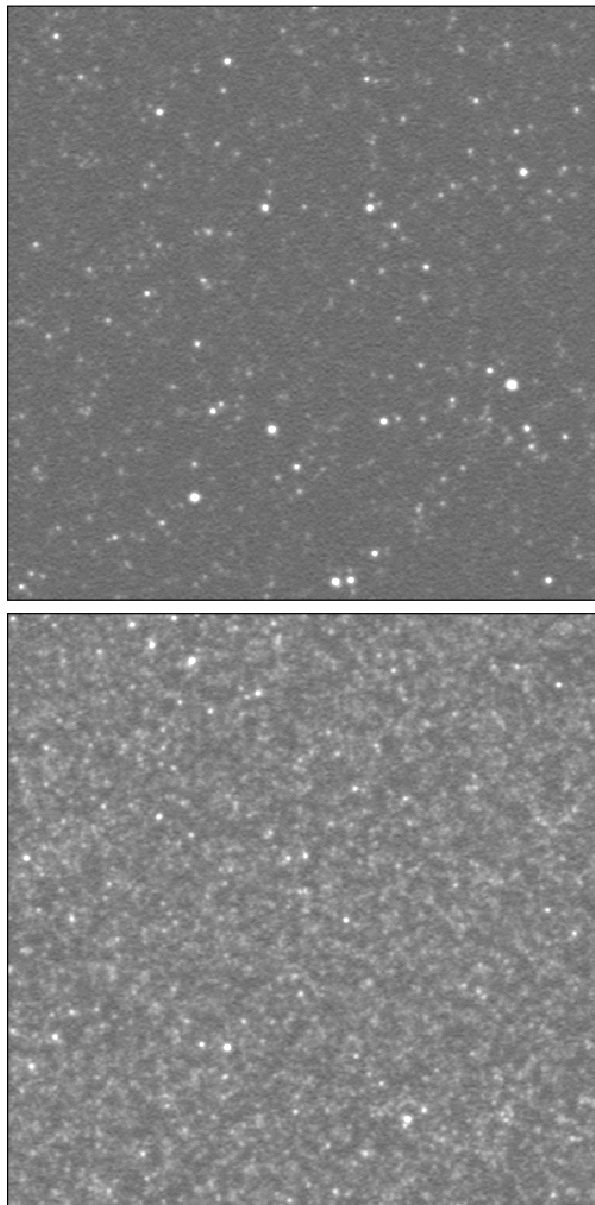


FIG. 2.6: Simulated images in the WIDE-L band for distributed sources. We generated the distributed sources according to the cases of  $\gamma = 1.5$  and  $N_0 = 10$  (upper panel) and  $\gamma = 2.5$  and  $N_0 = 10$  (lower panel). Photon and readout noises are added in these images.

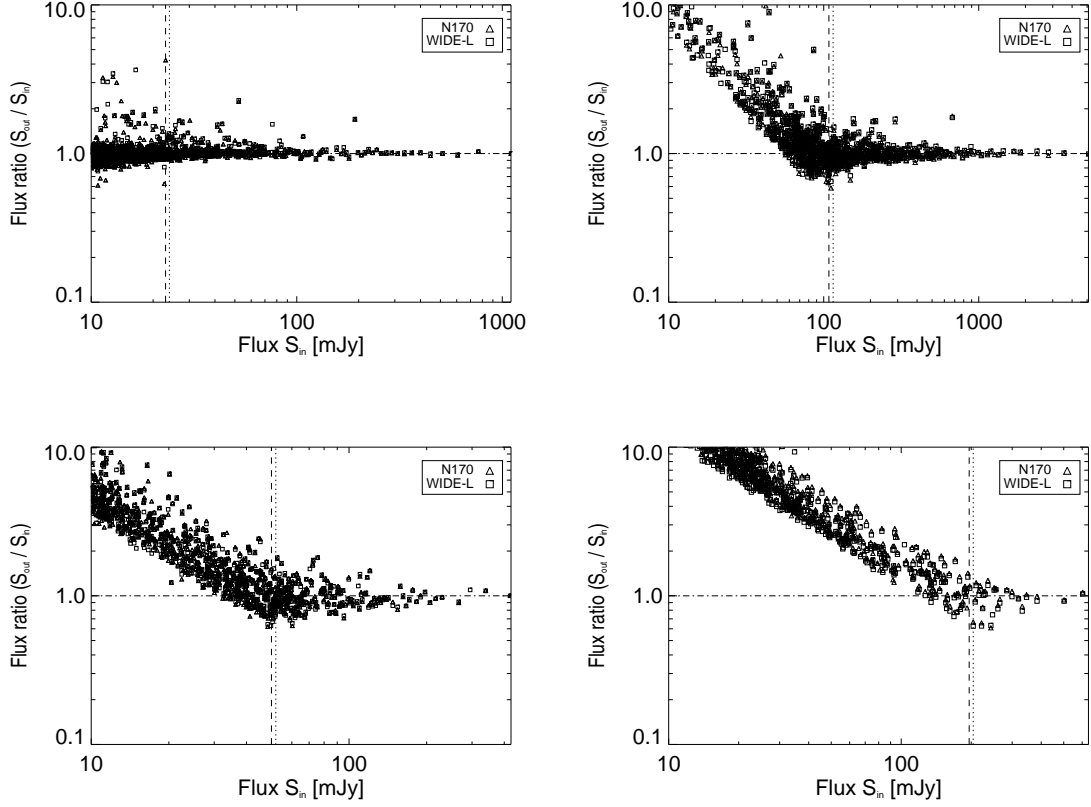


FIG. 2.7: Flux ratio between the input and the output fluxes for extracted and identified sources in LW bands for the case of  $\gamma = 1.5$  and  $N_0 = 10$  (upper left), the case of  $\gamma = 1.5$  and  $N_0 = 100$  (upper right), the case of  $\gamma = 2.5$  and  $N_0 = 10$  (lower left), and the case of  $\gamma = 3.0$  and  $N_0 = 60$  (lower right) without photon and readout noise. The flux in the vertical lines is  $5\sigma$  confusion noises calculated from equation (2.5). The dotted line is for the N170 band and the dashed line is for the WIDE-L band.  $S_{\text{in}}$  and  $S_{\text{out}}$  mean the input flux and the output flux, respectively. As the source confusion is severer, the flux is boosted even in the high flux value.

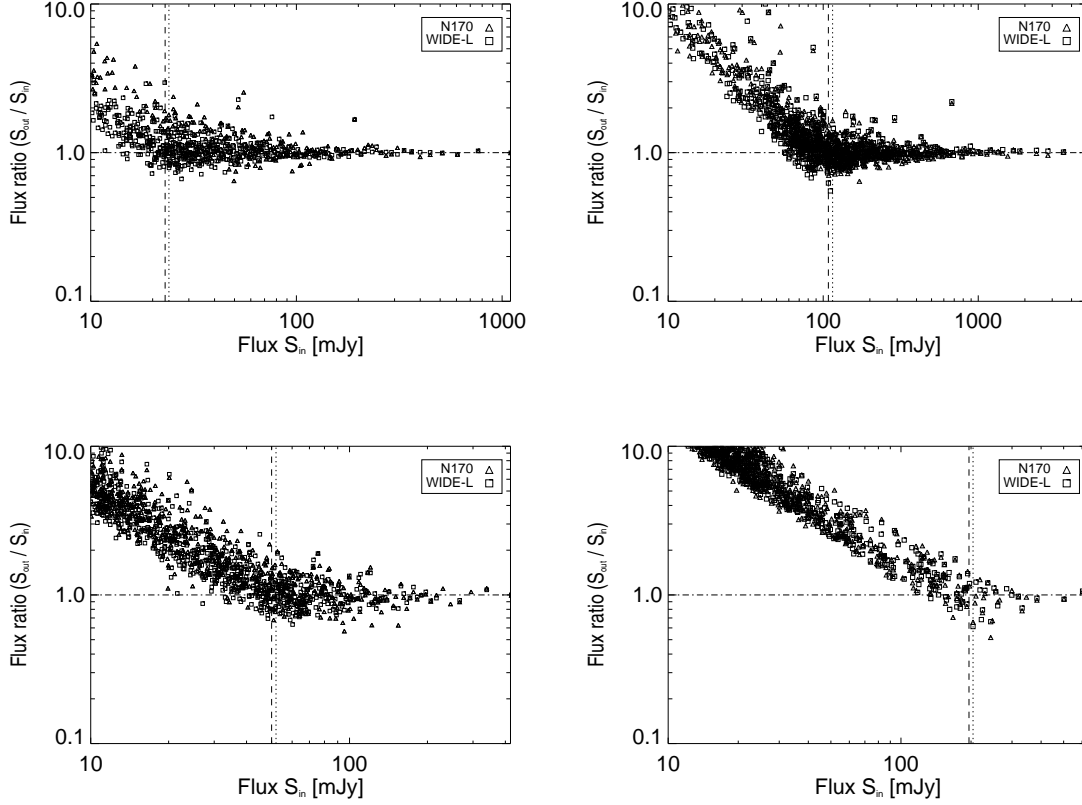


FIG. 2.8: Flux ratio between the input and output fluxes for extracted and identified sources in LW bands for the case of  $\gamma = 1.5$  and  $N_0 = 10$  (upper left), the case of  $\gamma = 1.5$  and  $N_0 = 100$  (upper right), the case of  $\gamma = 2.5$  and  $N_0 = 10$  (lower left), and the case of  $\gamma = 3.0$  and  $N_0 = 60$  (lower right) with the photon and readout noise. See the caption to figure 2.7 for the meanings of the lines and symbols. In the case of including the photon and readout noise, the flux ratio is scattered near the detection limits by photon and readout noise. However, the trend of the boosted flux is similar to the case without noises (see figure 2.7), due to the heavy confusion.

The results with more crowded sources (i.e.,  $\gamma = 2.5$  and  $\gamma = 3.0$ ) are shown in the lower panels of figure 2.7 for negligible noises, and figure 2.8 for normal noises. Even with negligible noises, we find that there are large deviations of the output fluxes from the input fluxes. Thus, the flux uncertainties are mostly caused by the source confusion shown in figure 2.7. Similar to the case dominated by the photon and readout noise shown in the upper-right panel of figure 2.8,  $S_{\text{out}}$  is systematically overestimated for sources below the theoretical confusion limits. Such an upward bias was caused by source confusion; many of the detected sources contain fainter sources within the beam. Actually, the significant upward bias is partially due to the parameter, i.e., threshold, set in SExtractor. First, SExtractor estimates the background fluctuation from each local area. Because we reduce the noise below a negligible level, the calculated background fluctuations are mainly due to many dim sources. The detected sources at low flux surely have a flux above the fluctuation times the threshold; these detected sources cause a significant upward bias. In the case of heavy confusion, the trend of the boosted flux (see the lower panels of figure 2.8) is very similar to the case without noises (see the lower panels of figure 2.7), which means that the faint sources work as the dominant noise.

Figure 2.9 shows the integrated source count results. For a comparison, we also plot the input source distribution. In the case of weak source confusion (i.e.,  $\gamma = 1.5$  and  $N_0 = 10$ ) (upper-left panel of figure 2.9), the source count from a simulated image follows the input source distribution well, except for the faint ends dominated by photon and readout noise. However, the lower panels of figure 2.9 show that the source distribution deviated from the input one due to source confusion. The location of the estimated confusion limit of table 2.4 is also shown in this figure. The observed slope is significantly different from the input slope. The output slope can be 1.5-times larger than the input slope in the case of a crowded source distribution.

As we mentioned in subsection 2.4.2, we generated crowded fields for the case of  $\gamma = 1.5$  by simply increasing  $N_0$  by a large factor, i.e.,  $N_0(> 100 \text{ mJy}) = 100$  and the case of  $\gamma = 2.5$  and  $N_0 = 10$ , to exclude photon and readout noise in order to check the effect of pure source confusion. Because there are no significant difference

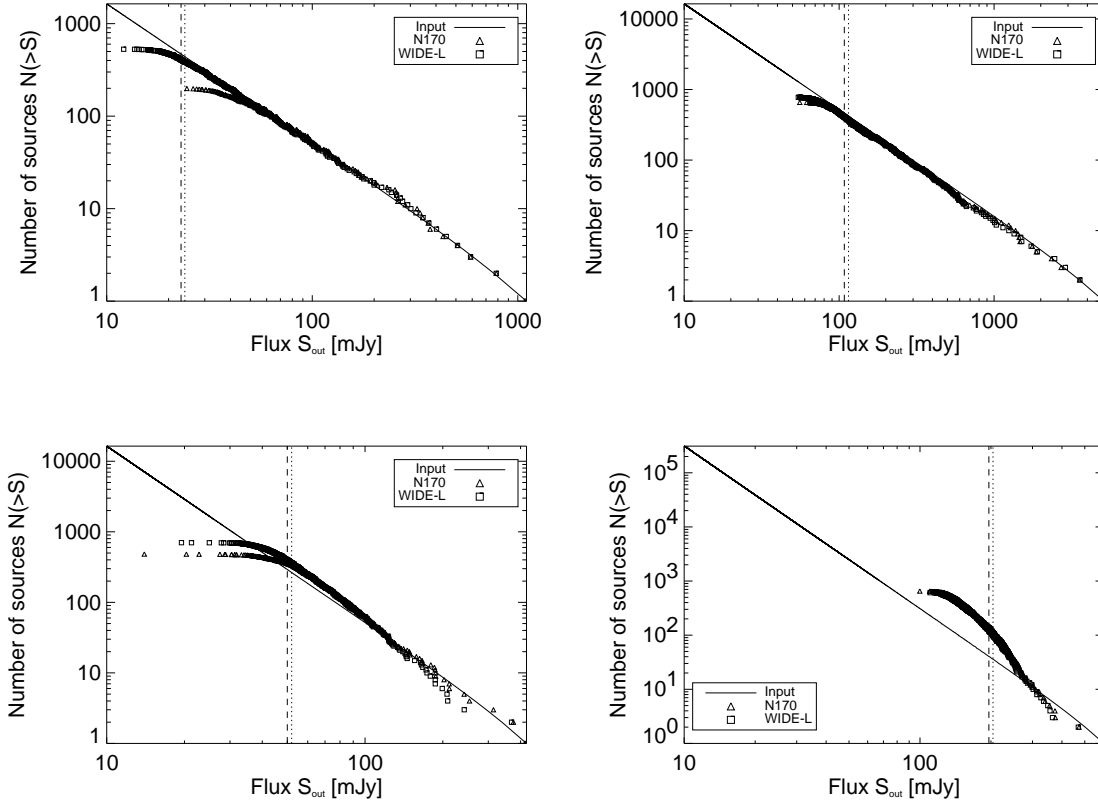


FIG. 2.9:  $N(> S)$  as a function of  $S$  for the case of  $\gamma = 1.5$  and  $N_0 = 10$  (upper left), the case of  $\gamma = 1.5$  and  $N_0 = 100$  (upper right), the case of  $\gamma = 2.5$  and  $N_0 = 10$  (lower left), and the case of  $\gamma = 3.0$  and  $N_0 = 60$  (lower right) with the photon and readout noise.  $N(> S)$  is the number of sources whose flux is greater than  $S$  in the size of the simulated image ( $8192'' \times 8192''$ ). The black solid lines represent the ‘true (or input)’ distribution and symbols show the ‘observed’ results. The vertical lines are the same as figure 2.7. The bend at low  $S$  is mainly due to the detection limit dominated by photon and readout noise. Also, the source confusion makes the slope significantly steeper than the true distribution in the case of the lower panels.

between the case with and without the photon and readout noise, as can be seen in the upper-right panel of figures 2.7 and 2.8, we show the source count result with the photon and readout noise in the upper-right panel of figure 2.9 in comparison with the less-crowded case (upper left). Clearly, the confusion becomes important at around  $S = 100$  mJy for WIDE-L according to a theoretical calculation, but the slope does not change. The change in the slope appears to occur only when the underlying  $N(> S)$  varies rather steeply on  $S$ . The lower-right panel of figure 2.9 shows the case of  $\gamma = 3.0$  and  $N_0 = 60$ , including the photon and readout noise. The slope of the source count is significantly changed by the heavy confusion, and the source detection mainly depends on source confusion.

### Detection limits from simulations

It is not easy to define the detection limits from the simulated data. Since the detection becomes increasingly difficult for sources below the detection limits, we first define the ‘detection correctness’ such that the ratio of the number of correctly detected sources to the number of detected sources from the photometry. We assume that the flux of the correctly detected source is the measured flux from the photometry, and agrees with the input flux within a 20% error. The detection correctness can be near unity for sources well beyond the detection limit, and goes down rapidly below the detection limit. We find that the detection correctness reaches around 0.7 at the estimated detection limit of a single scan. We thus define the location of the 70% detection correctness as the detection limit in our simulated data.

Figure 2.10 show a plot of the detection correctness with the photon and readout noise. We first attempted to estimate the detection limit purely due to source confusion. We arbitrarily suppressed the photon and readout noise by a factor of 100 so that the noise-dominated detection limit would become much less than the lower limit of the source flux of 10 mJy. The resulting detection limits, estimated based on the detection correctness, are summarized in table 2.5. Under this condition, because the source detection is affected by the source confusion and the photometric accuracy, we could obtain similar detection limits in both narrow and wide bands. These numbers are

TABLE 2.5: Detection limits for distributed point sources without photon and readout noise.

Band	$\gamma = 1.5$	$\gamma = 1.5$	$\gamma = 2.5$	$\gamma = 3.0$
	$N_0^* = 10$	$N_0^* = 100$	$N_0^* = 10$	$N_0^* = 60$
	(mJy)	(mJy)	(mJy)	(mJy)
WIDE-L	no confusion	100	58	355
N170	no confusion	105	61	390
WIDE-S	no confusion	45	31	305
N60	no confusion	40	30	278

\*  $N_0(> 100 \text{ mJy})$ . Number per square degree.

similar to those in table 2.4, except for  $\gamma = 1.5$ , where the detection correctness remains larger than 0.7, even for the faintest sources and for the case of the crowded source distribution. This means that the confusion is not important for  $\gamma = 1.5$  and  $N_0(> 100 \text{ mJy}) = 10$ .

Table 2.6 shows the estimates of combined detection limits where the readout noise, the photon noise, and the confusion noise are considered. Since the confusion is not important for the case of  $\gamma = 1.5$  and  $N_0 = 10$ , the detection limit is purely determined by the photon and readout noise. For the case of  $\gamma = 1.5$  and  $N_0 = 100$ ,  $\gamma = 2.5$ , and  $\gamma = 3.0$ , both the source confusion and the other noises contribute to the detection limits. The combined detection limits for this case exceeds both the noise dominated result (table 2.2) and source confusion dominated result (table 2.4). In the case of  $\gamma = 3.0$  and  $N_0 = 60$ , we cannot exactly determine the detection limits because the severe confusion makes the source detection difficult. Too many sources (i.e.,  $\gamma = 1.5$  and  $N_0 = 100$ ,  $\gamma = 3.0$  and  $N_0 = 60$ ) also act as the large amount of the photon noise, which affects in raising the detection limit. Therefore, accurate photometry could be an additional important factor for approaching the theoretical confusion limit in these cases.

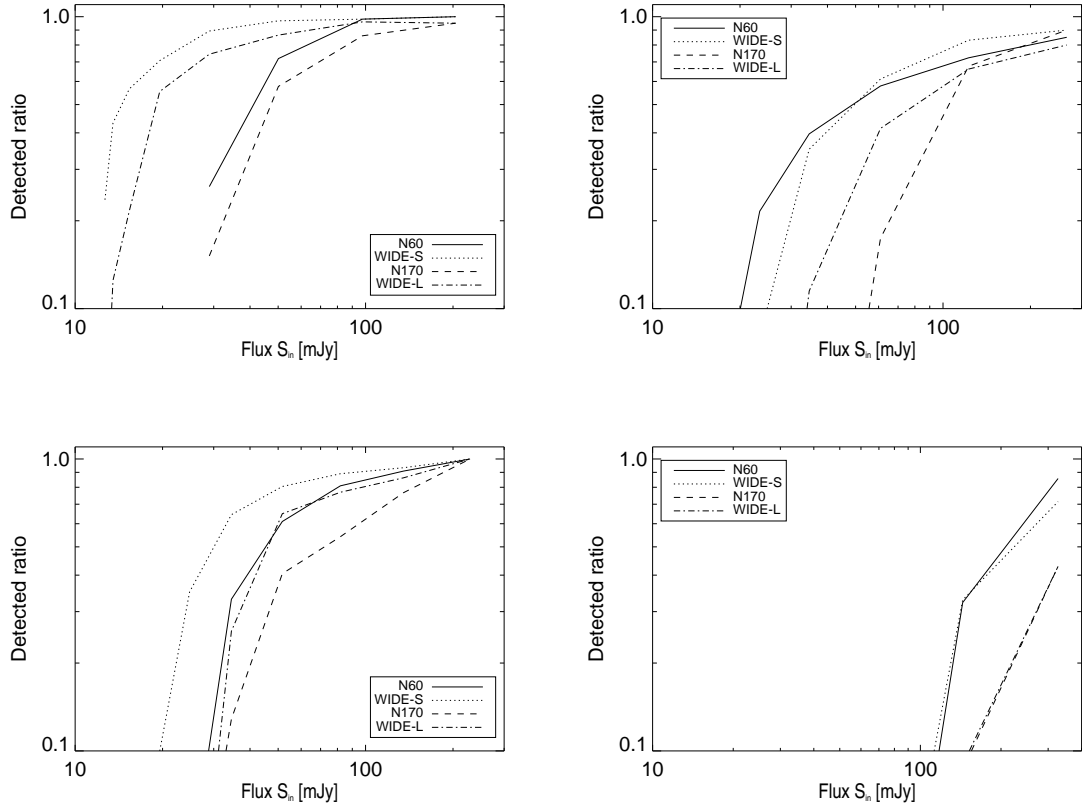


FIG. 2.10: Detection correctness for distributed sources with photon and readout noise for the case of  $\gamma = 1.5$  and  $N_0 = 10$  (top left), the case of  $\gamma = 1.5$  and  $N_0 = 100$  (top right), the case of  $\gamma = 2.5$  and  $N_0 = 10$  (bottom left), and the case of  $\gamma = 3.0$  and  $N_0 = 60$  (bottom right). The detected ratio is the ratio of the number of correctly detected sources (within a 20% error) to the number of detected sources from the photometry. A detected ratio of 1.0 means all detected sources have been correctly detected. The detected ratio for the case of weak confusion (i.e.,  $\gamma = 1.5$  and  $N_0 = 10$ ) rapidly approaches 1.0 in all bands. However, due to heavy confusion, the detected ratio does not approach 1.0 in the case of  $\gamma = 3.0$  and  $N_0 = 60$ .

TABLE 2.6: Detection limits for distributed point sources with photon and read-out noise, taking account of the effects of the performance of the entire system, the brightness of the sky, the telescope emission, and the distribution of sources.

Band	$\gamma = 1.5$	$\gamma = 1.5$	$\gamma = 2.5$	$\gamma = 3.0$
	$N_0^* = 10$	$N_0^* = 100$	$N_0^* = 10$	$N_0^* = 60$
	(mJy)	(mJy)	(mJy)	(mJy)
WIDE-L	26	125	68	440
N170	66	135	115	442
WIDE-S	21	82	40	310
N60	49	92	63	280

\*  $N_0(> 100 \text{ mJy})$ . Number per square degree.

Matsuhara et al. (2000) analysed the ISO data obtained for the high density case ( $\gamma = 3.0$  and  $N_0 = 60$ ) from the fluctuation analysis method, which is different from our photometric method. Because they assumed that the fluctuation is mainly caused by unresolved faint point sources, they could count the number of sources, even in a low flux range.

## 2.5 Summary

We have written observing simulation software, ‘FISVI’, for an upcoming infrared survey mission, ASTRO-F. Utilizing this software, we have estimated the performance of the Far Infrared Surveyor (FIS) onboard ASTRO-F for ideal conditions. We can carry out scanning simulations with a reasonable amount of computing resources by introducing the Compiled PSF. The software can be used to generate virtual data sets for a data-reduction pipeline.

We estimated the detection limits under various circumstances. For the case of a non-crowded source distribution, the readout noise is usually more important than the

photon noise for dark patches of the sky by a factor of 1.3 to 2.5. This means that the bright parts of the sky can be easily dominated by photon noise. The emission from the telescope is less than the interstellar background as long as the telescope temperature remains less than 6 K, but it could contribute significantly to the long-wavelength band if the temperature becomes larger than 6.5 K (see figure 2.4).

In crowded fields, source confusion becomes important in identifying sources. The detection correctness becomes smaller for fainter sources. We have defined the confusion limit in such a way that the number of correctly detected sources within a 20% error becomes larger than 70% of the number of detected sources from photometry. Such a definition of the confusion-dominated detection limit gives very similar values of the confusion limit based on a simple formula. The source confusion becomes larger than the detection limits by photon and readout noise only if the number of faint sources becomes much larger than a simple extension of the IRAS source counts down to around 10 mJy, assuming no luminosity or density evolution. Recent models of source counts based on ISO and SCUBA observations (Matsuhara et al.(2000); Dole et al.(2001); Franceschini et al.(2001); Pearson(2001)), however, predict the source distribution that is subject to significant confusion at the longest wavelength band (WIDE-L). Other bands appear to be noise-limited. The source confusion also could change the slope in  $\log N$ - $\log S$  plots.

In this paper, we have made many simplifying assumptions concerning the sky conditions. The actual sky brightness varies from place to place. The overall statistics of the galaxy counts should be significantly influenced by irregularities of the sky backgrounds. Also, in order to understand cosmological effects, we will consider various types of SED, the luminosity function, and the redshift distribution. The current version of FISVI does not take into account more complicated behaviors of the detectors. These issues will be discussed in forthcoming papers.

---

W.-S. Jeong, J. Sohn, and I. Ahn were financially supported by the BK21 Project of the Korean Government. They also appreciate hospitality while staying at ISAS. This work was financially supported in part by the KOSEF-JSPS corparative program. We thank Myungshin Im, Chris Pearson,

---

and Glenn J. White for reading our manuscript and giving many suggestions.

## REFERENCES

- Bertin, E., & Arnouts, S. 1996, *A&AS*, 117, 393
- Boggs, S. E., & Jean, P. 2001, *A&A*, 376, 1126
- Condon, J. J. 1974, *ApJ*, 188, 279
- Dole, H., et al. 2001, *A&A*, 372, 364
- Efstathiou, A., et al. 2000, *MNRAS*, 319, 1169
- Franceschini, A., Toffolatti, L., Danese, L., & De Zotti, G. 1989, *ApJ*, 344, 35
- Franceschini, A., Aussel, H., Cesarsky, C. J., Elbaz, D., & Fadda, D. 2001, *A&A*, 378, 1
- Garcia, R. A., Roca Cortés, T., & Régulo, C. 1998, *A&AS*, 128, 389
- Herbstmeier, U., et al. 1998, *A&A*, 332, 739
- Jeong, W.-S., et al. 2000, in *Proc. of Mid- and Far-Infrared Astronomy and Future Missions*, ed. T. Matsumoto & H. Shibai, *ISAS Report*, SP14, 297
- Kawada, M. 1998, *SPIE*, 3354, 905
- Kawada, M. 2000, in *Proc. of Mid- and Far-Infrared Astronomy and Future Missions*, ed. T. Matsumoto & H. Shibai, *ISAS Report*, SP14, 273
- Kiss, C., Abraham, P., Klaas, U., Juvela, M., & Lemke, D. 2001, *A&A*, 379, 1161
- Matsuhara, H., et al. 2000, *A&A*, 361, 407

- Matsuura, M., Nakagawa, T., Murakami, H., & Yamamura, I. 2001, ISAS Report, 681, 1
- Murakami, H. 1998, SPIE, 3356, 471
- Nakagawa, T. 2001, in the Proc of The Promise of the Herschel Space Observatory, ed. G. L. Pilbratt, J. Cernicharo, A.M. Heras, T. Prusti, & R. Harris, ESA-SP, 460, 67
- Pearson, C. P. 2001, MNRAS, 325, 1511
- Puget, J. J., et al. 1999, A&A, 345, 29
- Rieke, G. H. 1994, in Detection of Light: from the Ultraviolet to the Submillimeter, ed. K. Visnorsky (Cambridge: Cambridge University Press), pp. 65-67
- Rowan-Robinson, M. 2001, ApJ, 549, 745
- Shibai, H. 2000, in IAU Symp. 204, The extragalactic background and its cosmological implications, ed. M. Harwit & M. G. Hauser (Michigan: Astronomical Society of the Pacific), 455
- Takahashi, H., et al. 2000, SPIE, 4013, 47
- Press, W. H., Teukolsky, S. A., Vetterling, W. T., & Flannery, B. P. 1992, Numerical Recipes in FORTRAN (2nd ed.; New York: Cambridge University Press)
- Hockney, R. W., & Eastwood, J. W. 1988, , Computer Simulation Using Particles (Philadelphia: IOP Publishing Ltd)

## Chapter 3

# Change of Sampling Rate in Scan Mode Observation<sup>‡</sup>

### Abstract

The Far-Infrared Surveyor (FIS) is one of the on-board instruments on the ASTRO-F satellite, which will be launched in early 2004. The first a half year of its mission period of 500 days is dedicated to an all sky survey in four bands between 50 and 200  $\mu\text{m}$ . On the basis of the present hardware specifications and configurations of the FIS, we have written a computer program to simulate the FIS. The program can be used to evaluate the performance of the instrument as well as to produce input for the data reduction system. In this paper, we describe the current status of the program. As an example of the usage of the simulation program, we present the expected observing data for three different detector sampling rates. The functions which should be implemented into the program, in the future, are enumerated.

---

<sup>‡</sup>W.-S. Jeong, S. Pak, H. M. Lee, S. Kim, M. Matsuura, T. Nakagawa, I. Yamamura, H. Murakami, S. Matsuura, M. Kawada, H. Kaneda, & H. Shibai, ‘Simulations of Observations with the Far-Infrared Surveyor: Design Overview and Current Status’, in Proc. of Mid- and Far-Infrared Astronomy and Future Missions, eds. T. Matsumoto & H. Shibai, ISAS Report, SP14, 297

## 3.1 INTRODUCTION

The FIS (Far-Infrared Surveyor, Kawada 1998) is one of the focal plane instruments on-board the ASTRO-F (previously known as IRIS, Murakami 1998). The FIS is equipped with two-dimensional arrays and covers four wavelength bands: N60 (50 – 70 $\mu\text{m}$ ), WIDE-S (50 – 110 $\mu\text{m}$ ), N170 (150 – 200 $\mu\text{m}$ ), and WIDE-L (110 – 200 $\mu\text{m}$ ) (see Table 1 in Kawada 1998). FIS observes in both survey and pointing observation modes. In the survey mode, the detector pixels will continuously scan the sky while the satellite spins around itself on Sun Synchronous orbit with a 100 minute period.

We have developed a computer simulation software of the FIS survey mode observations. The purpose of our simulation software includes:

1. To evaluate the hardware design and its performance;
2. To find optimum observing parameter sets while the satellite is in orbit;
3. To provide input data for the reduction software to be completed before launch.

The FISVI is a virtual instrument program written in IDL to achieve the above objectives. In this paper, we present the simulation for the N170 (150 – 200 $\mu\text{m}$ ) band. Extension to other FIS bands is left as a future work. N170 band uses a  $2 \times 15$  array of stressed Ge:Ga detectors. Under current design of the optical system, one detector element covers a  $44.2'' \times 44.2''$  square shaped area in the sky, and the array is tilted against the scanning direction by  $26.5^\circ$  to achieve Nyquist sampling in the cross-scan direction (perpendicular to the scanning direction).

## 3.2 THE FIS VIRTUAL INSTRUMENT PROGRAM (FISVI)

### 3.2.1 Overview

The first generation of the FIS simulation program is described in Matsuura et al. (2000). The program considered the configuration and size of the detector elements,

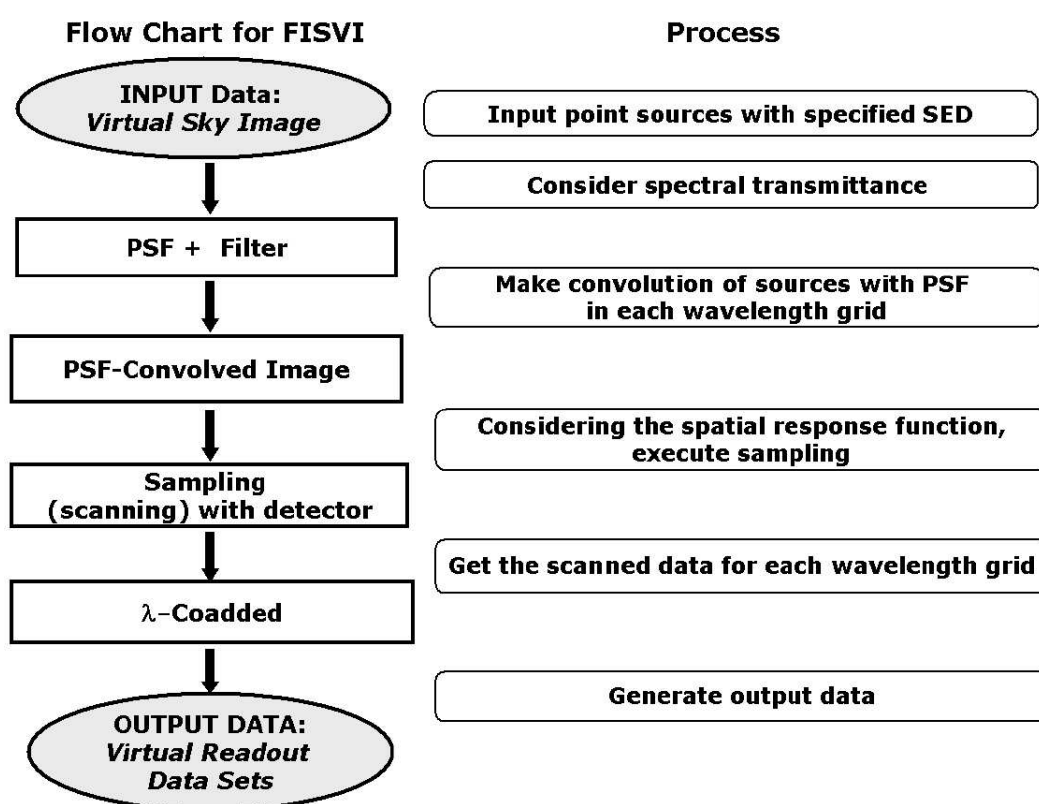


FIG. 3.1: Structure of software and flow chart of the FIS Virtual Instrument Program (FISVI)

sampling rate, and the telescope optics. In the program, the spatial response function, which takes into account the detector shape and the diffraction pattern of the telescope, is calculated for each detector element. A detector element is assumed to have square shaped response function. The (virtual) sky is scanned with the convolution of the diffraction pattern and the detector response. For the point spread function (PSF) of the telescope, the program adopts calculated results using ZEMAX optical simulation software including the shadow due to the baffle around the secondary mirror. The transmittance of the filters and the FIS optical elements, as well as the spectral response function of the detector are newly implemented.

We have written the 2nd version of simulator based on the program by Matsuura et al. (2000). Instead of scanning the sky by the telescope plus detector convolved PSF, we first perform convolution of a virtual sky with the telescope's PSF and then simulate the scanning of the virtual sky with the detector array. This modification improves the calculation speed significantly.

### 3.2.2 Optics and Detector Response

The radiation from the celestial source,  $F_\lambda(\alpha, \delta)$ , where  $\alpha$ , and  $\delta$  are right ascension and declination, respectively, is projected onto the focal plane at  $(x, y)$ . The monochromatic pixel value (energy absorbed by a pixel per unit time per unit wavelength interval),  $P_\lambda(x, y)$ , can be expressed by convolution of responsivity weighted flux with the PSF at a given  $\lambda$ .

The FIS detectors are not located on optical axis of the focal Plane. In the current version, however, we adopted the PSF at the optical axis. The aberrations due to offset from the center as well as the off-axis optics in the FIS will be considered in future.

The spectra of the input sources are taken into account. We need PSFs at arbitrary wavelengths while the PSF is calculated only at  $\lambda = 200\mu\text{m}$ . The necessary PSFs at given wavelengths are obtained by linear scaling in  $\lambda/\lambda_0$  using the computed PSF at  $\lambda_0 = 200 \mu\text{m}$ .

Transmittance of the FIS optics and the filters are included in the program.

Roughly speaking, the sensitivity of the stressed Ge:Ga detector is inversely proportional to the wavelength up to certain cut-off wavelength (e.g., Kazanskii et al. 1977). In the real detector, however, the cut-off is not very sharp and the responsivity drops rather gently from 150 to 200  $\mu\text{m}$ . The measurement by Makiuti et al. (1998) for the responsivity of the detector type to be used for N170 band shows substantial noise mainly due to the difficulties in correcting the filter transmission. Thus we have drawn a smooth curve based on this measurement for our calculation. The result is shown in Fig. 2 as a broken line. The drop toward the long wavelength begins at around 150  $\mu\text{m}$  and the responsivity becomes very small at around 200  $\mu\text{m}$ . The actual spectral response of the detectors for N170 on FIS will be somewhat different from the one we used here because of the uncertainties in the responsivity of the detector, and the curves in Fig. 2 should be considered as tentative. The transmittance of the filter (Takahashi et al. 2000) including the FIS optics is also shown in Fig. 2 as a dotted line, together with the combined responsivity of the filter-detector system as a solid line. Since the detector responsivity is relative value, we normalized the combined responsivity to 1 at the peak value (at around 170  $\mu\text{m}$ ). We note that the combined responsivity of the filter-detector system is narrowly peaked at around 170  $\mu\text{m}$ .

### 3.2.3 Input Data

The input data shown in Fig. 3 consist of 20 point sources of various fluxes. In the current program, we use arbitrary units for the flux. As for the spectral energy distribution (SED) of the sources, we have examined both flat spectra (i.e., constant  $F_\lambda$ , where  $F_\lambda d\lambda$  is the energy flux in  $\lambda \sim \lambda + d\lambda$ ) and Rayleigh-Jeans tail of the black-body spectra (i.e.,  $F_\lambda \propto \lambda^{-4}$ ). We have taken into account the spectral response function of N170, which is shown in Fig. 2, to obtain the final images by adding up monochromatic images at discrete wavelength grids (see §2.4). More realistic SEDs can be accommodated in our program.

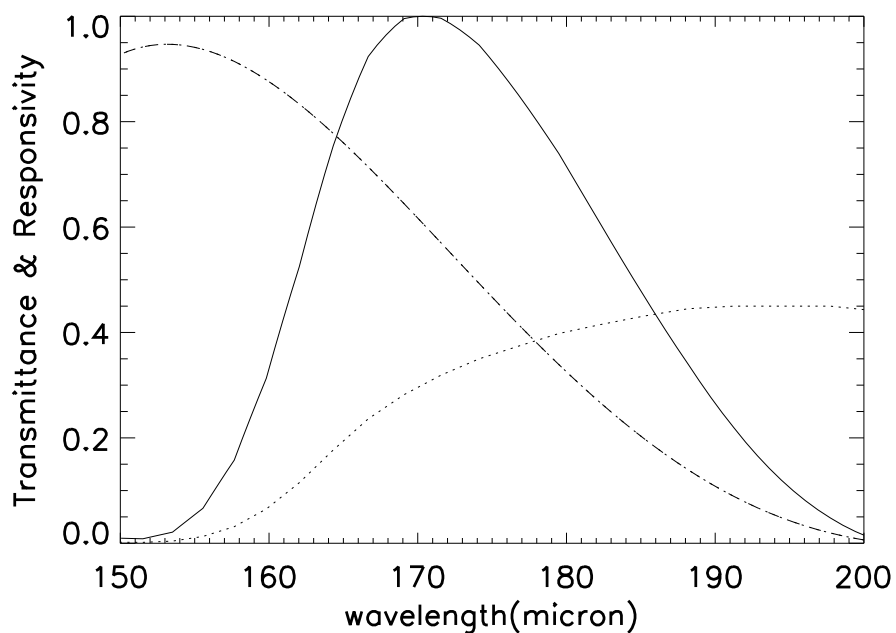


FIG. 3.2: The transmittance of the filter (including the FIS optics: dotted), the responsivity of the detector (dash dotted), and filter-detector combined responsivity as a function of wavelength (solid). The combined response is normalized such that the peak value becomes 1 (at around  $\lambda = 170\mu\text{m}$ ).

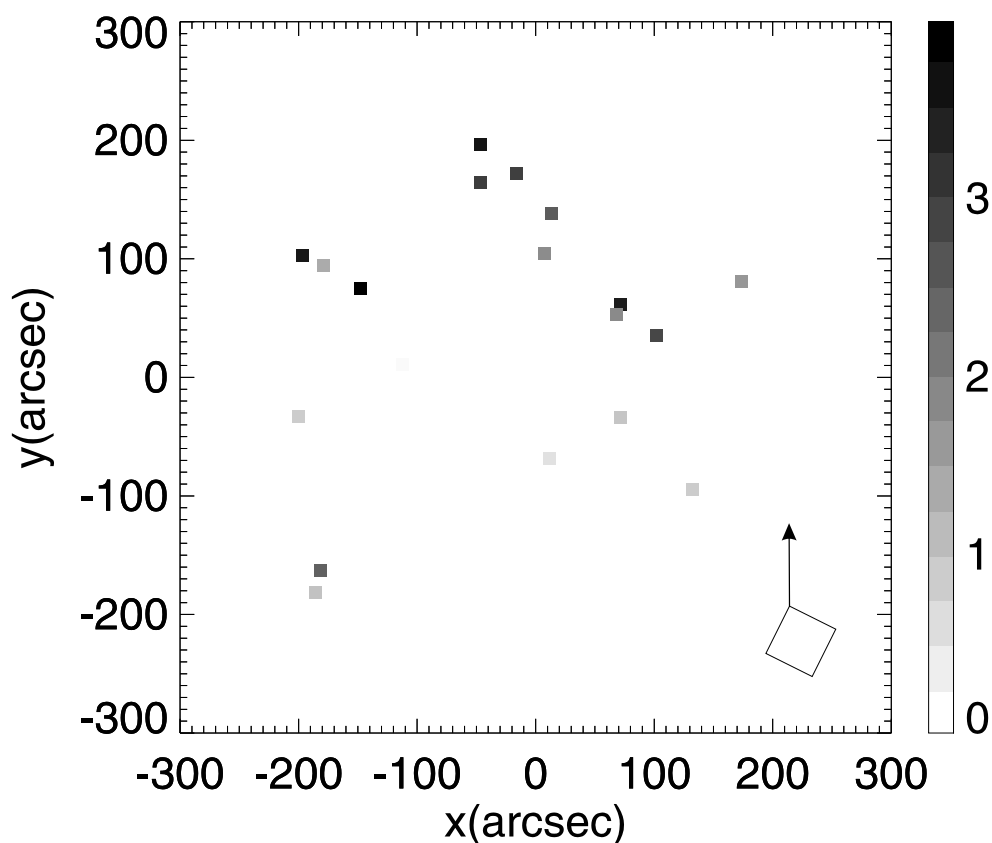


FIG. 3.3: Virtual input data composed of 20 point sources in the sky. These sources are assumed to have either flat spectra (i.e., constant  $F_\lambda$ ) or Rayleigh-Jeans tail of black body spectra (i.e.,  $F_\lambda \propto \lambda^{-4}$ ). The numbers shown in the color bar is the flux in arbitrary units. The tilted square box indicates a detector pixel projected on the sky relative to the scanning direction which is shown as an arrow.

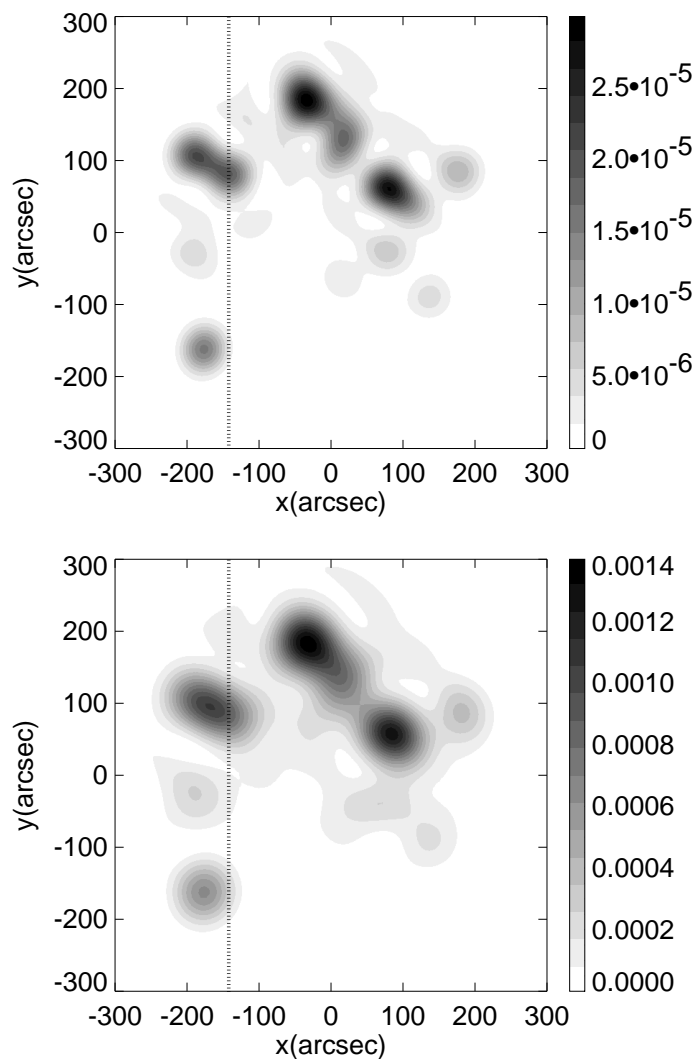


FIG. 3.4: PSF convolved image (in linear scale in brightness) at  $150 \mu\text{m}$  (upper panel) and at  $200 \mu\text{m}$  (lower panel) on the focal plane. The vertical lines at  $x = -142''$  indicate the cuts where we obtained the one-dimensional profiles shown in Fig. 6. The numbers shown along the color bars are the flux densities in arbitrary units.

### 3.2.4 Detector and Readout

The satellite will scan the sky with a speed of  $3.6 \text{ arcmin s}^{-1}$  (see Murakami 1998). We can simulate this by moving the detector arrays on the PSF-convolved image. The photon energy is converted to charges and stored in the charge integrating amplifier. In our program, the readout values during two subsequent sampling steps is obtained by integrating  $P_\lambda(x, y)$  over the time and over the wavelengths. In order to carry out the time integration, we take the pixel values at discrete times separated by small time-steps ( $\Delta t = 1/64 \text{ sec}$ ) to mimic a continuous motion of the detector. Thus, a readout with 16 Hz sampling rate is a summation of pixel values at four different time-steps. The representative position of one readout is assumed to be a mid-point of two positions: one at the beginning and the other at the end of the integration. The wavelength integration ( $\lambda$ -coaddition process) is performed by dividing the entire band into discrete wavelengths with  $\Delta\lambda = 5\mu\text{m}$  interval.

## 3.3 RESULTING IMAGES

We have applied our program to a virtual distribution of 20 point sources over  $10 \text{ arcmin} \times 10 \text{ arcmin}$  area, as shown in Fig. 3, together with one pixel element as a square shaped box. The scanning direction is indicated as an arrow.

In Fig. 4, we have shown the monochromatic images at 150 and 200  $\mu\text{m}$ . Obviously, the image at 150  $\mu\text{m}$  is shaper than that of 200  $\mu\text{m}$  because of the difference in PSF: the diffraction limit at 150 and 200  $\mu\text{m}$  are  $53.9''$  and  $71.9''$ , respectively. Also notice the extended light well outside the bright sources resulting from the outer tail of the PSF. Such features are most clearly seen around a group of sources at  $(x, y) \approx (-40, 180)$  and  $(100, 20)$ .

Actual images obtained by integrating monochromatic ones over  $\lambda$  are shown in Fig. 5. Here we have assumed that, for each source, the integrated flux from  $\lambda = 150$  to 200  $\mu\text{m}$  are the same for flat and Rayleigh-Jeans tail SEDs. We find that these two images are nearly identical. The SED appears to have very little effects on the ‘effective wavelength’, that represents a wavelength of a given band, for N170. This is

mainly because of the narrowness of the combined responsivity of the filters and the detector shown in Fig. 2.

## 3.4 DISCUSSIONS

Our program can be used to achieve the tasks listed in section 1. However, there are still substantial uncertainties in instrumental characteristics such as the spectral response of the detectors. Also the program is in a preliminary stage and more effects are to be taken into account. In this section, we briefly discuss the effects of sampling rate on the observed data and list the necessary works in the future on this program. In the current version, we assumed that the photon flux instantaneously changes into current.

### 3.4.1 Effects of Sampling Rate

The sampling rate should be chosen to optimize the data quality and the amount of data. We have examined three different sampling rates: the nominal (16 Hz), half of the nominal (8 Hz), and twice the nominal (32 Hz). Fig. 6 shows a result of a scan along  $x = -142''$  at two different wavelengths ( $\lambda = 150$  and  $200 \mu\text{m}$ ) in the upper panels. We also show the  $\lambda$ -coadded results for the flat and Rayleigh-Jeans tail SEDs in the lower panels. The low sampling rate generally produces somewhat poorer profiles. Also notice that there are some differences in the one-dimensional profiles between 150 and  $200 \mu\text{m}$  scans. The small peaks at around  $y = -40''$  and  $200''$  are less pronounced in the  $150 \mu\text{m}$  profiles. These regions do not contain any source, and the diffuse components are mainly due to the tail of the PSF. Since the PSF is narrower for shorter wavelengths, we see less diffuse light at  $150 \mu\text{m}$  than at  $200 \mu\text{m}$ .

The difference between the scanned data with 16 and 32 Hz sampling is clearly much smaller than that between 16 and 8 Hz samplings. Therefore, the current choice of nominal 16 Hz sampling appears to be appropriate for FIS observations for the ideal sky. Sampling rate of 8 Hz give substantially distorted image profiles for bright sources. It may be possible to recover some aspects of the sources from under sampled images

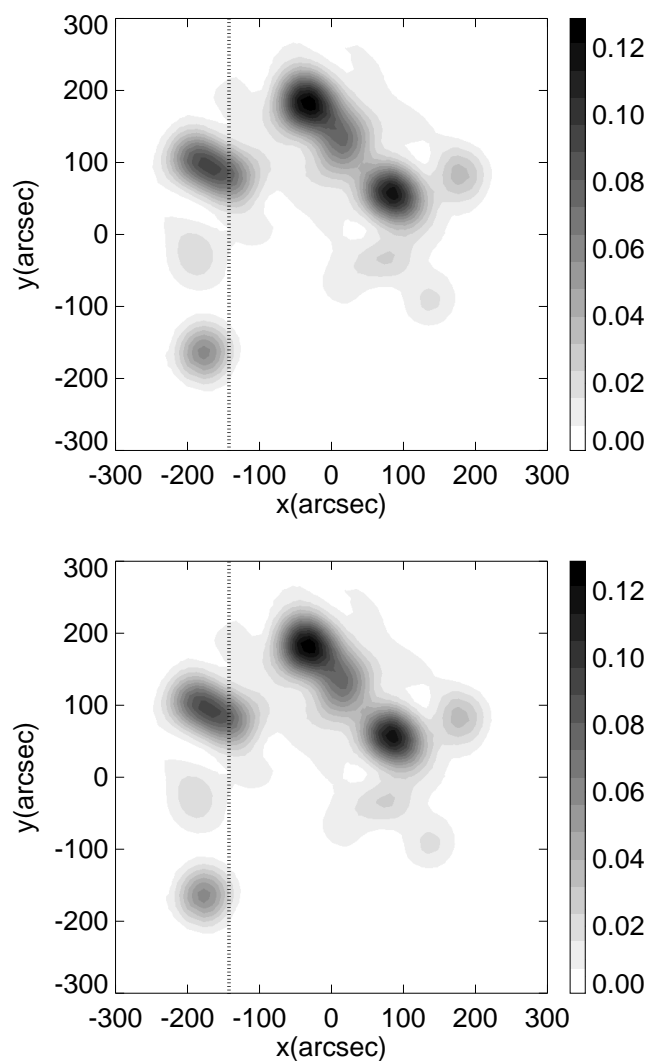


FIG. 3.5:  $\lambda$  - coadded image for flat SED (upper), and Rayleigh-Jeans tail of black body SED (lower). Since the throughout spectral response has a rather narrow width, the effective wavelength is not much sensitive to the spectral shape of the source, and these two images are nearly identical. The numbers shown along the color bars are the flux densities in arbitrary units.

using PSF fitting procedure, but it is beyond the scope of this paper to examine such issue.

### 3.4.2 Future Work

The complex response of the hardware of the FIS has not been fully incorporated in the current version of FISVI. We will embody some more realistic effects in future simulations. For example, spatial response function of the detector is not exactly a box function, especially for unstressed Ge:Ga detector arrays (see Fig. 3 in Hiromoto et al. 1998). The projected shape of the detector is distorted by optical aberrations. The effect of noise should also be taken into account.

The Ge:Ga detector changes its response depending on the incident photons. Due to the transient response, the detector output versus input flux would be a non-linear function. It also affects the apparent detected position of the sources. Okamura (2000) measured the time constants of the transient effects in the laboratory. To correct the transient response is one of the key issues on the ASTRO-F data reduction, and therefore the future program will include such effects.

The charges from the detector are collected at the charge integrating amplifier. The integrated charges are discharged by resetting every 2 – 5 minutes. Longer discharge intervals are preferred because each reset needs a short pause to settle down. However, the integrating amplifier can be saturated, if the detector sees a bright source. Thus we should find an optimum mode by simulating more realistic sky data and correct values for the optics-detector combined sensitivities.

Finally, the effects of cosmic ray hitting will have to be included in the program. The effects of cosmic ray hitting are: (1) creation of a sharp spike (glitch) and an associated after effect and (2) changes in response of the detector in both short and long time scales. The effects may differ depending on the nature of imparting particle, the energy, and the location of the impact. Proper implementation of these effects into the simulation program will help us to investigate how to detect and correct the spikes and tails, and to optimize the curing method of detector response change after

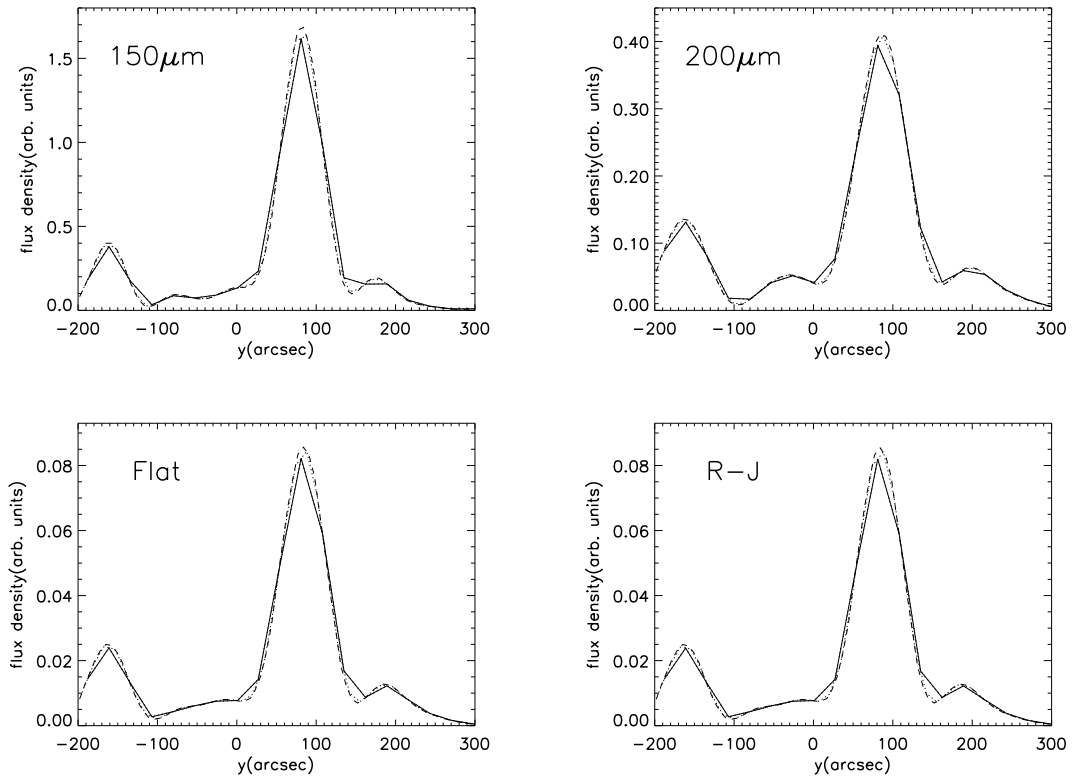


FIG. 3.6: The brightness distribution along one-dimensional cut shown in Fig. 3 with different sampling rates (8, 16 and 32 Hz) at 150 (upper-left), and 200  $\mu\text{m}$  (upper-right), respectively. The lower panels show the same for  $\lambda$ -coadded scanned data of flat (lower-left) and Rayleigh-Jeans tail of blackbody (lower-right) SEDs, respectively. The solid, dotted, and broken lines represent 8 Hz, 16 Hz, and 32 Hz sampling results, respectively. Clearly 8 Hz sampling gives rather poor information regarding the peak positions and fluxes.

the passage of South-Atlantic Anomaly (SAA) where most of the cosmic ray hitting will take place.

---

This work was financially supported in part by the BK21 Project of the Korean Government, and in part by the KOSEF-JSPS corporative research program. M.M. is supported by the research fellowship of JSPS for the Young Scientists.

## REFERENCES

- Hiromoto, N., Fujiwara, M., Shibai, H., Hirao, T., Nakagawa, T., and Kawada, M. 1998, SPIE Proc. 3354, p48
- Kawada, M. 1998, SPIE Proc. 3354, P905
- Kazanskii, A. G., Richards, P. L., and Haller, E. E., 1977, Appl. Phys. Lett., 31, 496.
- Makiuti, S., Doi, Y., Shibai, H., Hiromoto, N., Nakagawa, T., Kawada, M., Okumura, K., and Okuda, H. 1998, SPIE Proc. 3354, p261
- Matsuura, M. et al. 2000, in preparation
- Murakami, H., 1998, proc. SPIE 3356, p471
- Okamura, Y. 2000, Master Thesis, University of Tokyo
- Takahashi, H., et al. 2000, SPIE Proc. 4013, p47



# Chapter 4

## ASTRO-F/FIS Observing Simulation Including Detector Characteristics<sup>§</sup>

### Abstract

We have examined the effects of transients, glitches caused by cosmic ray hits, and the crosstalk of the far-infrared detector arrays on-board ASTRO-F on its survey mode data. We used simple model fits to laboratory measurements for the transients and glitch profiles. We also tested several correction methods, based on these models, to recover the original signal.

### 4.1 INTRODUCTION

ASTRO-F is the next generation infrared space telescope of the Japanese Institute of Space and Astronautical Science due for launch in early 2004. One of its instruments, the Far Infrared Surveyor (FIS) will map the entire sky in four bands using short wavelength (SW) and long wavelength (LW) detector arrays (Murakami 1998; Shibai

---

<sup>§</sup>W.-S. Jeong, S. Pak, H. M. Lee, T. Nakagawa, M. Kim, S. H. Oh, H. Kaneda, S. Makiuti, M. Shirahata, S. Matsuura, M. A. Patrashin, C. Pearson, & H. Shibai, *Adv. Space Res.*, in press

2000; Nakagawa 2001). We have developed a suite of software with an aim to simulate the FIS observations (Jeong et al. 2000; 2003; 2004). Such software will be used for many different purposes: e.g., to check the hardware performance for realistic sources, to design the optimal observational modes, and to generate virtual data that can be used in constructing the data reduction software.

The FIS uses two Ge:Ga arrays: unstressed for SW and stressed for LW. It is well known that these arrays exhibit many non-ideal characteristics such as a slow transient response, non-linear crosstalk among detector pixels, and susceptibility to high energy radiation (Matsuura et al. 2003). The correction of these effects is essential for the data reduction process. We can examine the consequences of such complex effects by using our simulation software. In this paper, we present results of simulations that include glitches by cosmic rays, detector transients, and crosstalk between adjacent detector pixels. The simulated raw data show how serious these effects could be on the real observations. By carefully analysing the simulated data, we suggest appropriate methods to remove such effects.

## 4.2 DETECTOR RESPONSE

Ideally, the detector should record the incoming signal instantaneously with a steady responsivity and there should be no interference from nearby pixels. However in practice, the anomalous behaviour of a detector and unstable conditions of space environment cause changes in the detector response.

Since the detectors do not respond instantaneously to an incoming signal (e.g. photon), the output signal has different shape from the input in the scanning data. This is known as the transient behaviour of the detector. The right panel of Figure 5.1 shows clearly that the transient shifts the peak in time, lowers the peak and produces a long tail after the peak. The transient is usually characterized by a time constant, but this constant can in fact vary with the strength of input signal.

A small fraction of the charge carriers, generated in a particular detector by the incident photons, could leak into neighboring pixels due to lateral diffusion (Rieke

1994). This is the simplest type of the stationary crosstalk which results in a blurring of the signal as shown in the right panel of Figure 5.1. The crosstalk does not change the position of the peak but it makes the peak lower and Point Spread Function (PSF) wider.

In orbit, high energy particles often hit the detectors producing glitches in the time series data. After a cosmic ray hit, the responsivity of a detector becomes much higher than the nominal value for an extended period. We consider these three effects: transients, crosstalk, and glitches in the observing simulations of ASTRO-F/FIS, based on the laboratory measurements of these effects. Note, we have not taken into account the change of responsivity after a cosmic ray hit because we require more laboratory data to model this effect.

## 4.3 MODELING OF DETECTOR RESPONSE

In order to simulate the detector response, it is useful to model the laboratory data by simple functions.

### 4.3.1 Transients

The laboratory data for transients (and also its after effect: see below) can be represented by several different models: examples being a one- or two-component Lari model (Lari et al. 2001), or a one- or two-component exponential model. Although these models have quite different functional forms, the differences in the model response are very small. Therefore, we employed the two-component exponential model which has the following simple form for the response function,  $r(t)$

$$r(t) = \left(1 - \sum_{i=1}^2 B_i\right) \delta(t - t_0) + \sum_{i=1}^2 \left\{ \frac{B_i}{\tau_i} \exp\left[-\frac{t - t_0}{\tau_i}\right] \right\}, \quad (4.1)$$

where  $\delta(t)$  is a delta function,  $t$  is the time,  $\tau$  is the time constant and  $B$  is the contribution of the transient component. The detector readout is an integration of  $r(t)$  times the input signal  $f(t)$  from  $t_0$  to  $t$ . Thus the readout at  $t$  can be computed

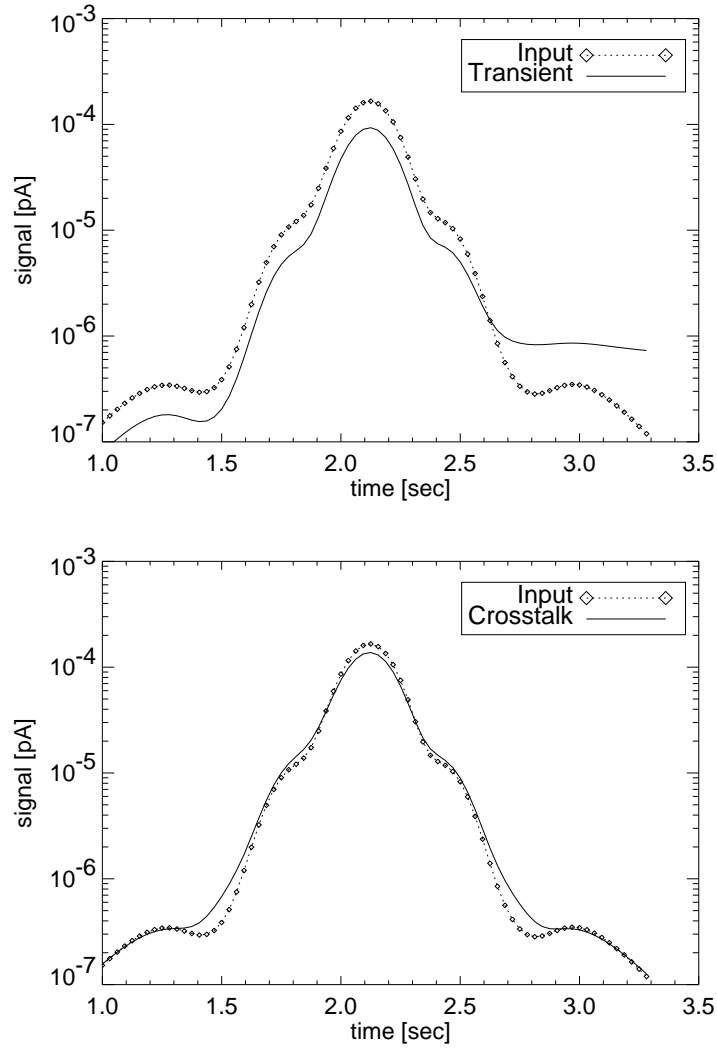


FIG. 4.1: Profiles of the point source in simulated scans measured by an ideal detector and detectors exhibiting the slow transient response (left panel), and the crosstalk due to lateral diffusion (right panel).

from  $R(t) = \int_0^t f(t-u)r(u)du$ , where  $u = t - t_0$  and  $u \geq 0$ . The four parameters in Eq. 4.1 are listed in Table 4.1. The time constants and the “contribution constants” depend on the amount of photocurrent through the detector.

TABLE 4.1: Time-constants and contributions of transient component (Kaneda 2002)

Parameters	Time-constant ( $\tau$ ) (sec)	Contribution of Transient Component (B) (pA)
$\tau_1, B_1$	$9.0 \times J^{-0.79}$	$0.154 \times J^{0.06}$
$\tau_2, B_2$	$1.11 \times J^{-0.35}$	$0.177 \times J^{-0.08}$

J: photocurrent [pA]

### 4.3.2 Stationary Crosstalk

We model the crosstalk in the simulation by transferring some fraction of the integrated charge to nearby pixels. Based on laboratory data, we assume a response where 20% of the pixel value goes to adjacent pixels and 5% goes to nearby pixels in diagonal direction in the SW bands. For the LW bands, 5% goes to adjacent pixels and 1% goes to diagonal pixels (Matsuura et al. 2003). The crosstalk causes the Full Width at Half Maximum (FWHM) of the image to increase by 15% in the SW bands and 5% in the LW bands, respectively. Since we also apply this crosstalk response to the marginal pixels, i.e., a pixel located at the end of a row or column, this gives some amount of flux to the surrounding eight pixels including empty pixels, therefore will be a loss of flux of  $\sim 10\%$  in the SW bands and  $\sim 3\%$  in the LW bands, respectively.

### 4.3.3 Glitches

From an extensive analysis of glitches with various models (Kim et al. 2002, private communication), both the Lari models, and the exponential models reproduce the profiles of low energy glitches, while the Lari model is the most appropriate for high

energy glitches. In our simulation, however, we employed a one-component exponential model for simplicity.

Through the analysis of data from the Far-Infrared Line Mapper (FILM) onboard the Infrared Telescope in Space mission (IRTS) (Murakami et al. 1996), we have classified glitches into four types, according to their profiles. In this simulation, we simplify the parameters which describe the shape of a glitch and assume that all glitches can be represented by the following equation,

$$S(t) = H_1\delta(t - t_0) + H_2 \exp\left[-\frac{t - t_0}{\tau}\right], \quad (4.2)$$

where  $S(t)$  is the signal,  $H_1$  and  $H_2$  are the heights of the glitch for the delta function and the exponential component, respectively,  $t_0$  is the event time of a glitch, and  $\tau$  is the time constant. We assume that the heights of the glitches ( $H_1$ ,  $H_2$ ) follow a Gaussian distribution whose mean and dispersion are listed in Table 4.2. Table 4.2 also lists the other parameters of Eq. 4.2 for the four glitch types considered. Since we do not know exactly how the responsivity changes after a glitch, we assume that the responsivity remains constant irrespective of a glitch in this work. When more extensive data sets become available, we will also consider these response changes.

## 4.4 RESULTS

### 4.4.1 Simulation Data

Based upon our models and using laboratory data, we have simulated the transient response, the glitches and the crosstalk for the ASTRO-F/FIS simulation software. Figure 5.2 shows the effect of the transient (a), crosstalk (b), and glitches (c and d). The transient causes a long tail along the scan direction. The effect of the crosstalk is to blur the image. The glitches appear as bright knots, or narrow and long bright lines if their strength is very high.

Actual observational data would be even more complicated, as these effects would occur together. In Figure 5.3, we display the simulated images of an artificial sky

TABLE 4.2: Parameters for four types of glitches

Type	Rate (sec/glitch)	$H_1$ (mean, $\sigma$ ) (fA)	Cutoff for $H_1$ (fA)	$H_2$ (mean, $\sigma$ ) (fA)	Cutoff for $H_2$ (fA)	$\tau$ (sec)
Type A <sub>+</sub> <sup>1</sup>	250	(10, 8.5)	> 5	-	-	-
Type A <sub>-</sub> <sup>2</sup>	1000	(-6, 7)	< -5	-	-	-
Type B	1800	(10, 8.5)	> 5	(15, 12)	> 2	3
Type C	500	(10, 8.5)	> 0	(-15, 12)	< -2	1
Type D	80000	(200, 150)	> 5	(35, 30)	> 10	300

<sup>1</sup> positive type of glitch

<sup>2</sup> negative type of glitch

covering  $1^\circ \times 1^\circ$  area without (left panel) and with (right panel) detector characteristics. In these images, we use a power-law relation for the point source distribution with a power index  $\gamma = 1.5$  and a normalisation constant  $N_0 = 10$  which corresponds to negligible source confusion (see Jeong et al. 2003 for details). The real task of data reduction is to remove these effects as effectively as possible. Below we discuss how we can eliminate such spurious effects.

#### 4.4.2 Correction for the Detector Characteristics

In order to correct for the transient, we need to know the transient response function. We assume the same model of  $r(t)$  used for the generation of data for the correction process. Since we know the incoming photon flux in the time sequence, we can estimate the leakage signal from the integration of the transient response by fitting the signal and finding the model parameters of the transient for each time sequence. We can therefore compensate for the signal affected by transient with these leakages for each time sequence.

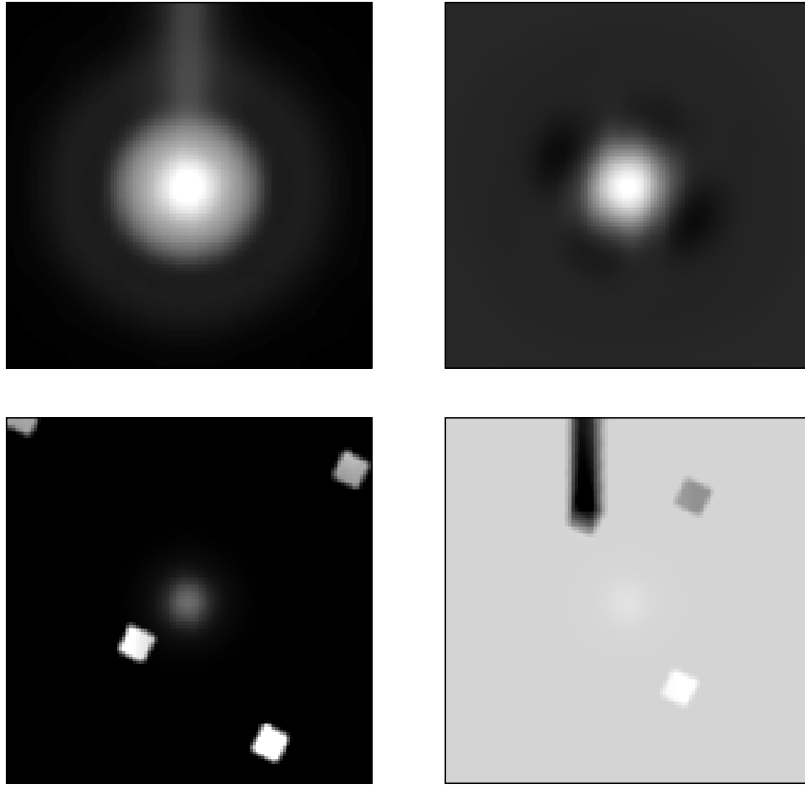


FIG. 4.2: Reconstructed image including transients (a), crosstalk (b) and glitches (c and d). After passing through the center of the source, we can see the tail of a signal (a). Panel (b) shows the residual image between the original image and the image including the crosstalk. Due to the high strength of the glitches, the shape of both the pixel and the glitch appear distinctively in the images (c and d).

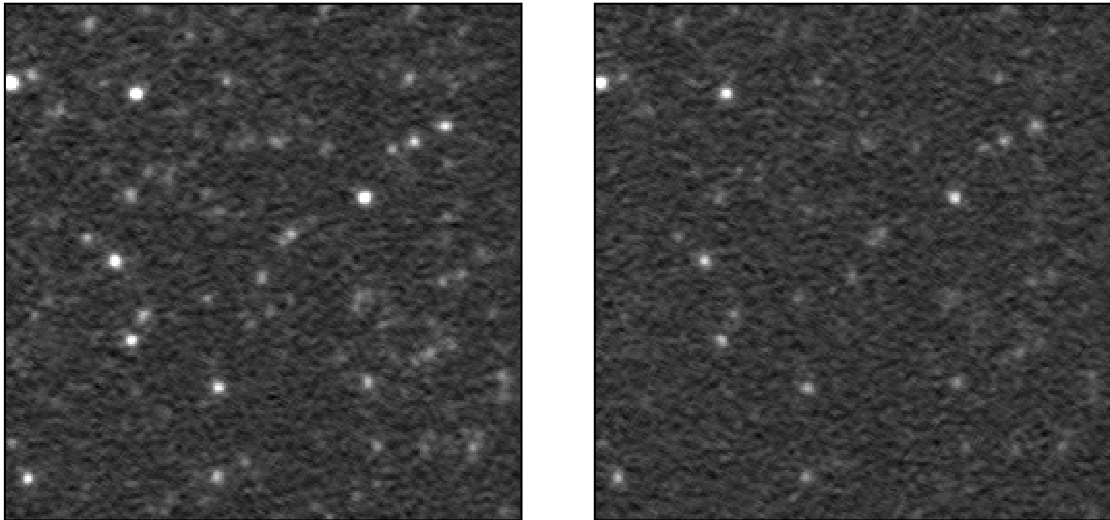


FIG. 4.3: Simulated  $1^\circ \times 1^\circ$  images with many sources. The left panel is the image without the detector characteristics. The right panel is the image including the detector characteristics.

Glitches and crosstalk are easier to recover. In the case of the glitches, we corrected them by replacing the corrupted signal by that of the other unglitched pixels passing through the same position. For the crosstalk effect, we simulate the crosstalk with a constant response for the surrounding pixels. Since we assumed that a constant fraction of a signal has leaked due to the crosstalk effect, we approximately correct it by collecting the same fraction of the signal from the surrounding pixels. For a more realistic correction, an iterative process should be applied. In practice, the correction accuracy of the transient and the crosstalk effects are determined by the consistency of the model parameters and the noise because the actual behavior of the detector may not exactly follow our simple model.

We have applied the above mentioned process to the simulated data shown in Figure 5.3. We then carried out aperture photometry on both the image affected by the detector characteristics and the corrected image using the SExtractor software *v2.0.0* (Bertin & Arnouts 1996) in order to check the accuracy of our corrections.

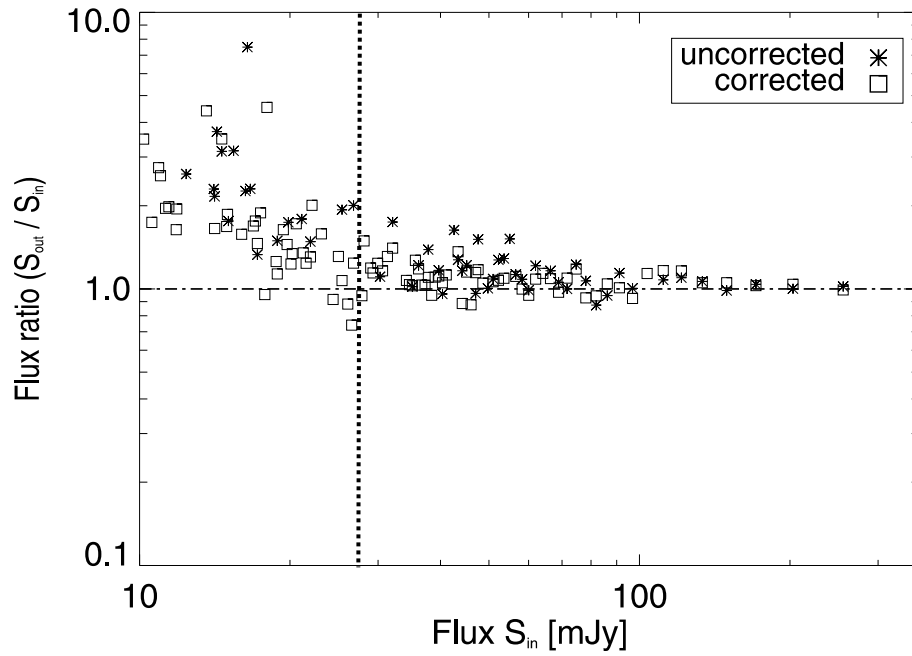


FIG. 4.4: Ratio of the output flux to the input flux. The asterisk symbols show the detected sources in the image including the detector characteristics, and the rectangles show the detected sources in the image after correcting for the detector characteristics. The vertical dotted line shows the estimated  $5\sigma$  detection limit.

Figure 5.4 shows the ratio of the output flux to the input flux, for the extracted and identified sources. For the purpose of calibrating the output flux, we used the five brightest input sources. Hence, the flux ratio of the bright sources is around 1.0 for the photometry on the image including the detector characteristics. At lower flux levels (below 20 mJy), the detected sources are limited by the photon and readout noise. In the case of the uncorrected image, the number of detected sources is 10% lower than those in the corrected image. In addition, the corrected image gives a much better result down to the detection limit.

## 4.5 SUMMARY

We have carried out simulations including transients, glitches and crosstalk effects for the detectors of ASTRO-F/FIS. We have employed simple models for these effects based on laboratory measurements. The corrections were applied to the simulated time series data, by adopting the same models which were used for generating the detector characteristics. Though we could accurately recover the input flux down to the detection limit, the actual behavior of the detector is affected by a combination of many detector characteristics that do not follow simple models. The change of the detector responsivity after a glitch is also an important issue for the data reduction process. We will investigate these issues more deeply in forthcoming works.

---

W.-S. Jeong, M. Kim, and S. H. Oh acknowledge the visiting fellowship by the BK21 Project of the Korean Government. This work was financially supported in part by the KOSEF Grant No. R14-2002-058-01000-0. The ASTRO-F project is managed and operated by the Institute of Space and Astronautical Science (ISAS), Japan, in collaboration with groups in universities and institutes in Japan as well as with Seoul National University, Korea. We thank André Fletcher in Korea Astronomy Observatory for help with editing this paper.



# REFERENCES

- Bertin, E., & S. Arnouts, 1996, *A&AS*, 117, 393
- Jeong W.-S., S. Pak, H. M. Lee, et al., 2000, in *Proc. of Mid- and Far-Infrared Astronomy and Future Missions*, eds. T. Matsumoto & H. Shibai, ISAS Report SP14, 297
- Jeong W.-S., S. Pak, H. M. Lee, et al., 2003, *PASJ*, 55, 717
- Jeong W.-S., S. Pak, H. M. Lee, et al., 2004, *Adv. Space Res.*, in press
- Kaneda H., Y. Okamura, and T. Nakagawa, 2002, *Adv. Space Res.*, 30, issue 9, 2105
- Kim M. et al., 2002, private communication
- Lari, C., F., Pozzi, C., Gruppioni, et al., 2001, *MNRAS*, 325, 1173
- Matsuura, S., Y., Isozaki, M., Shirahata, et al., 2003, *SPIE Proc.*, 4850, in press
- Murakami, H., M., Freund, K., Ganga, et al., 1996, *PASJ*, 48, L41
- Murakami, H., 1998, *SPIE Proc.*, 3356, 471
- Nakagawa, T., 2001, in the *Proc. of The Promise of the Herschel Space Observatory*, eds. G.L. Pilbratt, J. Cernicharo, A.M. Heras, T. Prusti, & Harris, ESA-SP 460, 67
- Rieke, G. H., 1994, in *Detection of Light: from the Ultraviolet to the Submillimeter*, Cambridge University Press, Cambridge
- Shibai, H., 2000, in *The extragalactic background and its cosmological implications*, eds. M. Harwit & M.G. Hauser, IAU Symp. No. 204, 455



# Chapter 5

## Simulations of Cosmological Observations with ASTRO-F/FIS<sup>¶</sup>

### Abstract

The Far-Infrared Surveyor (FIS) is one of the focal-plane instruments on the ASTRO-F mission which will be launched in early 2004. The purpose of the FIS is to perform an all-sky survey in the wavelength range 50 – 200  $\mu\text{m}$ . We are developing a suite of software that simulates the observations with this instrument to check the performance of the ASTRO-F/FIS as a whole and to prepare input data sets for the data analysis and reduction software prior to launch. The detection limit of the FIS is affected by many factors: the performance of the entire system, the brightness of sky and telescope emission, readout process, and the distribution of the celestial sources. The input model for FIS simulator consists of a catalogue of extragalactic point sources generated from the luminosity function at 60  $\mu\text{m}$ , and a redshift distribution incorporating pure luminosity evolution ( $\Omega_0 = 1$ ,  $\Lambda = 0$ ). We present the expected source count results from the FIS survey and estimate the limiting redshift as  $\sim 2.5$  in the Band at 50 – 110  $\mu\text{m}$  and  $\sim 3$  in the Band at 110 – 200  $\mu\text{m}$ .

---

<sup>¶</sup>W.-S. Jeong, S. Pak, H. M. Lee, T. Nakagawa, M. Watanabe, M. Kawada, H. Shibai, C. Pearson, & M. Rowan-Robinson, Adv. Space Res., in press

## 5.1 INTRODUCTION

The ASTRO-F (previously known as IRIS) is the second Japanese space mission for infrared astronomy which will be launched in early 2004 (Murakami 1998; Shibai 2000; Nakagawa 2001). The major task of this mission is to carry out an all sky survey using the Far-Infrared Surveyor (FIS), in four far-infrared bands, i.e., N60 ( $50 - 75 \mu\text{m}$ ), WIDE-S ( $50 - 110 \mu\text{m}$ ), N170 ( $150 - 200 \mu\text{m}$ ), and WIDE-L ( $110 - 200 \mu\text{m}$ ). The detailed hardware specifications of the FIS are described in Kawada (1998; 2000).

The performance of ASTRO-F/FIS can be represented by the effective detection limit for faint sources which are mostly distant galaxies and seen as point-like sources. There are several factors contributing to the effective detection limits. The sensitivity of the detectors (e.g., read noise) and the entire telescope system (e.g., photon noise of the telescope emission) allows only sources brighter than a certain threshold to be reliably measured. In addition, the structure of the cirrus emission from the Galaxy contributes to the photon noise and the sky confusion noise. Moreover, the measurement of the brightness of a source can be further influenced by neighboring sources if more than one source lies within a single beam of the telescope. The final detection limit should thus depend on the performance of the entire system, the brightness of sky and telescope emission, readout process, and the distribution of sources as a function of the flux.

We have constructed a software simulator called the FISVI representing Virtual Instrument of the FIS, that can simulate the data stream of ASTRO-F/FIS. The purposes of the software simulation are to confirm the hardware configurations and to measure the detection limits. The initial design concepts and the detailed algorithms of the FISVI are described in Jeong et al. (2000; 2003). Anomalous behaviours of the detectors are discussed in Jeong et al. (2004). In this paper, we assumed that the sky brightness is constant and only contributes photon noise. The sky confusion noise due to the cirrus structure will be discussed in the following paper.

## 5.2 SOFTWARE STRUCTURE

Figure 1 shows an overview of the simulation software. We first prepare input data for the observing simulations. The input data file provides the coordinates and the properties of the sources, e.g., type of spectral energy distribution (SED), luminosity and redshift, in the virtual sky. We only deal with point sources in this paper because most of the target sources will be distant. The observing simulation procedure makes the images on the focal plane by convolving the point sources and the Point Spread Function (PSF) of the telescope and the instrument. In this convolution, we use the Compiled PSF which includes the information on the transmittance and the spectral response in order to reduce the computation time by an order of magnitude (Jeong et al. 2003). The software generates time series data for each pixel by simulating the scanning procedure of the ASTRO-F/FIS survey mode observations. Using these time series data, we can simulate an image through the image reconstruction routines. We finally count the sources on the reconstructed images to estimate the detection limits.

## 5.3 POINT SOURCE CATALOGUE

In our previous work (Jeong et al. 2003), we did not consider in detail, the SEDs of galaxy sources, their evolution, or the cosmological model for the spatial distribution of the input sources. However, these results showed that the effective detection limits in the long wavelength bands, e.g., WIDE-L band, are governed by source confusion noise. In order to check the detection limits of the ASTRO-F/FIS with realistic extragalactic, cosmological models, we introduce a point source catalogue generated from the models of Pearson and Rowan-Robinson (1996), Pearson (2001) and Rowan-Robinson (2001).

### 5.3.1 Galaxy Evolution Models

Generally, the source count model can be described by the SEDs of galaxies and their luminosity function (see Figure 5.2), if there is no evolution of the galaxies. In this simulation, we incorporate four spectral components: infrared cirrus to represent quiescent

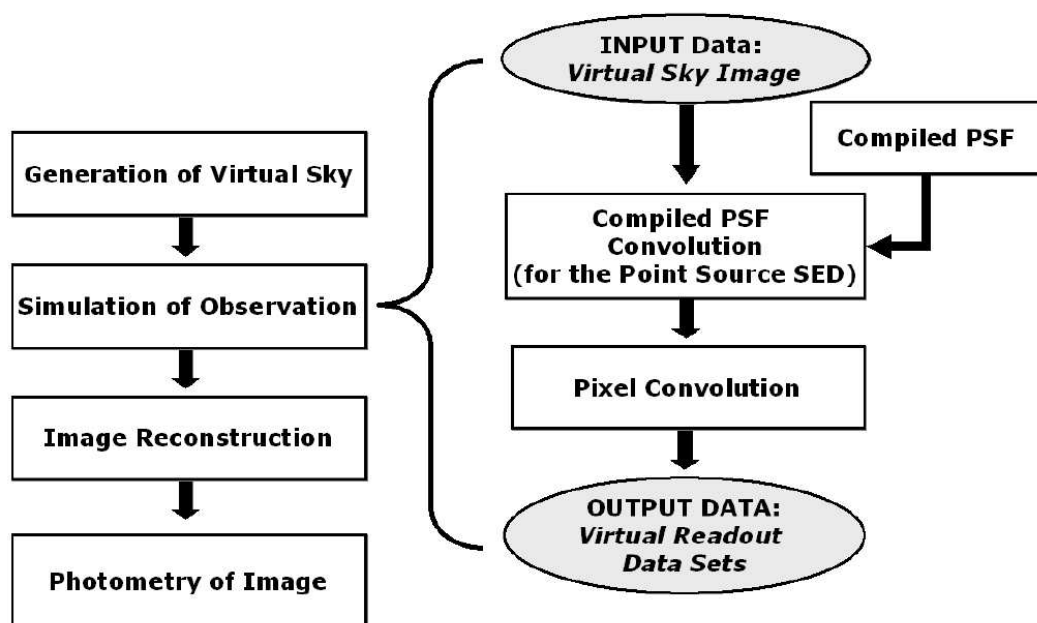


FIG. 5.1: Structure of the simulation software. On the right side, the virtual observation procedures using the Compiled PSF are shown.

normal galaxies, an M82-like starburst, an Arp 220-like high optical depth starburst to represent ultraluminous infrared galaxies, and an active galactic nucleus (AGN) dust torus (Rowan-Robinson 2001). The 60  $\mu\text{m}$  luminosity function is determined by using the IRAS PSCz sample (Saunders et al. 2000).

It has been known that galaxy evolution is a necessary and crucial ingredient in explaining the source counts at infrared wavelengths. Evolution can be in the luminosity or/and in the number density of the source population. The effect of luminosity evolution, assumed to be due to enhanced bulk star formation in galaxies, is to make the luminosity of the galaxies increase with look back time, i.e. galaxies were more luminous in the past. The effect of the density evolution, assumed to be due to merging in the galaxy population, is to increase the number density of galaxies with look back time, i.e. galaxies were more numerous in the past. The luminosity evolution can be represented parametrically as power law functions. We assume the luminosity of a source increases by a factor  $f(z)$  at a redshift  $z$ , i.e.,  $L(z) = L(z = 0)f(z)$ , where  $f(z)$  follows the power law function of redshift  $z$  (Pearson & Rowan-Robinson 1996):  $f(z) = (1 + z)^{3.1}$  for  $0 < z \leq 2$ ,  $f(z) = 2^{3.1}$  for  $2 < z < 10$ , and 0 for  $z \geq 10$ . Similarly, the density evolution also follows the power law (Rowan-Robinson 2001):  $\rho(z) = \rho(0)(1 + z)^n$ , where  $n = 1$ .

### 5.3.2 Source Distribution

For any source at redshift  $z$ , the rest frame source luminosity,  $L_{\nu_o}$ , at frequency,  $\nu_o$ , is spread out over a sphere of surface  $4\pi D_L^2$ , where  $D_L$  is the luminosity distance which is a distance to a source as determined by observing the attenuation of the source's light intensity. The observed flux at the observing frequency  $\nu$  is obtained from:

$$S(\nu) = \frac{(1 + z)L_{\nu_o}}{4\pi D_L^2} = \frac{L_\nu K(L, z)}{4\pi D_L^2}, \quad (5.1)$$

where  $K(L, z)$  is the K-correction that relates the rest frame source spectrum to the observers frame source spectrum. For any given flux limit, we then calculate the limiting luminosity,  $L$  for a source to be observable at a redshift  $z(L, S, \nu)$ . The total

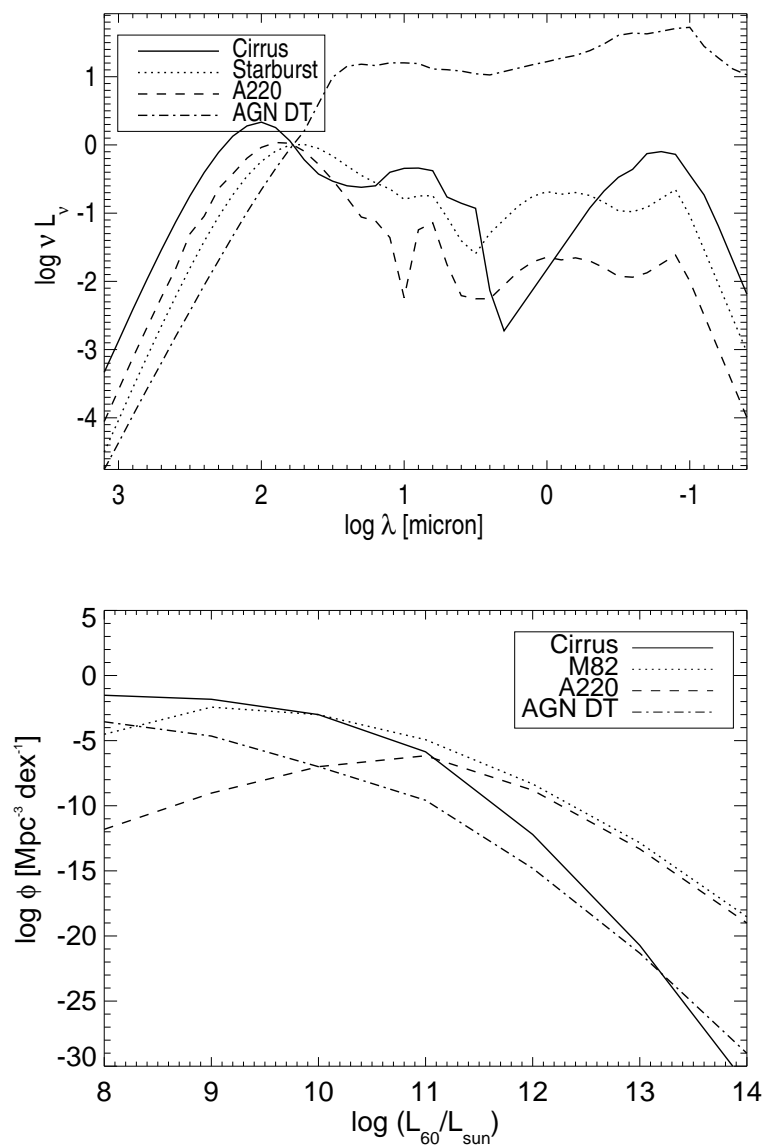


FIG. 5.2: Spectral energy distribution (upper; Rowan-Robinson 2001) and luminosity function (lower; Saunders et al. 2000) at 60  $\mu\text{m}$  for four galaxy types used in this simulation.

number of sources down to a flux limit  $S$  is then calculated by summing over the  $60\mu\text{m}$  luminosity function and cosmological volume element as given by:

$$N_\nu(> S) = \sum_{i=1}^4 \int d \log L \int_0^{z(L,S,\nu)} \phi(L, z) dV, \quad (5.2)$$

where  $\phi$  is the luminosity function and the summation is performed for four types of SED.

## 5.4 GALAXY SOURCE COUNTS RESULTS

We make the input point source catalogue from the source distribution and generate the image for each band. We carried out the aperture photometry on the simulated images using SExtractor software *v2.0.0* (Bertin & Arnouts 1996). The source detection in this simulation mainly depends on the photon and readout noise, and the source confusion noise.

In this work, we assumed three sources of noise: photon noise due to the sky background, photon noise due to the thermal emission from the telescope, and readout noise. We assumed that the photon noise and the readout noise follow Poisson statistics and Gaussian statistics, respectively (see Jeong et al. 2003 for details). In addition, the detection limit is affected by the source confusion: many detected sources contain fainter sources within the beam. In order to compare this with the theoretical source confusion limit, we also calculate the theoretical  $5\sigma$  source confusion noise using the formula in Condon (1974) and Francheschini (1989), and plots that in Figures 5.3 and 5.4.

Figure 5.3 shows a plot of the  $S_{\text{out}}/S_{\text{in}}$  as a function of  $S_{\text{in}}$ , where  $S_{\text{in}}$  and  $S_{\text{out}}$  denote the input flux and the flux obtained by photometry. We find that the output flux  $S_{\text{out}}$  is consistent with the input flux for the SW bands. The theoretical source confusion limit is much lower than the level of the photon and readout noise. But, in the LW bands, the output flux  $S_{\text{out}}$  is systematically overestimated for sources below the theoretical source confusion limits. Such an upward bias is caused by source confusion.

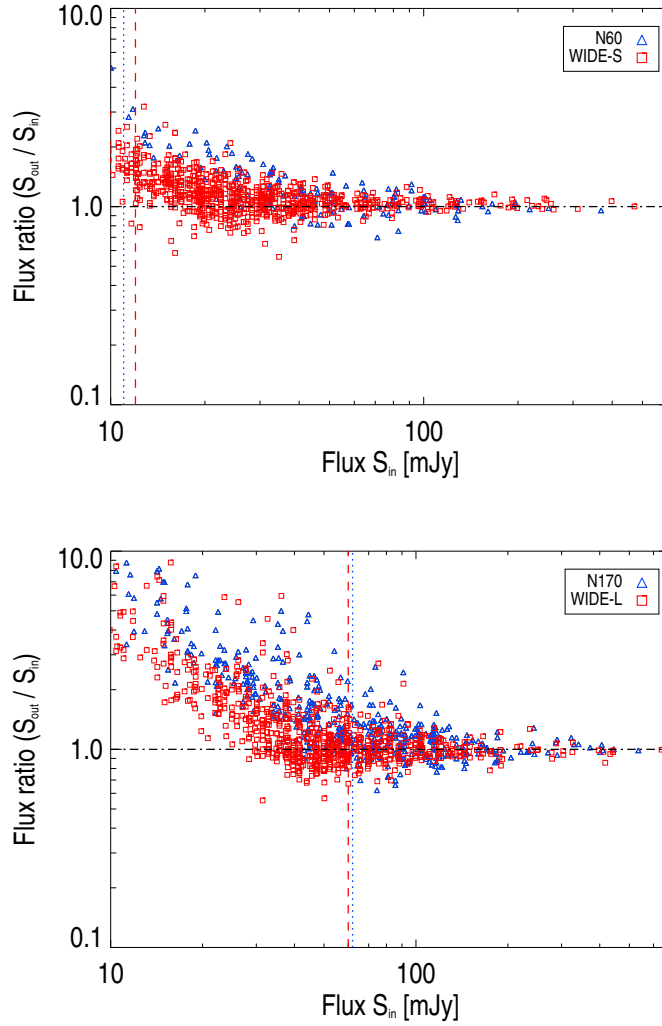


FIG. 5.3: Flux ratio between the input and the output fluxes for extracted and identified sources. The vertical lines represent the theoretical  $5\sigma$  source confusion noise using the formula for the narrow band (dotted line) and the wide band (dashed line). The output flux is well consistent with the input flux in the case of SW bands (upper). But, in LW bands, the output flux is greater than the input flux (lower) due to the source confusion.

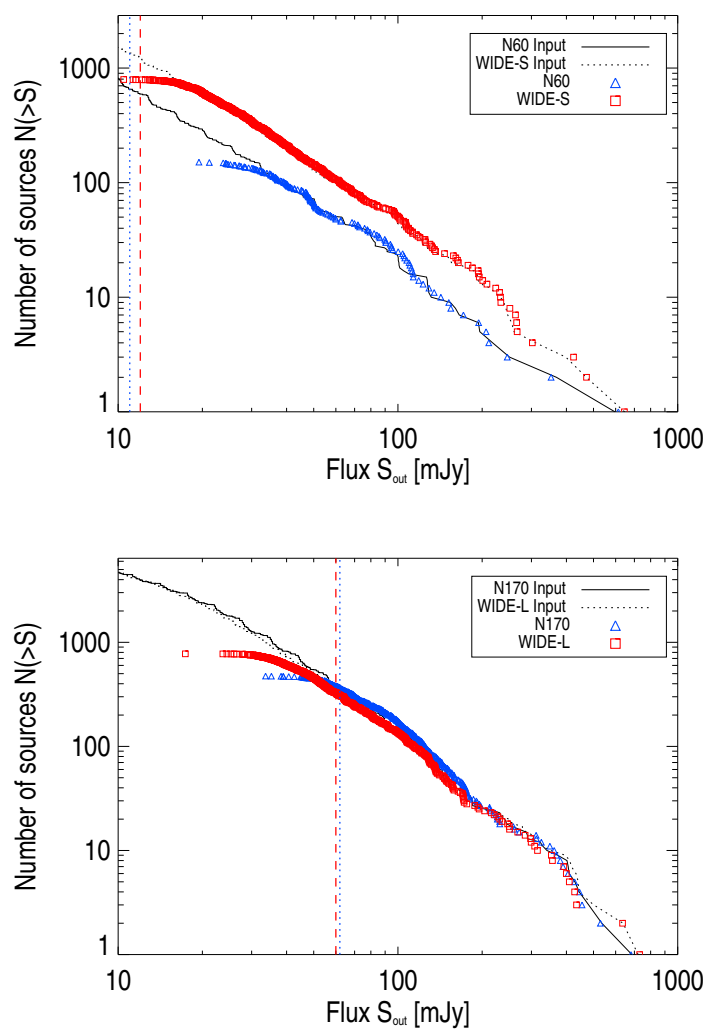


FIG. 5.4: Integrated source count results. The upper panel is for SW bands and the lower panel is for LW bands. The vertical lines mean the theoretical confusion limits.

TABLE 5.1:  $5\sigma$  detection limits

	WIDE-L	N170	WIDE-S	N60
	(mJy)	(mJy)	(mJy)	(mJy)
source confusion limit (Jeong et al. 2003)	23	24	12	11
source confusion limit (Present)	60	62	13	12
detection limit (Jeong et al. 2003)	26	66	21	49
detection limit (Present)	54	78	23	46

These results mean that the source confusion in the SW bands is negligible, but in the LW bands it will affect source detection.

Figure 5.4 shows a plot of integrated source count results. The source distribution in the LW bands has a higher normalization factor due to the strong evolution and the SED of galaxies compared with our previous work (Jeong et al. 2003), which make the source confusion limits higher. The bend at low S is mainly due to the detection limit dominated by the photon and readout noise in the SW bands. Because the theoretical source confusion limit is larger than the bend in LW bands, source confusion becomes important in the LW bands though we can not see a significant flux boosting in the right panel of Figure 5.4. Therefore, the source count result is limited in SW bands by the photon and readout noise and in LW by the source confusion. Table 5.1 shows the  $5\sigma$  detection in our simulation. For comparison, we also list the previous work (Jeong et al. 2003).

## 5.5 DISCUSSION

In order to check the performance of the FIS survey, we have estimated the predicted number-redshift distribution in a cosmological model. We define the detection correctness which is the ratio of the number of correctly detected sources to the number of actually detected sources to calculate the detection limits. This sets a lower limit to

the luminosity of an observable source at redshift  $z$ . The number-redshift distribution at flux  $S$ , can be obtained from the integration of the evolving luminosity function and is given by:

$$\frac{dN_\nu(S, z)}{dz} = \int d \log L \int_0^{z(L, S, \nu)} \phi(L, z) \frac{dV}{dz} \quad (5.3)$$

Source detection is mainly limited by photon and readout noise in the SW bands. Since the source confusion severely affects source detection in the LW bands due to the crowded beams, its limiting magnitude is not so different from that of the SW bands (see Figure 5.5). The limiting redshift is  $\sim 2.5$  in SW bands and  $\sim 3$  in LW bands. Also, we can see that the number of sources with high redshift in the LW bands is larger than that in the SW bands. This is due to the positive effects of the large K-corrections induced as the LW bands climb the Rayleigh-Jeans slope towards the dust peak around  $100 - 60 \mu\text{m}$  in the source SEDs.

---

W.-S. Jeong was financially supported by the BK21 Project of the Korean Government. This work was financially supported in part by the KOSEF-JSPS corporative program. The ASTRO-F project is managed and operated by the Institute of Space and Astronautical Science (ISAS), Japan in collaboration with groups in universities and institutes in Japan as well as with Seoul National University, Korea.

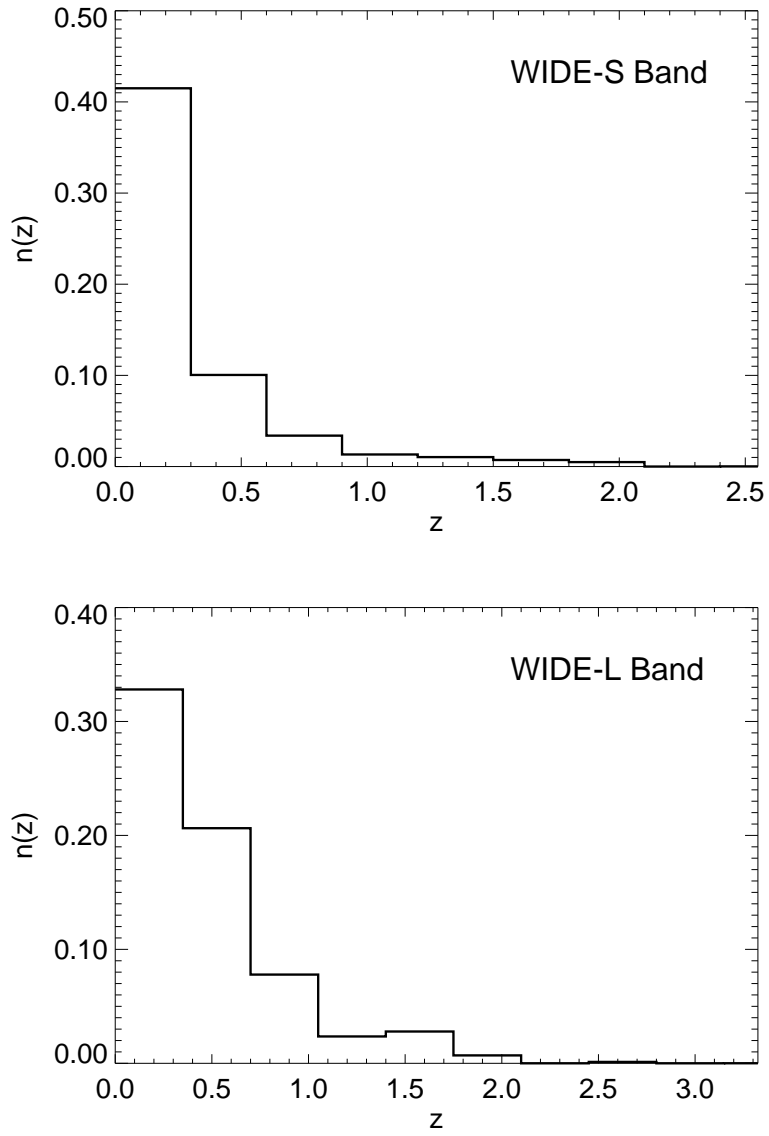


FIG. 5.5: Predicted redshift distribution for Wide-S and Wide-L bands.

## REFERENCES

- Bertin, E., & S. Arnouts, 1996, *A&AS*, 117, 393
- Condon, J.J., 1974, *AJ*, 188, 279
- Franceschini, A., L. Toffolatti, and L. Danese, 1989, *ApJ*, 344, 35
- Jeong W.-S., S. Pak, H. M. Lee, et al., 2000, in *Proc. of Mid- and Far-Infrared Astronomy and Future Missions*, eds. T. Matsumoto & H. Shibai, ISAS Report SP14, 297
- Jeong W.-S., S. Pak, H. M. Lee, T. Nakagawa, J. Sohn, I. Ahn, I. Yamamura, M. Watanabe, M. Kawada, & H. Shibai, 2003, *PASJ*, 55, 717
- Jeong W.-S., S. Pak, H. M. Lee, et al., 2004, *Adv. Space Res.*, in press
- Kawada M., 1998, *Proc. of SPIE*, 3354, 905
- Kawada, M., 2000, in *Proc. of Mid- and Far-Infrared Astronomy and Future Missions*, eds. T. Matsumoto & H. Shibai, ISAS Report SP14, 273
- Murakami, H., 1998, *Proc. of SPIE*, 3356, 471
- Nakagawa, T., 2001, in *Proc. of The Promise of the Herschel Space Observatory*, eds. G.L. Pilbratt, J. Cernicharo, A.M. Heras, T. Prusti, & R. Harris, ESA-SP 460, 67
- Pearson, C. P., & M. Rowan-Robinson, 1996, *MNRAS*, 283, 174
- Pearson, C. P., 2001, *MNRAS*, 325, 1511
- Rowan-Robinson, M., 2001, *ApJ*, 549, 745

Saunders, W. et al. 2000, MNRAS, 317, 55

Shibai, H., 2001, in The Extragalactic Background and Its Cosmological Implications,  
eds. M. Harwit & M. G. Hauser, IAU Symp. No. 204, 455

# Chapter 6

## Sky Confusion Due to Galactic Cirrus<sup>b</sup>

### Abstract

Fluctuations in the observed brightness of the background radiation can lead to confusion with real point sources. Such background emission confusion will be important for infrared observations with relatively large beam sizes since the degree of fluctuation tends to decrease with angular scale. In order to quantitatively assess the effect of this background emission on the detection of point sources for current and future far-infrared observations by space-borne missions such as Spitzer, ASTRO-F, Herschel and SPICA, we have extended the Galactic emission map to higher resolution than the currently accessible scale. Using this high resolution map, we estimate the sky confusion noise due to the emission from interstellar dust clouds or cirrus, based on fluctuation analysis as well as carrying out photometry over realistically simulated images. We find that the confusion noise derived by this fluctuation analysis agrees well with the result from realistic simulations, when we take the parameter in the fluctuation analysis related to background estimation parameter in the photometry to be the same value. Though the confusion noise becomes dominant in long wavelength bands

---

<sup>b</sup>W.-S. Jeong, S. Pak, H. M. Lee, T. Nakagawa, S. M. Kwon, C. P. Pearson, & G. J. White, 2004, submitted to MNRAS

(> 100  $\mu\text{m}$ ) for each space mission, the confusion due to cirrus structure is expected to be much less significant for the next generation of the space missions with larger aperture sizes (e.g. Herschel and SPICA) than the estimate from the observation data.

## 6.1 INTRODUCTION

Galactic emission in the far-infrared (IR) sky affects the detection of faint IR sources in maps. The amount of emission manifests itself as photon noise whose fluctuations follow Poisson statistics. In addition, any brightness fluctuation at scales below the beam size could cause confusion with real point sources. Emission from irregular clouds of interstellar dust on all spatial scales commonly referred to as *infrared cirrus*, was discovered by the Infrared Astronomy Satellite (IRAS) Low et al. 1984. Cirrus emission peaks at far-IR wavelengths but was detected in all 4 IRAS bands 12, 25, 60, and 100  $\mu\text{m}$  (Helou & Beichman 1990, hereafter HB90). The Galactic cirrus depends upon the Galactic latitude and is significant for wavelengths longer than 60  $\mu\text{m}$ . This Galactic cirrus, which is the main source of background radiation in far-IR, causes an uncertainty in the determination of source fluxes by varying the sky brightness. The accurate determination of observational detection limits requires a knowledge of the Galactic emission as a function of position on the sky. The other important factor affecting the source detection is the source confusion which mainly depends upon the telescope beam size and the source distribution itself. The effects resulting from a combination of the sky confusion and the source confusion will be discussed in depth in the forthcoming paper [Jeong et al. 2004c (Paper II), in preparation].

There have been realistic estimations of the sky confusion from observation data such as IRAS and the Infrared Space Observatory (ISO) (Gautier et al. 1992; Helou & Beichman 1990; Herbstmeier et al. 1998; Kiss et al. 2001). However, the resolution of the data in their studies is not still sufficient to the application to missions planned in future since the resolutions of future missions will reach to the values of smaller than 1 arcmin. Many valuable data in the far-IR wavelength range will be available within or around this decade by a multitude of IR space projects such as Spitzer (formerly

known as SIRTf, the Space Infrared Telescope Facility) Gallagher et al. 2003, ASTRO-F (Murakami 1998; Shibai 2000; Nakagawa 2001; Pearson et al. 2004), Herschel Space Observatory (HSO) (Pilbratt 2003) and the Space Infrared Telescope for Cosmology and Astrophysics (SPICA) (Nakagawa 2004). Since these instruments will observe the sky to high sensitivities, it is required to understand the factors determining their detection limits. Based on the measured power spectrum and the spectral models of the dust emission over the entire sky, we extrapolate this power spectrum in order to include the small-scale fluctuations and generate the dust map with higher spatial resolution in various relevant wavelength bands ( $< 10$  arcsec).

This paper is organized as follows. In section 6.2, we briefly describes the sky confusion noise due to sky brightness fluctuations and in section 6.3, the process for the realization of Galactic dust emission at high angular resolution in various IR bands. Based upon the specifications of each IR mission, we estimate the sky confusion noise through statistical analysis in section 6.4. We present in section 6.5 a comparison of estimated detection limits based on statistical noise analysis with the results based on the photometry from realistically simulated images. In section 6.6, we discuss the effect of the instrumental noise and our conclusions are summarised in section 6.7.

## 6.2 CONFUSION DUE TO SKY FLUCTUATION

Measuring the brightness of sources involves subtracting the sky background derived from the well-defined reference. The fluctuations in the surface brightness of extended structure on similar scales to the resolution of the telescope/instrument beam can produce spurious events that can be easily mistaken for genuine point sources. This is because the source detection is usually simply accomplished from the difference in signal between the on-source position and some background position. The sky confusion noise due to the sky brightness fluctuations,  $N(\theta)$ , is defined as:

$$N(\theta) = \Omega \sqrt{S(\theta)}, \quad (6.1)$$

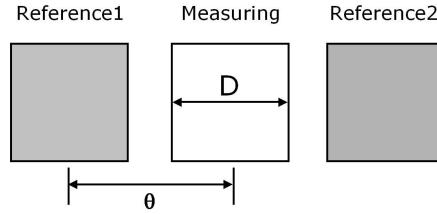


FIG. 6.1: Schematic outline of the reference aperture configurations for two symmetrically placed circular apertures (left) and reference annulus (right) (Gautier et al. 1992).

where  $\Omega$  is the solid angle of the measuring aperture,  $\theta$  is the angular separation between the target and reference sky positions, and  $S(\theta)$  is the second order structure function. Gautier et al. (1992) calculated the sky confusion noise due to the structure of the Galactic cirrus, using the second order structure function for a far-IR surface brightness distribution:

$$S(\theta) = \left\langle \left| I(x) - \frac{I(x - \theta) + I(x + \theta)}{2} \right|^2 \right\rangle_x, \quad (6.2)$$

where  $I$  is the sky brightness,  $x$  is the location of the target, and  $\langle \rangle$  represents the average which is taken in spatial coordinates over the whole map. For the configuration of two symmetrically placed reference apertures, see the figure 6.1.

Though the zodiacal emission is main background source in the short wavelength of far-IR range, it will not contribute to the fluctuations on the large scales because the zodiacal light is smooth on large scales of its brightness distribution (Reach et al. 1995; Kelsall et al. 1998). From the analysis of the ISO data, Ábrahám et al. (1997) searched for the brightness fluctuations in the zodiacal light at  $25 \mu\text{m}$  with 5 fields of  $\sim 0.5^\circ \times 0.5^\circ$  at low, intermediate, and high ecliptic latitudes. They found that an upper limit to the fluctuations of 0.2% of the total brightness level was estimated for an aperture of  $3'$  diameter. This amount of fluctuations supported the model for a smooth zodiacal light distribution.

Therefore, the sky confusion noise is mainly related to the spatial properties of the cirrus. In many cases, the power spectrum of the dust emission can be expressed as a simple power-law. Using the IRAS data at 100  $\mu\text{m}$ , Gautier et al. (1992) computed the power spectrum  $P$  of the spatial fluctuations of cirrus emission as a function of spatial frequency  $k$ , for angles between 4' and 400'.

$$P = P_0 \left( \frac{k}{k_0} \right)^\alpha = P_0 \left( \frac{d_0}{d} \right)^\alpha, \quad (6.3)$$

where  $P_0$  is the power at the spatial frequency  $k_0$ ,  $d_0$  is the corresponding scale length,  $d$  is the scale length corresponding to the width of the measurement aperture, and  $\alpha$  is the index of the power spectrum.  $P_0$  scales roughly as cube of the average surface brightness  $B_0$  of the cirrus cloud. Integrating equation 6.2 numerically, the sky confusion noise  $N$  scales as:

$$N \propto \left( \frac{d}{d_0} \right)^{\frac{1-\alpha}{2}} \cdot P_0^{\frac{1}{2}}. \quad (6.4)$$

Helou & Beichman (1990) extended the work of 100  $\mu\text{m}$  by Gautier et al. (1992) in order to estimate the sky confusion at all wavelengths, using the empirical relationship,  $P_0 \propto \langle B_0 \rangle^3$  and  $\alpha = -3$  in Gautier et al. (1992). They found an approximation for the cirrus confusion noise as follows:

$$\frac{N_{\text{HB90}}}{1 \text{ mJy}} = \zeta \cdot \left( \frac{\lambda}{100 \mu\text{m}} \right)^{2.5} \left( \frac{D_t}{1 \text{ m}} \right)^{-2.5} \left( \frac{\langle B_\lambda \rangle}{1 \text{ MJy sr}^{-1}} \right)^{1.5}, \quad (6.5)$$

where  $\zeta$  is the normalization constant,  $\lambda$  the wavelength of the measurement,  $D_t$  the diameter of the telescope, and  $\langle B_\lambda \rangle$  is the mean brightness at the observation wavelength. They set the constant  $\zeta$  to be 0.3.

This indicates that the sky confusion depends upon both the variation of the surface brightness in the background structure and the resolution of the telescope. Consequently, the noise becomes less significant for larger aperture sizes such that the next generation of space telescopes (e.g., Herschel and SPICA) should not be severely affected by sky confusion over most of the sky.

## 6.3 GENERATION OF CIRRUS MAP

In order to investigate the sky confusion for the present and upcoming infrared space missions with a high resolution. We obtain cirrus emission map by adding the artificially generated high resolution component to the observation data with the low resolution. For the observation data, we used the all-sky 100  $\mu\text{m}$  dust map generated from the IRAS data by Schlegel, Finkbeiner, and Davis (1998; hereafter SFD98). Here, we describe our simulation models for cirrus map and discuss it.

### 6.3.1 Fluctuations at Higher Spatial Resolution

#### Measured Power Spectrum

Figure 6.2 shows the power spectrum measured in the dust maps of SFD98 at a Galactic latitude of  $b = |50|$  degrees. These power spectra are well fitted with power laws of index -2.9. However, the power drops above the frequency corresponding to the map resolution of  $\sim 6.1$  arcmin (see figure 6.2). Though the structure of the dust emission over the entire sky position can be derived from a dust map, e.g., SFD98, we need to generate the dust map including the contributions from small-scale fluctuations in order to study for the planned present and future missions with high resolution ( $< 1$  arcmin). We obtain this high resolution map by adding small-scale structure of cirrus emission to the low-resolution map of SFD98 assuming that the small-scale fluctuations also follow the estimated power spectrum with the same power-law index, as described above.

#### Simulation of Fluctuations Due to Dust Emission

In order to add the small-scale fluctuations, we simulate fluctuations due to the cirrus emission through the Fourier analysis of density fluctuations. The power,  $P(k)$ , is defined as the variance of the amplitude in the fluctuations:

$$P(k) \equiv \langle |\delta_k|^2 \rangle = \frac{1}{V} \int \xi(x) \frac{\sin(kx)}{kx} 4\pi x^2 dx, \quad (6.6)$$

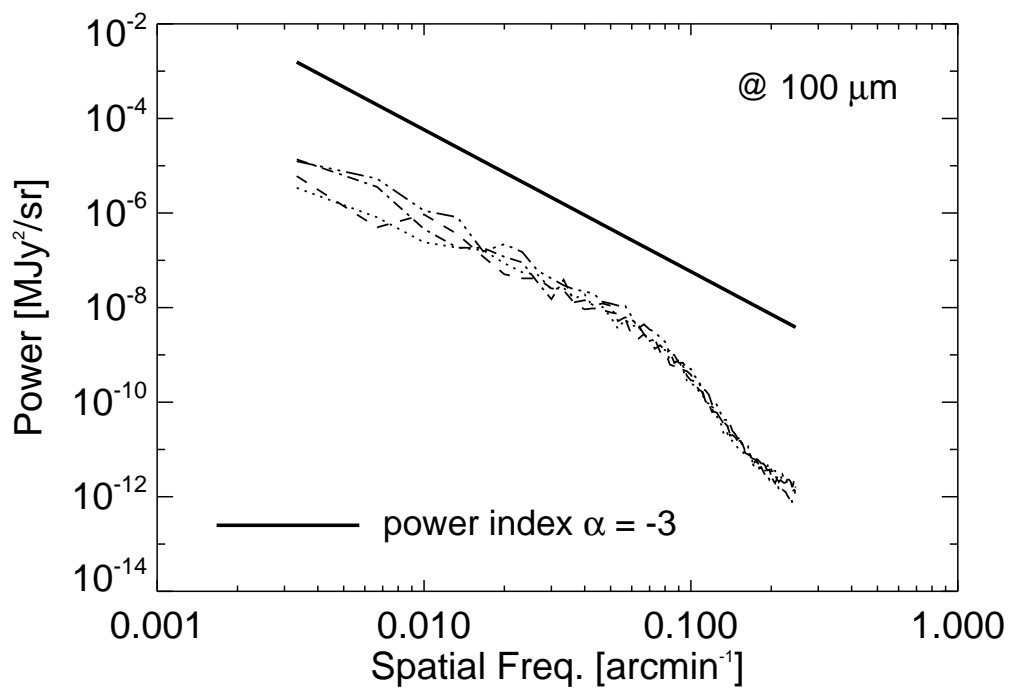


FIG. 6.2: Measured power spectrum of dust emission in the dust map by SFD98 (Schlegel, Finkbeiner & Davis 1998). The four curves represent four patches selected in the Northern and the Southern Galactic sky at  $b = |50|^\circ$ .

where  $k$  is the spatial frequency,  $\delta_k$  is the perturbation field,  $\langle |\delta_k|^2 \rangle$  is the variance of the fluctuation and  $\xi(x)$  is the correlation function of the density field. We assume that the distribution of fluctuations is approximated as a random Gaussian process where the Fourier components  $\delta_k$  have random phases so that the statistical properties of distribution are fully described by the power spectrum  $|\delta_k|^2$  (Peebles 1980). In this case, we can set each fluctuation within a finite grid in the frequency domain by a random Gaussian process of the amplitude of each fluctuation considering the realization of a volume for the sample embedded within a larger finite volume (Gott & Park 1990; Park et al. 1994; Peacock 1999). We assign Fourier amplitudes randomly within the above distribution in the finite volume and assign phases randomly between 0 and  $2\pi$ . Since the field used in this simulation is small ( $< 10$  degree), we can take the small-angle approximation and treat the patch of sky as flat (White et al. 1999). In the flat sky approximation, we obtain the power spectrum and generate a patch of the dust map in cartesian coordinates.

We generate a realistic distribution of the Galactic emission in the following manner. The basic data for the information of the large-scale structure are obtained from the low resolution all-sky map by SFD98. We add the simulated small-scale structure to these basic data in the Fourier domain, where the power spectrum of the small-scale structure follows that of the large-scale structure. Figure 6.3 shows our simulated emission map including small-scale fluctuations. The left panel of figure 6.3 shows the simulated dust emission image corresponding to a power spectrum with  $\alpha = -3$ . The middle panel includes only the emission below the resolution of the dust map by SFD98,  $\sim 6.1$  arcmin, (large-scale emission) while the right panel shows the emission above the resolution of the dust map by SFD98 (separated in Fourier domain, i.e., small-scale emission). The lower panel shows the profiles for selected areas of two images (upper-left and upper-middle panels). We find in this simulation that the emission including the high resolution, small-scale component (above the resolution of the dust map by SFD98 to a resolution of 4 arcsec) reflects the trend of the large-scale emission (below the resolution of SFD98 dust map). In addition, the contribution from the small-scale fluctuation becomes  $\sim 15\%$  of the mean sky brightness.

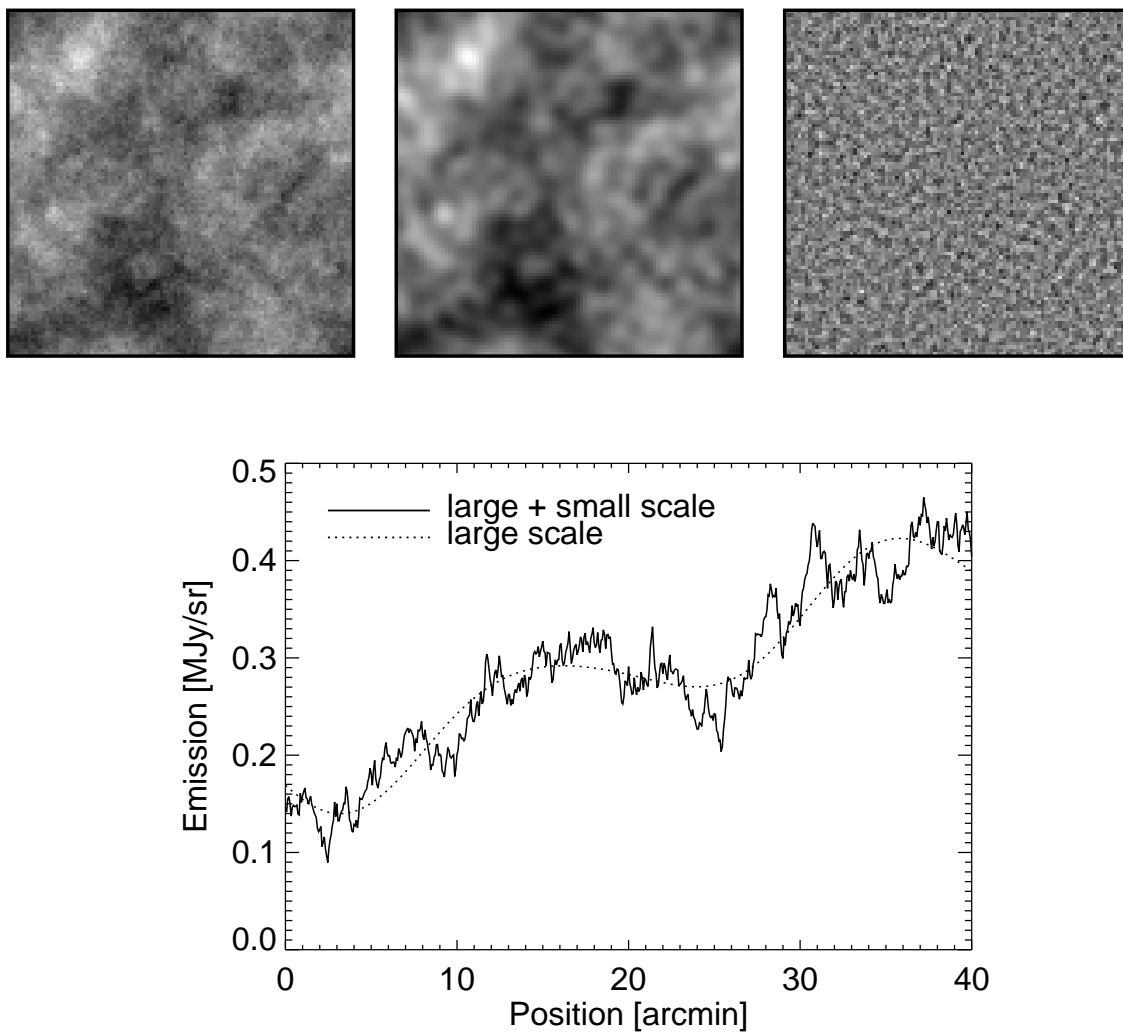


FIG. 6.3: Simulated dust emission map (upper) and the profile of map (lower). The upper-left panel shows the simulated image assuming a power spectrum with a power index of -3. The upper-middle panel and the upper-right panel show only large-scale fluctuations and small-scale fluctuations, respectively. The lower panel shows the one-dimensional profile for a selected part of the upper-left and the upper-middle panel.

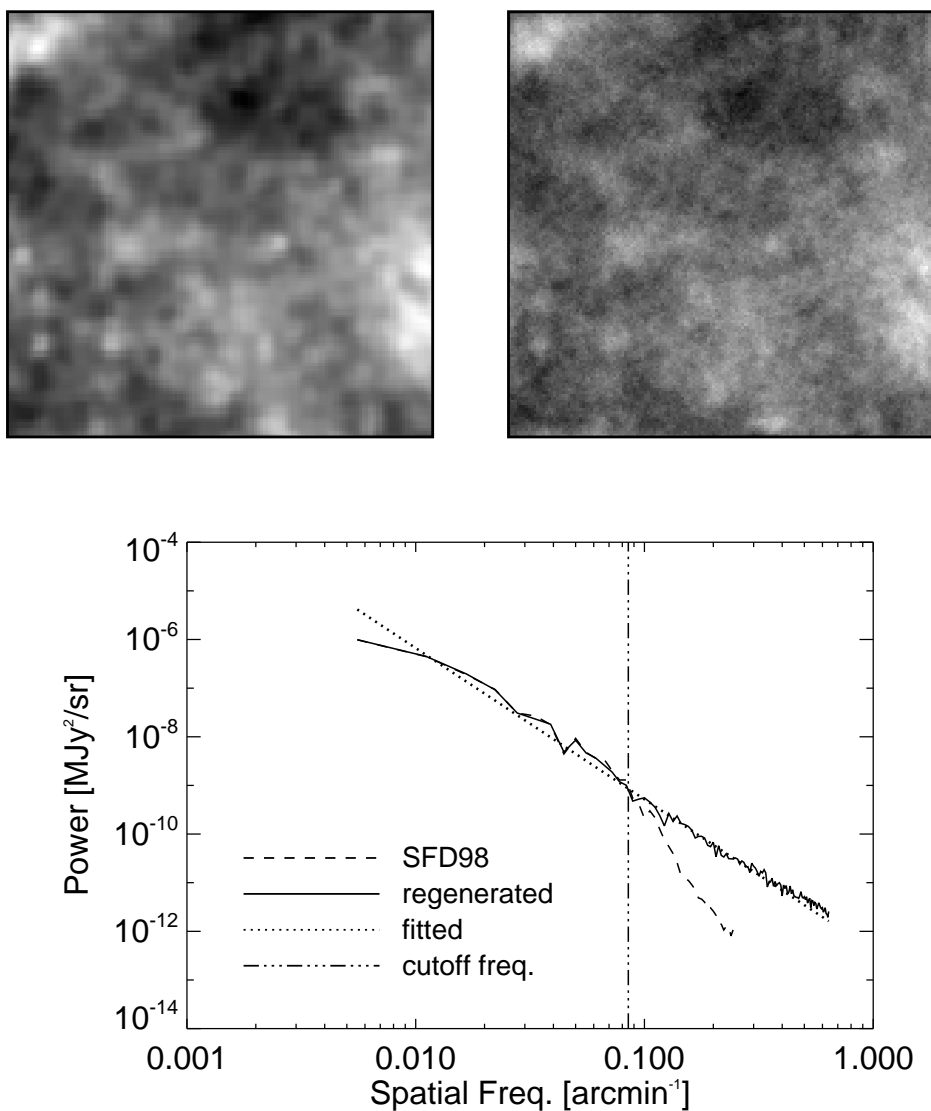


FIG. 6.4: Patch of SFD98 dust map, regenerated patch (upper panel) and the estimated power spectrum (lower panel). The upper-left panel is a patch of the SFD98 dust map at the Galactic latitude of 50 degree and the upper-right panel is the regenerated patch based upon the patch from the SFD98 dust map. The dashed and solid lines in the lower panel show the estimated power spectrum of the upper-left and the upper-right panels, respectively. Note that the Nyquist frequency in the power spectrum of the upper-right panel is  $7.5 \text{ arcmin}^{-1}$ , but we only plot to  $\sim 0.5 \text{ arcmin}^{-1}$ . The dotted line shows the fit to the power spectrum below the spatial cutoff frequency.

We obtain a patch of the dust map including small-scale fluctuations by summing the large-scale component of SFD98 dust map and the small-scale component of the simulated emission in the Fourier domain. According to this scheme of Fourier power spectrum analysis, the cutoff spatial frequency of the dust map by SFD98 is set to the Nyquist limit, i.e. a half of the spatial frequency corresponding to the resolution of the dust map by SFD98. We use the power spectrum fitted below the Nyquist sampling limit in order to extend the power spectrum to higher spatial frequencies. Typically, the 2D power spectrum of a SFD98 dust map patch shows the presence of a cross along spatial frequencies of  $x$  and  $y$  axis if we assume that the center in the spatial domain is regarded as the spatial frequency 0. This cross is caused by the Fast Fourier Transform (FFT) algorithm that makes an “infinite pavement” with the image prior to computing the Fourier transform (Miville-Deschênes et al. 2002). In order to preserve the information of the emission at the edges, we directly use the power at the spatial frequencies of  $x$  and  $y$  axis, and extrapolate the power at other spatial frequencies (above the cutoff spatial frequency) according to the estimated power spectrum. In figure 6.4, we show a patch of the dust map by SFD98 at a Galactic latitude of 50 degree, a patch regenerated by extending the power spectrum of the patch by SFD98 and the estimated power spectrum.

### 6.3.2 Dust Emission at Other Wavelengths

Assuming that the spatial structure of the dust emission is independent of wavelength, we can obtain the dust map at other wavelengths than  $100 \mu\text{m}$  by applying an appropriate model for the Spectral Energy Distribution (SED). Since the dust particles are small ( $< 0.25 \mu\text{m}$ ) compared with far-IR wavelengths, the opacity does not depend upon the details of the particle size distribution, but on the nature of the emitting material itself. In the far-IR, the opacity  $\kappa_\nu$  generally follows a power law:

$$\kappa_\nu \propto \nu^\beta \tag{6.7}$$

with frequency  $\nu$ .

The SED may be approximated as one-component or two-component models (Schlegel, Finkbeiner & Davis 1998; Finkbeiner et al. 1999). The dust temperature map is constructed from the COBE Diffuse Infrared Background Experiment (DIRBE) 100  $\mu\text{m}$  and 240  $\mu\text{m}$  data (Boggess et al. 1992) which was designed to search for the cosmic IR background radiation. The emission  $I_\nu$  at frequency  $\nu$  can be expressed as

$$I_\nu = K_{100}^{-1}(\beta, T) I_{100} \frac{\nu^\beta B_\nu(T)}{\nu_0^\beta B_{\nu_0}(T)}, \quad (6.8)$$

where  $B_\nu(T)$  is the Planck function at temperature  $T$ ,  $I_{100}$  is the DIRBE-calibrated 100  $\mu\text{m}$  map,  $K_{100}^{-1}(\beta, T)$  is the color correction factor for the DIRBE 100  $\mu\text{m}$  filter when observing a  $\nu^\beta B_\nu(T)$  spectrum (DIRBE Explanatory Supplement 1995). Though the generated temperature maps have relatively low resolution ( $1.3^\circ$ ) compared with our simulated dust map patch, we interpolate this map to small grid sizes ( $< 10$  arcsec), since we do not expect any significant variation of temperature over the smaller scale than the resolution of the map. Taking the emissivity model with  $\beta = 2$  (Draine & Lee 1984) for considering the dominant component of the dust grain, we obtain the dust temperature from the DIRBE 100  $\mu\text{m}/240 \mu\text{m}$  emission ratio (one-component model).

Based upon laboratory measurements, a multicomponent model for interstellar dust has been constructed by Pollack et al. (1994). In order to solve the inconsistency of the  $\nu^2$  emissivity model in the 100 – 2100 GHz (3000 – 143  $\mu\text{m}$ ) emission, Finkbeiner et al. (1999) used a two-component model where diverse grain species dominate the emission at different frequencies in order to fit the data of the COBE Far Infrared Absolute Spectrophotometer (FIRAS). Assuming that each component of the dust has a power-law emissivity over the FIRAS range, Finkbeiner et al. (1999) constructed the emission  $I_\nu$  in multicomponent model:

$$I_\nu = \frac{\sum_i f_i Q_i(\nu) B_\nu(T_i)}{\sum_i f_i Q_i(\nu_0) B_{\nu_0}(T_i) K_{100}(\beta_i, T_i)} I_{100}, \quad (6.9)$$

where  $f_i$  is a normalization factor for the  $i$ -th grain component,  $T_i$  is the temperature of component  $i$ ,  $K_{100}$  is the DIRBE color-correction factor and  $I_{100}$  is the SFD98 100  $\mu\text{m}$  flux in the DIRBE filter. The emission efficiency  $Q_i(\nu)$  is the ratio of the emission cross section to the geometrical cross section of the grain component  $i$ . A two-component

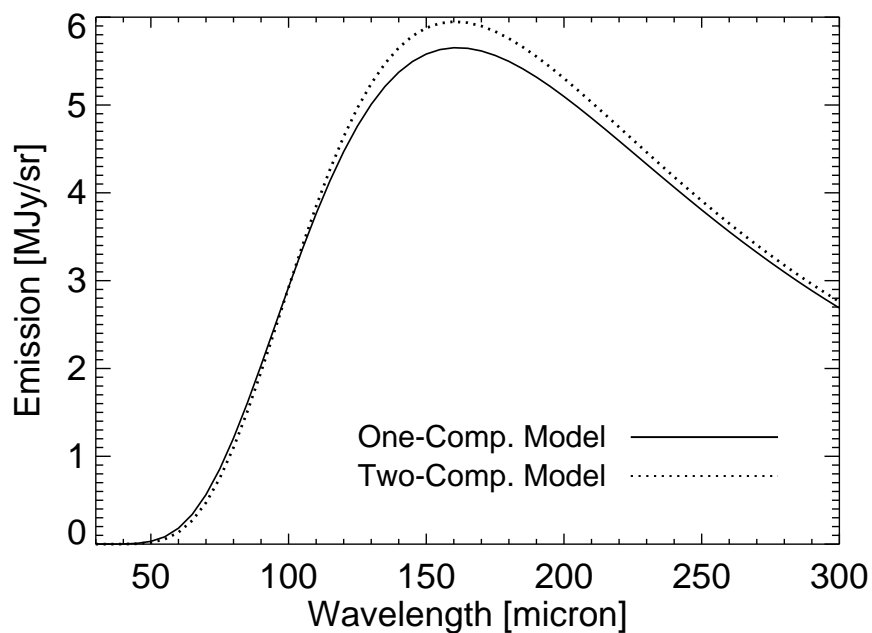


FIG. 6.5: Comparison between the one-component dust model and the two-component dust model for one small patch. The dust emission of the two-component model in the wavelength range from  $120 \mu\text{m}$  to  $200 \mu\text{m}$  is slightly higher than that of the one-component model due to the dominant contribution by carbon grains.

model with a mixture of silicate and carbon-dominated grains provides a fit to an accuracy of  $\sim 15\%$  to all the FIRAS data over the entire high-latitude sky. In figure 6.5, we see the dust emission for the one-component and two-component dust models [see Schlegel et al. (1998); Finkbeiner et al. (1999)]. The two-component model agrees well with the FIRAS data in the wavelength range longer than  $100\ \mu\text{m}$  where the dust emission estimated from one-component model is significantly lower than the estimate from the two-component model.

In two models are not considered the contribution of the small grains resulting in an excess below  $100\ \mu\text{m}$ . However, because we do not have any significant difference between two models or an accurate dust model below  $100\ \mu\text{m}$ , for our purpose, we only use the two-component model in our wavelength range. Through a Point Spread Function (PSF) convolution at each wavelength and a wavelength integration over a  $5\ \mu\text{m}$  wavelength grid, we obtain the high resolution dust map in other bands.

## 6.4 STATISTICAL ANALYSIS FOR SKY CONFUSION NOISE

Among the parameters affecting the sky confusion noise, most of them depend upon the mean brightness, the spatial structure of the cirrus, and the observing wavelength, as seen in equation 6.5. In Table 6.1, we list the basic instrumental parameters of present and future IR space missions; the aperture of the telescope, Full Width at Half Maximum (FWHM) of the beam profile and the pixel size for each detector. For comparison with previous studies (Herbstmeier et al. 1998; Kiss et al. 2001), we include the specifications for ISO. We select a short wavelength band (SW) and a long wavelength band (LW) for each mission.

In order to examine the dependency of the sky confusion noise on the instrumental parameters, we list a normalization constant  $\zeta$  for each mission considered in this work in Table 6.2. As the aperture of the telescope becomes the larger or the wavelength becomes shorter,  $\zeta$  should become correspondingly smaller. For example, if we nor-

TABLE 6.1: Instrumental parameters for various space missions.

Space Mission	Aperture	Wavelength		FWHM <sup>a</sup>		Pixel size	
	(meter)	( $\mu\text{m}$ )		(arcsec)		(arcsec)	
		SW	LW	SW	LW	SW	LW
ISO <sup>b</sup>	0.6	90	170	31.8	60	46	92
Spitzer <sup>c</sup>	0.85	70	160	16.7	35.2	9.84	16
ASTRO-F <sup>d</sup>	0.67	75	140	23	44	26.8	44.2
Herschel <sup>e</sup>	3.5	70	160	4.3	9.7	3.2	6.4
SPICA	3.5	70	160	4.3	9.7	1.8	3.6

<sup>a</sup> FWHM of diffraction pattern.

<sup>b</sup> Two ISOPHOT filters (C1\_90 in SW band and C2\_170 in LW band).

<sup>c</sup> MIPS bands for the Spitzer mission.

<sup>d</sup> ASTRO-F/FIS (Far Infrared Surveyor) has a WIDE-S band in SW and WIDE-L band in LW.

<sup>e</sup> PACS have ‘blue’ array in short wavelength (60-85 $\mu\text{m}$  or 85-130 $\mu\text{m}$ ) and the ‘red’ array in long wavelength (130-210 $\mu\text{m}$ ).

TABLE 6.2: Normalization constant  $\zeta$  of HB90 formula for each space mission. The instrumental parameters for each mission are given in Table 6.1. The mean brightness here is fixed to be  $1 \text{ MJy sr}^{-1}$ .

Space Mission	$\zeta$	
	SW	LW
ISO	0.83	4.05
Spitzer	0.18	1.46
ASTRO-F	0.40	1.89
Herschel	0.0054	0.042
SPICA	0.0054	0.042

malize equation 6.5 with the short wavelength parameter and telescope aperture of ISO mission, i.e.  $90 \mu\text{m}$  and  $0.6 \text{ m}$ , respectively,  $\zeta$  will be  $0.83$  instead of  $0.3$  obtained by Helou & Beichman (1990). In section 6.3, we obtained the dust maps simulated to high spatial resolution over a wide spectral range. With this simulated dust map, we estimate the sky confusion noise for various space mission projects.

### 6.4.1 Selected Regions

We generate the PSF-convolved patches of a dust map as a function of increasing Galactic latitude (decreasing sky brightness) from  $0.3 \text{ MJy sr}^{-1}$  to  $25 \text{ MJy sr}^{-1}$  at  $100 \mu\text{m}$  at a resolution of  $1 \text{ arcsec}$  by using the method explained in section 6.3. The size of the simulated image is  $1.3^\circ \times 1.3^\circ$ . For the PSF, we used an ideal circular aperture Airy pattern corresponding to the aperture size of telescopes. In figure 6.6, we can see the PSF-convolved small patch of dust map ( $900'' \times 900''$ ) for each space mission. The larger the aperture of the telescope becomes, the smaller structures that become visible. Since the cirrus emission generally depends upon the Galactic latitude, we select the patches as a function of the Galactic latitude. We list the properties of

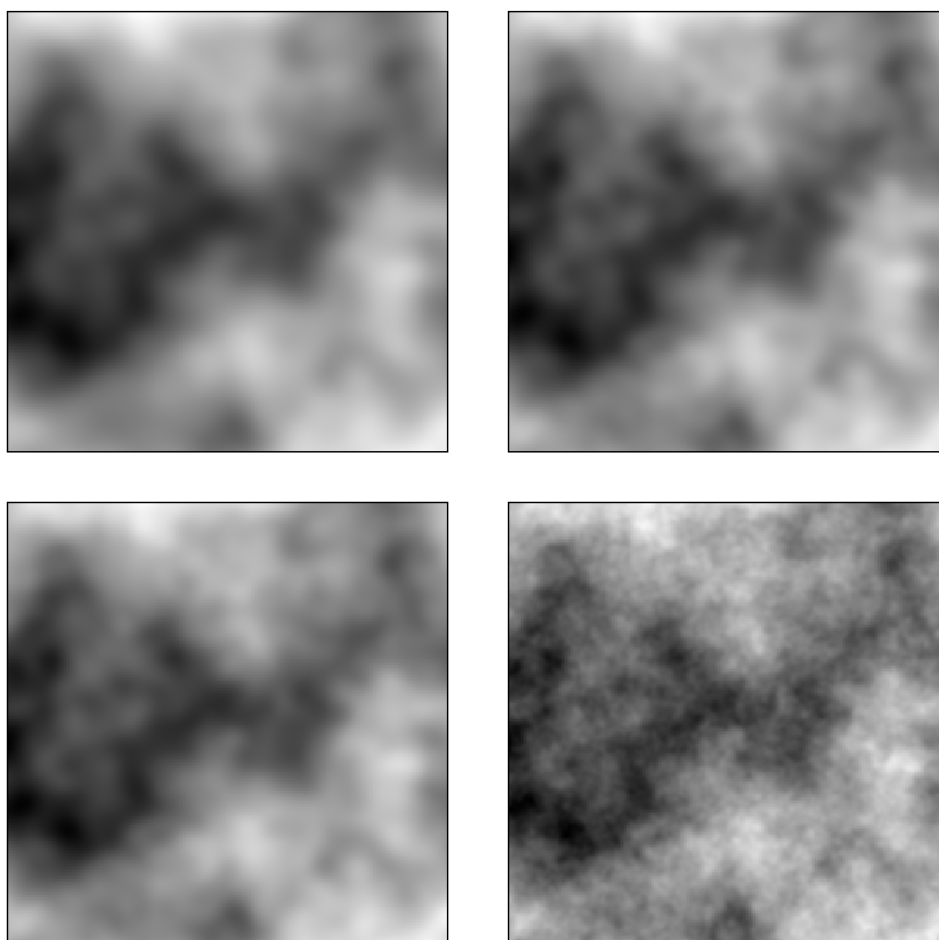


FIG. 6.6: PSF-convolved patch of the dust map for space mission; ISO (upper-left), ASTRO-F (upper-right), Spitzer (lower-left), Herschel/SPICA (lower-right) missions.

TABLE 6.3: Properties of the selected regions. The Galactic longitude of all patches is  $0^\circ$ .  $B_0$  is a mean sky brightness,  $\alpha$  is the power index of the power spectrum, and  $P_0$  is the power estimated at  $0.01 \text{ arcmin}^{-1}$  and  $100 \mu\text{m}$ .

Region <sup>a</sup>	$B_0$			$\alpha$	$\log P_0$
	$70\mu\text{m}$	$100\mu\text{m}$	$160\mu\text{m}$		
$b=10^\circ$	5.4	24.4	53.9	$-3.45\pm 0.11$	$9.00\pm 0.17$
$b=17^\circ$	3.5	18.6	45.3	$-3.50\pm 0.16$	$9.05\pm 0.24$
$b=22^\circ$	3.5	15.3	34.1	$-3.54\pm 0.15$	$8.48\pm 0.22$
$b=28^\circ$	2.2	8.9	24.7	$-3.50\pm 0.15$	$7.74\pm 0.21$
$b=36^\circ$	1.2	6.0	14.4	$-3.80\pm 0.10$	$7.41\pm 0.15$
$b=45^\circ$	0.6	2.8	6.2	$-3.13\pm 0.12$	$6.39\pm 0.18$
$b=59^\circ$	0.3	1.4	2.9	$-2.99\pm 0.09$	$6.00\pm 0.13$
$b=70^\circ$	0.2	1.2	2.6	$-3.20\pm 0.10$	$6.27\pm 0.15$
$b=84^\circ$	0.1	0.8	1.8	$-2.87\pm 0.09$	$5.77\pm 0.14$
$b=90^\circ$	0.1	0.5	1.4	$-2.87\pm 0.08$	$5.66\pm 0.12$

selected regions at a Galactic longitude of  $0^\circ$  among 50 patches in Table 6.3. The estimated power spectrum in Table 6.3 differs from patch to patch. In order to reflect the large structure of the dust map and reduce the discrepancies of the power spectrum between adjacent patches, we use a large area around the patch ( $\sim 2.5^\circ \times 2.5^\circ$ ) in the measurement of the power spectrum.

## 6.4.2 Estimation of Sky Confusion Noise

### Contribution of Instrumental Noise

In order to estimate the sky confusion noise, the structure function for the cirrus emission patch obtained by measuring the sky brightness fluctuations is widely used (Gautier et al. 1992; Herbstmeier et al. 1998; Kiss et al. 2001). The size of the measuring aperture is set to be the FWHM of each beam profile if the detector pixel size is smaller than the FWHM of a beam profile. Since the sky confusion noise and the instrumental noise are statistically independent (Herbstmeier et al. 1998; Kiss et al. 2001), the measured noise  $N_{\text{meas}}$  is

$$N_{\text{meas}}^2 \leq N^2 + \eta \cdot \sigma_{\text{inst}}^2, \quad (6.10)$$

where  $N$  is the sky confusion noise,  $\sigma_{\text{inst}}$  is the instrumental noise and  $\eta$  is the contribution factor from the instrumental noise.  $\eta$  can be determined by the size of the measurement aperture and the separation (see equation 6.2 and figure 6.1). The noise measured in equation 6.10 assumes a constant value for the instrumental noise, however, in reality, the noise level may well change due to the anomalous behaviour of the detectors and the unstable conditions of the in-orbit environment.

### Comparison with Other Results

We estimate the sky confusion noise from the patches of the simulated sky map. In figure 6.7, we plot the fractional area as a function of sky brightness over the whole sky to visualize the sky brightness distribution. Since we consider the sky confusion caused solely by the emission from cirrus structures, we do not include any contribution from

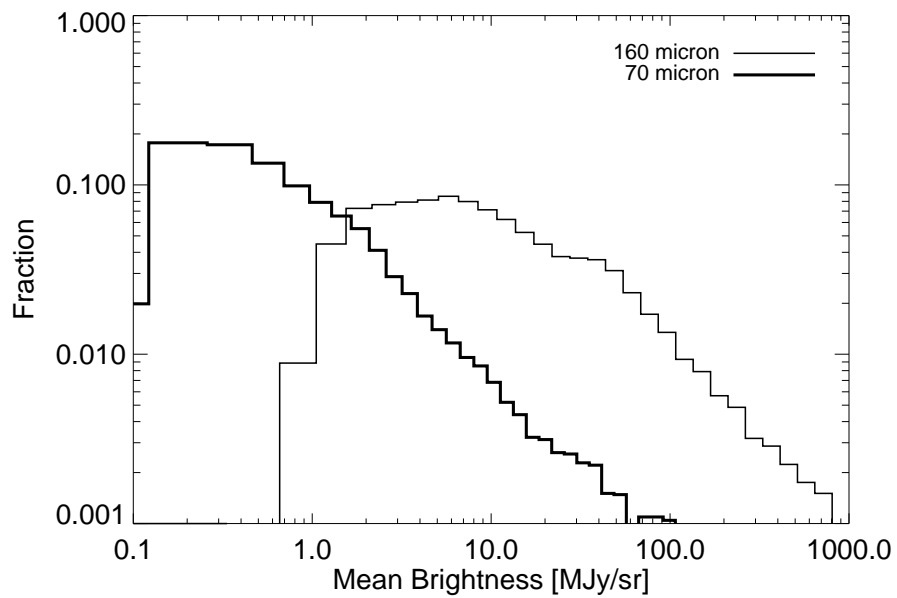


FIG. 6.7: The fraction of the sky brightness for all sky. Note that most of the sky have the sky brightness below 1 MJy sr<sup>-1</sup> (SW) and 15 MJy sr<sup>-1</sup> (LW). The contribution in the highest mean brightness resulted from near the Galactic center.

the instrumental noise in the simulated patches of the sky map that we would expect from equation 6.10.

In order to determine the dependency of the sky confusion noise on separation, we performed a “calculation” for the estimation of sky confusion noise for given mean brightness of the sky patch for each space mission (ISO, Spitzer, ASTRO-F, and Herschel/SPICA) by systematically varying the value of  $k$  from 2 to 7, using equation 6.2. Generally, the larger the separation becomes, the larger the sky confusion noise becomes because we may be estimating the fluctuations from different structures. In practical photometry, large separations are generally used, i.e.,  $\theta = kD$ ,  $k > 2$  in the configuration of figure 6.1 (Laureijs et al. 2000; Kiss et al. 2001). As a reference, we take the estimate of the sky confusion noise with  $k = 2.5$  for a comparison of the measured sky confusion with the photometric results given in section 6.5.

In figures 6.8 – 6.11, we present our estimates of the sky confusion noise for the ISO, Spitzer, ASTRO-F and Herschel/SPICA space missions comparing the formula for the sky confusion noise predicted by HB90 (hereafter HB90 formula). For ISO results, the sky confusion noise with  $k = 2.5$  is overestimated for the dark fields, but underestimated for the bright fields (see figure 6.8). With larger separations, e.g.,  $k = 7$ , the estimated confusion noise approaches the HB90 formula though it is still overestimated for the dark fields. We can see the same tendency in other studies in the sky confusion noise measured from ISO observations (Herbstmeier et al. 1998; Kiss et al. 2001). The measured sky confusion noise for the Spitzer and Herschel/SPICA missions are much lower than the predictions of HB90 except for the dark fields (see figures 6.10 and 6.11).

Comparing the empirical relation between  $P_0$  and  $B_0$  by Gautier et al. (1992), we present our estimated  $P_0$  in figure 6.12. It shows a lower  $P_0$  in bright fields and the higher  $P_0$  in dark fields could cause an underestimation in the bright fields and an overestimation in the dark fields of the sky confusion noise. This inconsistency, overestimation of  $P_0$  in bright fields and underestimation of  $P_0$  in dark fields, also appears in other regions of the sky. By fitting our estimations of  $P_0$ , we obtained a new relation between the  $P_0$  and  $B_0$ . The HB90 formula assumed that this empirical relation is valid

in other wavelengths. However, although the cirrus structure is generally preserved in other wavelengths, the empirical relation should be scaled according to the variation of the cirrus brightness with wavelength, i.e, cirrus spectral energy distribution. Therefore, in order to apply our empirical formula to other wavelength bands, we need some additional correction. For this correction, we used the ratio of the mean brightness at the two wavelengths, e.g.,  $B_{160\mu\text{m}}/B_{100\mu\text{m}} \sim 2$  (see Table 6.3). For comparison with the sky confusion noise estimated from the ISO mission, we plot the HB90 formula to which our empirical relation is applied (see thick dotted line in figure 6.8). Though the revised HB90 formula solve the discrepancies of our estimations to some extent, there are still disagreements especially with the results for higher resolution missions.

The HB90 formula was obtained from the analysis of the low resolution IRAS data at 100  $\mu\text{m}$  and assumed a constant power index for the cirrus power spectrum. In the case of the high resolution missions, since the sky confusion becomes sensitive to the local structure rather than the large scale structure, the calculation of the sky confusion strongly depends upon the power spectrum estimated for each patch and the power at the scale length corresponding to the resolution of the detector. Therefore, we should consider carefully the combination of the resolution and the power spectrum of the cirrus in the estimation of the sky confusion noise. In addition, the larger discrepancy in the bright regions for the ASTRO-F mission compared with the prediction from ISO observations can be explained by an increase in the spatial resolution, although the aperture sizes of two telescopes are similar (see the specifications of the two space missions in Table 6.1). We conclude that the sky confusion level predicted by the IRAS data from which HB90 formula are derived is significantly overestimated in the case of the higher resolution missions.

Generally the most significant component of the extragalactic background in the far-IR is the cirrus emission, however, at high spatial frequencies the Cosmic Far-IR Background (CFIRB) fluctuations may become dominant (Schlegel, Finkbeiner & Davis 1998; Guiderdoni et al. 1997; Juvela, Mattila & Lemke 2000). Therefore, in any estimation of the sky confusion noise using observational data in the dark fields should consider the fluctuation due to the CFIRB. By fitting the sky confusion noise over the

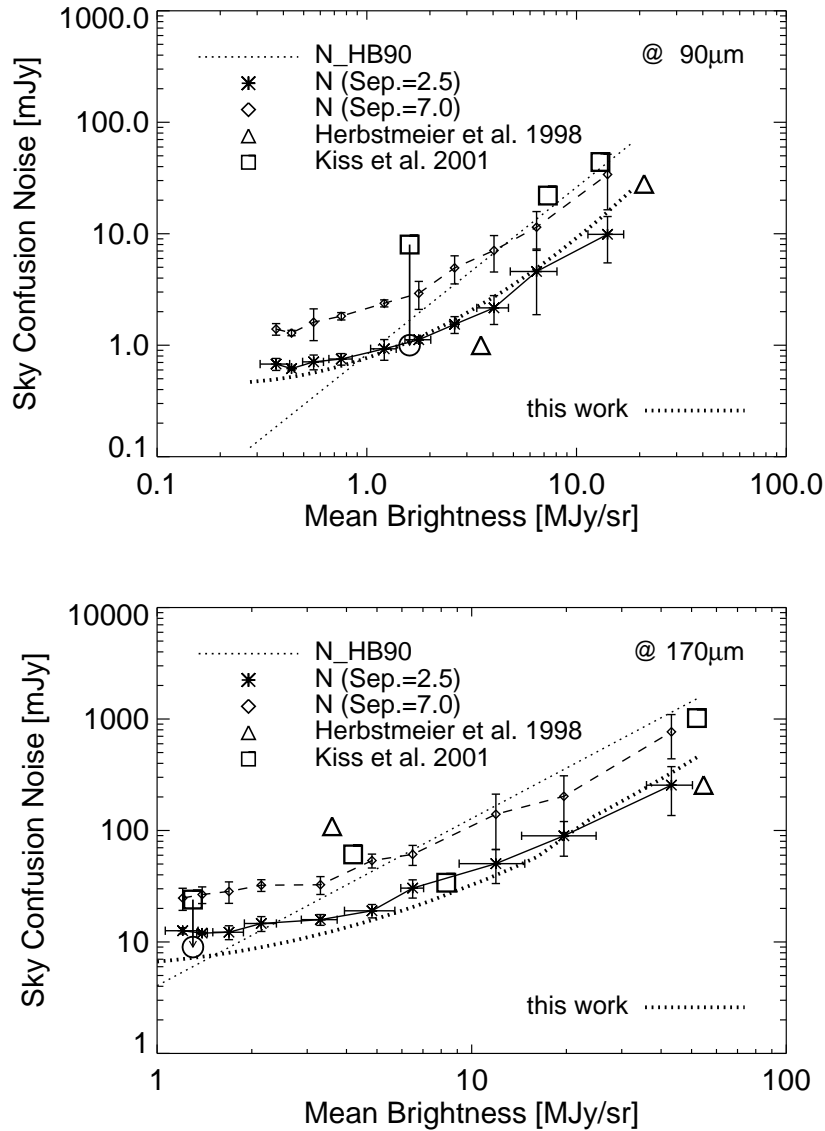


FIG. 6.8: Estimated sky confusion noise for the ISO mission. Upper and lower panels show the sky confusion noise at  $90\ \mu\text{m}$  and  $170\ \mu\text{m}$ , respectively. The dotted line shows the sky confusion noise by HB90 (Helou & Beichman 1990). The symbols are the estimated sky confusion noise on averaging 5 patches with similar mean brightness. For comparison, we plot the estimated sky confusion noise for the larger separation of  $k = 7$ . The circle symbol means the sky confusion noise correcting the contribution from the CFIRB. The thick dotted line is the HB90 formula to which our empirical relation is applied.

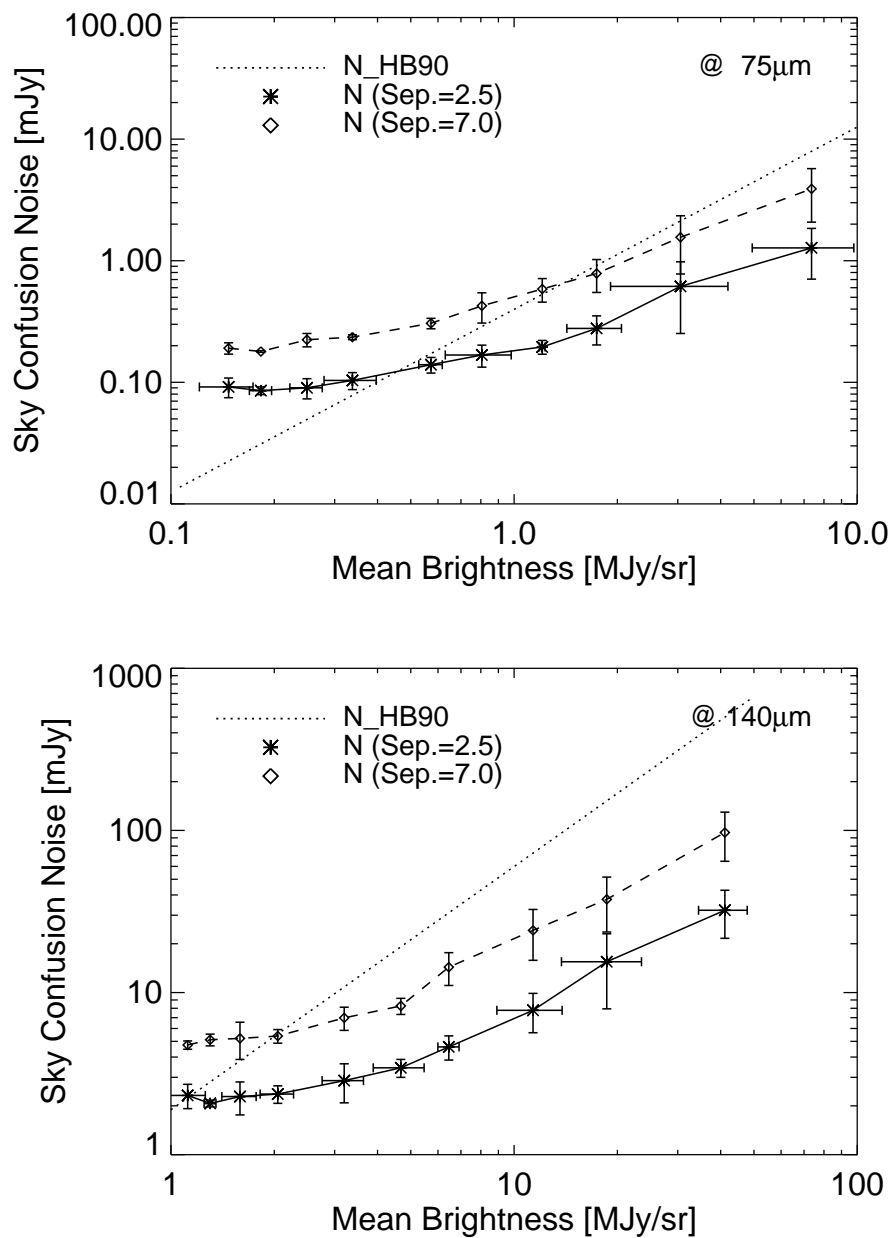


FIG. 6.9: Estimated sky confusion noise for the ASTRO-F mission. Left and right panels show the sky confusion noise in the WIDE-S band ( $75 \mu\text{m}$ ) and WIDE-L band ( $140 \mu\text{m}$ ), respectively. The symbols and lines are same as given in figure 6.8.

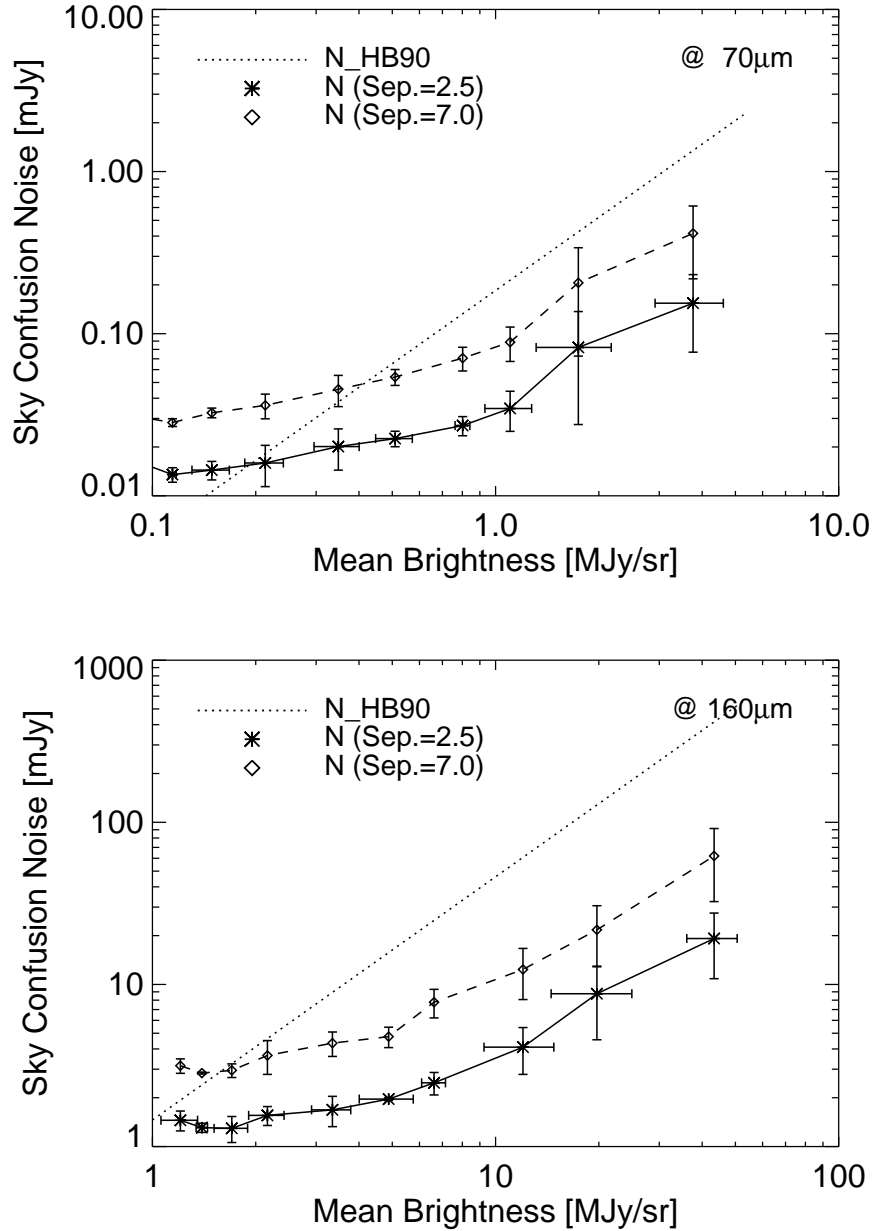


FIG. 6.10: Estimated sky confusion noise for the Spitzer mission. Left and right panels show the sky confusion noise for the MIPS 70  $\mu\text{m}$  and 160  $\mu\text{m}$  bands, respectively. The symbols and lines are same as in figure 6.8.

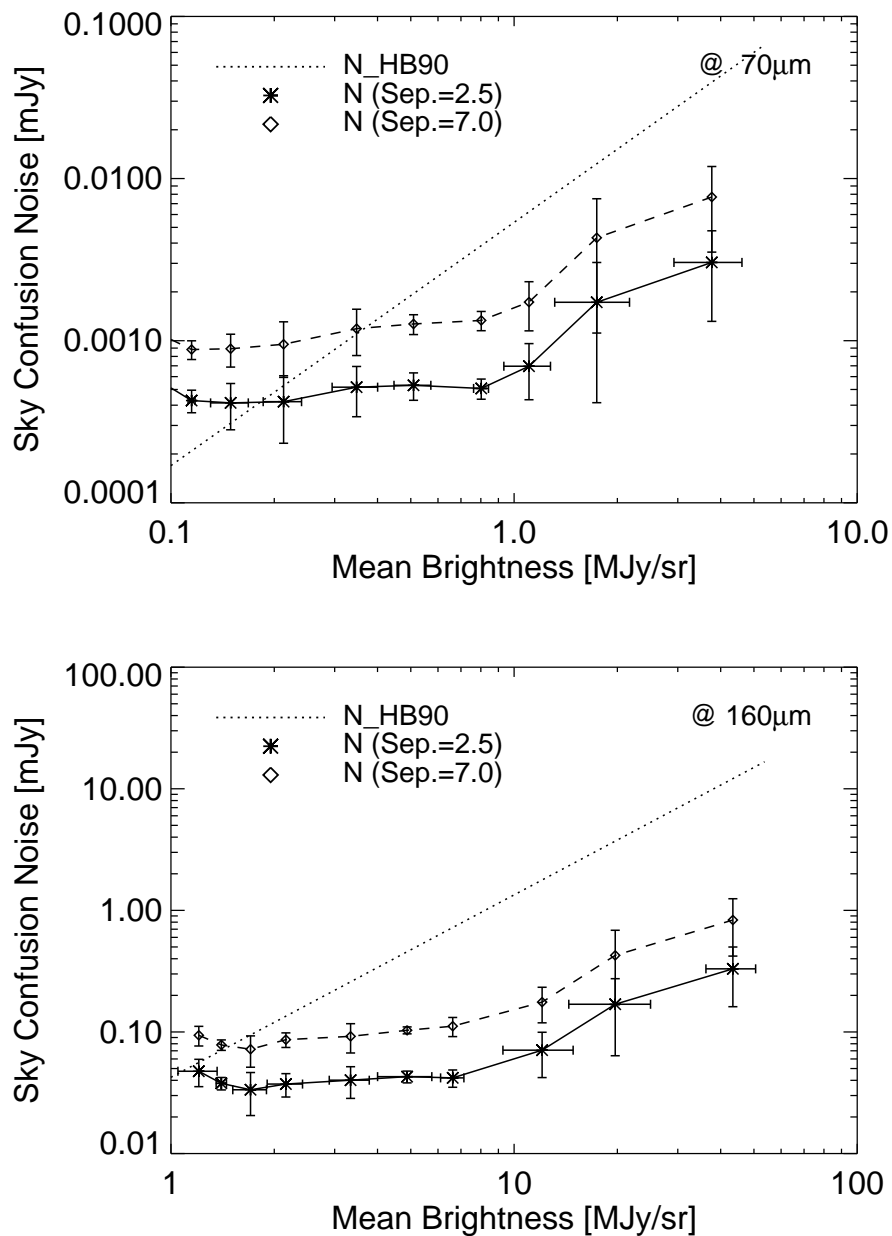


FIG. 6.11: Estimated sky confusion noise for the Herschel and SPICA missions. Left and right panels show the sky confusion noise at  $70 \mu\text{m}$  and  $160 \mu\text{m}$ , respectively. The symbols and lines are same as in figure 6.8.

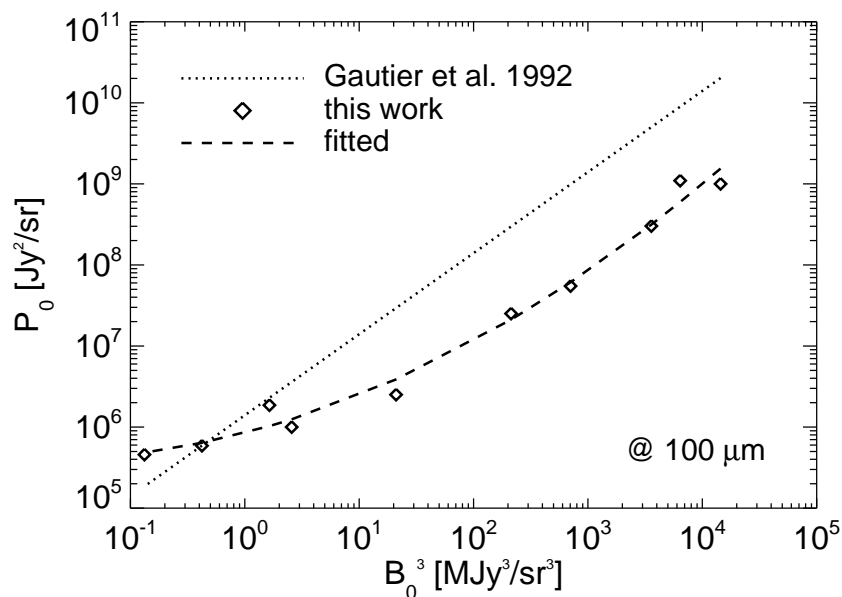


FIG. 6.12: The relation between  $P_0$  and  $B_0^3$ . The dotted line is the result from Gautier et al. (1992), the symbol is from our estimated  $P_0$ , and the dashed line is the fit to our result. In bright fields, values of  $P_0$  expected from Gautier et al. (1992) have higher values than those measured from our patches in bright fields.

mean sky brightness, Kiss et al. (2001) obtained CFIRB fluctuation of  $7 \pm 2$  mJy at  $90 \mu\text{m}$  and  $15 \pm 4$  mJy at  $170 \mu\text{m}$ . After correcting for the contribution of the CFIRB in the estimation of the sky confusion noise, we obtained results similar with those of Kiss et al. (2001) in the dark fields (see the symbol in circle with arrow in figure 6.8 at the mean brightness of  $\sim 1.5$  MJy/sr). Since the CFIRB fluctuations strongly depend upon the extragalactic source count model, we will discuss this issue in greater depth in our forthcoming paper [Jeong et al. 2004c (Paper II), in preparation].

### Sky Confusion Noise for Various Separations

Kiss et al. (2001) analyzed the dependency of the sky confusion noise on larger separations by the simple power expression from ISO observation data:

$$N(q \cdot \theta_{\min}) = N(\theta_{\min}) \times q^\gamma, \quad (6.11)$$

where  $q = 1, \frac{3}{2}, \dots, \frac{7}{2}$  and  $\gamma$  is a constant for a specific map. We check this dependency by fitting  $\gamma$  for all patches as given in figure 6.13. The brighter the sky becomes, the higher  $\gamma$  becomes due to the prominent structure of the cirrus emission. Kiss et al. (2001) obtained a much lower  $\gamma$  in dark regions, but their values of  $\gamma$  in other regions are similar to our results. This result can be explained by two possible effects: one is that the cirrus structure observed by ISO is blurred by the instrumental noise in most of the dark regions and the other is that many extragalactic point sources below the detection limit, i.e. CFIRB fluctuations, can remove the cirrus structure. If we only consider the component due to the cirrus in the dark fields, the values of  $\gamma$  in the dark regions by Kiss et al. (2001) are similar to our results. In most of the bright regions, the scatter of  $\gamma$  shows the similar trend and this is probably caused by the relatively large difference in the spatial structure in each region. For the Herschel and SPICA missions, our estimations show that  $\gamma$  slowly increases and the error decreases compared to other missions. This is due to the much higher resolution than the other missions considered.

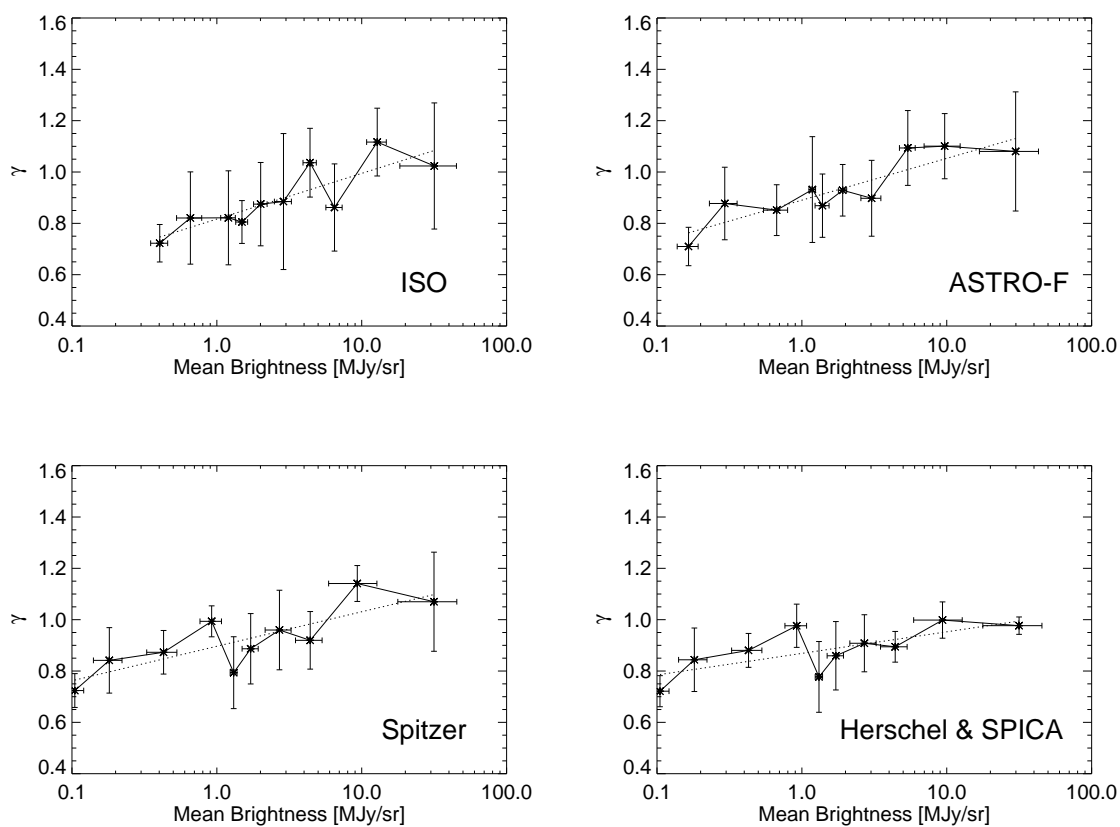


FIG. 6.13: Dependency of the sky confusion noise on separation for ISO, ASTRO-F, Spitzer, Herschel and SPICA, respectively. The dotted line is a fit to our estimation analysis data. In the brighter regions,  $\gamma$  has higher values than in the dark fields.

### Effect by Changing Power Index $\alpha$

In this study, we assume that the structure of cirrus is independent of wavelength. Kiss et al. (2003) suggest however that the power index of the power spectrum also depends upon both the wavelength and the surface brightness due to the coexistence of dust components with various temperatures within the same field and cold extended emission features (usually,  $-2.0 < \alpha < -4.0$ ). Using the assumption that the sky confusion noise is proportional to the scale length (see equation 6.4), we can estimate the sky confusion for different power indices. The ratio  $\psi$  of the sky confusion noise with the power index of  $\alpha + \epsilon$  to that with the power index of  $\alpha$  can be defined as:

$$\psi = \frac{N(\alpha + \epsilon)}{N(\alpha)}, \quad (6.12)$$

where  $\epsilon$  is the contribution to the power index from any other structure in the power spectrum. In this calculation, we fix the power at the scale length of the resolution limit of the map ( $\sim 6.1$  arcmin) at  $100 \mu\text{m}$  from the assumption that the power over this scale is not changed by the components proposed by Kiss et al. (2003). Table 6.4 lists the ratio of the sky confusion noise for the different power indices for each space mission. Since the fluctuation at smaller scales is more sensitive to the power index, the sky confusion noise is much more dependent upon the power index for the space missions with higher resolutions.

## 6.5 PHOTOMETRIC MEASUREMENTS OF SKY CONFUSION NOISE

In section 6.4, we estimated the sky confusion noise via the fluctuation analysis. The sky confusion noise should affect the source detection efficiency, causing a deterioration in the detection limit. In this section, we obtain the measured sky confusion noise by carrying out photometry on simulated images.

TABLE 6.4: Ratio  $\psi$  of the sky confusion noise for the different power indices.

Space Mission	$\epsilon^a = -1.0$		$\epsilon = 1.0$	
	SW	LW	SW	LW
ISO	0.13	0.19	1.7	1.2
Spitzer	0.083	0.12	2.8	1.9
ASTRO-F	0.10	0.13	2.2	1.8
Herschel	0.041	0.061	5.6	3.8
SPICA	0.041	0.061	5.6	3.8

<sup>a</sup> contribution index in the power spectrum.

### 6.5.1 Source Distribution

The distribution of sources per unit area on the sky can be described as a function of the flux density and depends upon both the spatial distribution of the sources and their luminosity function. For simplicity, we assume the number of sources whose flux is greater than flux  $S$ ,  $n(> S)$ , is a power-law function of  $S$ ,

$$n(> S) = n_0(> S_0) \left( \frac{S}{S_0} \right)^{-\omega}, \quad (6.13)$$

for  $S_{\min} < S < S_{\max}$ , where  $n_0$  and  $S_0$  are normalization constants for number of sources and for flux, respectively,  $S_{\min}$  is the minimum flux,  $S_{\max}$  is the maximum flux in the source distribution, and  $\omega$  is the power index of the distribution of sources.

The source confusion caused by the overlapping of adjacent sources mainly depends upon the source distribution and the beam profile (Condon 1974; Franceschini et al. 1989). Source confusion becomes important as the observation sensitivity increases since there are usually more faint sources than brighter ones. Currently fashionable source count models require strong evolution in order to fit the observation data from the ISO mission from mid- to far-IR, the SCUBA data at sub-mm wavelengths, and

the Cosmic Infrared Background (CIRB) at  $170 \mu\text{m}$  (Oliver et al. 1997; Smail, Ivison & Blain 1997; Kawara et al. 1998; Hughes et al. 1998; Aussel et al. 1999; Puget et al. 1999; Efstathiou et al. 2000; Serjeant et al. 2000; Lagache et al. 2000; Matsuhara et al. 2000; Scott et al. 2002). In our study, we use a simple source distribution for the purpose of investigating only the effect of the sky confusion. We will discuss the source confusion with more realistic source count models in the forthcoming paper [Jeong et al. 2004c (Paper II), in preparation]. In order to avoid the contributions from any source confusion itself, we take only a small number of sources. However, the estimate of detection limit becomes rather uncertain, if there are too few sources. Therefore, we have employed a model for the  $n(S)$  utilizing a distribution with two slopes,  $\omega = 1.0$  for bright flux end and  $\omega = 0.3$  for faint flux end ( see figure 6.14), in order to derive an accurate value for the sky confusion limit without source confusion effect. Since the sky confusion noise in the SW bands is much lower than that in the LW bands, we set different normalization constants and minimum flux values  $S_{\text{min}}$ , i.e.,  $S_{\text{min}} = 0.001$  mJy and  $n_0(> S_0) = 3$  in the SW band,  $S_{\text{min}} = 0.1$  mJy and  $n_0(> S_0) = 10$  in the LW band, where  $S_0$  is set to be 100 mJy (see figure 6.14).

### 6.5.2 Source Detection

We generate images including point sources with the beam profile of each mission using the source distribution described in section 6.5.1. Figure 6.16 shows the simulated images for the various missions considered. The smaller the detector pixel and the beam profile become, the more sources and the smaller structure in the cirrus emission appear.

We carried out aperture photometry on the simulated images using the SExtractor software *v2.0.0* (Bertin & Arnouts 1996). The most influential parameters are the size of background mesh and the threshold for the source detection in this aperture photometry. We set the size of the background mesh to 2.5 times of the measuring aperture, and the detection threshold as 4, which is optimized for better reliability of the detected sources and reducing false detection rate. The final detection limit

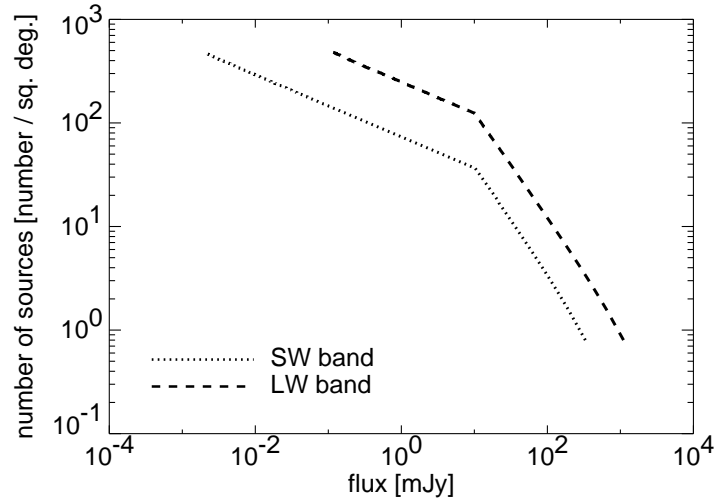


FIG. 6.14: Source distribution in the SW band and LW band. We use different slopes ( $\omega = 1.0$  and  $\omega = 0.3$ ) for the power law source distribution at the boundary flux of 10 mJy in order to reduce the effect of the source confusion.

is determined by the minimum flux of detected point sources. We found that the detection limits determined from  $4\sigma$  criteria are consistent with the 4 times of sky confusion noise measured from the statistical analysis. Note that our estimated sky confusion noise is a  $1\sigma$  fluctuation. In figure 6.17, we compare the detection limit by photometry with the sky confusion noise for each mission. For the ISO and ASTRO-F missions, the results from photometry give relatively higher detection limits than the theoretical estimations via fluctuation analysis. This trend results from the larger detector pixel size compared with the FWHM of the beam profile. The large detector pixel size of the ISO mission significantly degraded the performance of the detection of the point sources (e.g., the left panels in figure 6.17).

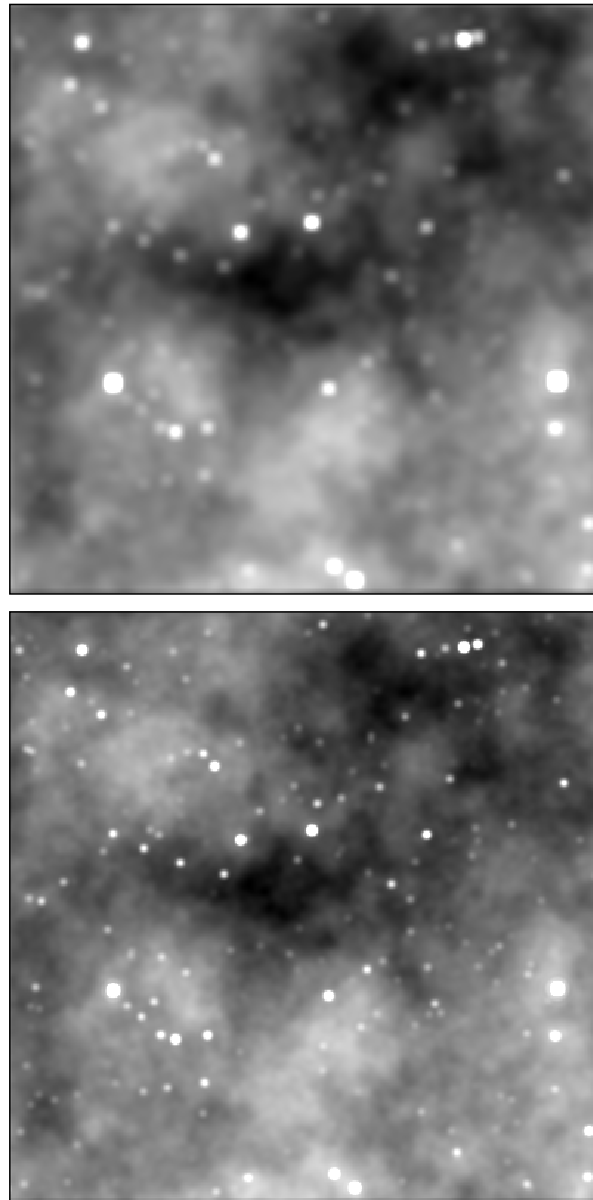


FIG. 6.15: Simulated images including point sources in the LW band for ISO (upper), ASTRO-F (lower) missions. The mean brightness of the cirrus background is  $2 \text{ MJy sr}^{-1}$  at  $160 \mu\text{m}$ .

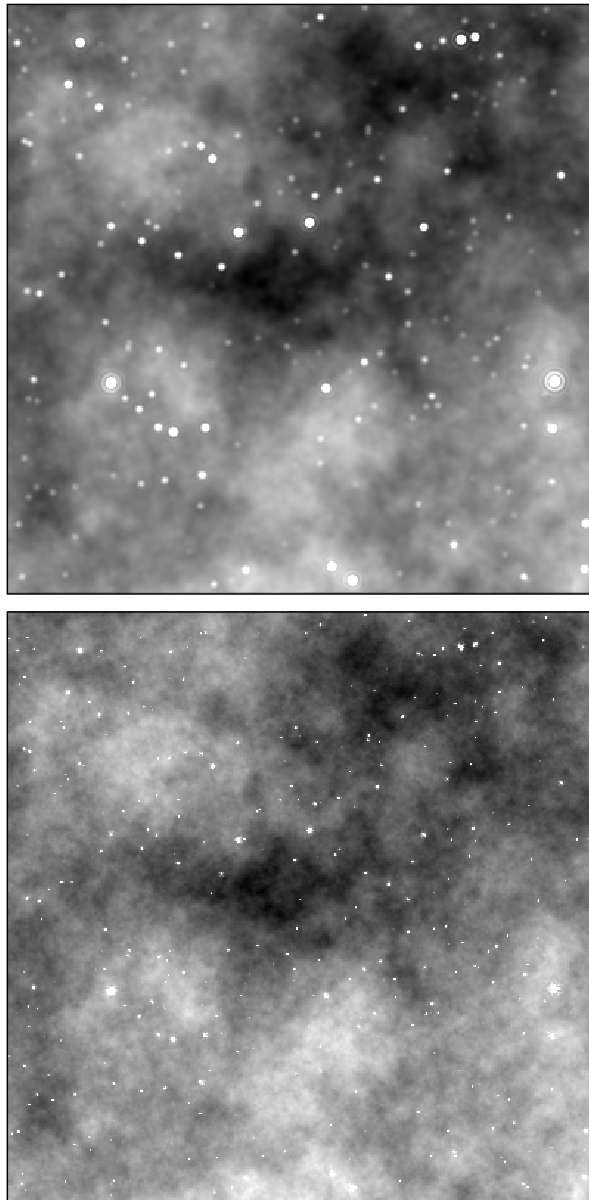


FIG. 6.16: Simulated images including point sources in the LW band for Spitzer (upper) , and Herschel and SPICA (lower) missions. The mean brightness of the cirrus background is  $2 \text{ MJy sr}^{-1}$  at  $160\mu\text{m}$ .

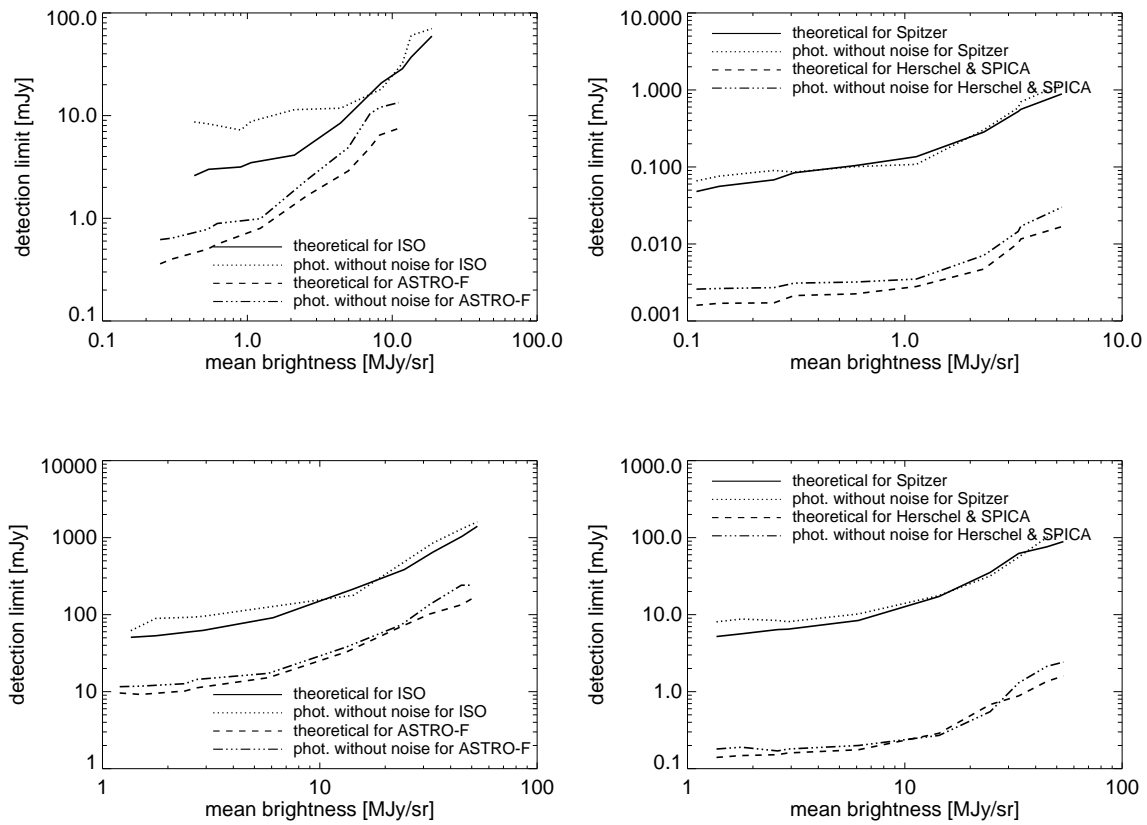


FIG. 6.17: Estimated detection limit by photometry. Figures show the detection limit and 4 times sky confusion noise estimated from the statistical analysis for the ISO and ASTRO-F missions (left) and Spitzer, Herschel and SPICA missions (right). Upper and lower panels show the results for the SW band and LW band, respectively.

## 6.6 INCLUSION OF INSTRUMENTAL NOISE

We have considered the basic instrumental parameters in estimating the sky confusion noise due to the IR cirrus. However, the measurement of the sky confusion noise from images is also affected by instrumental noise sources as discussed in section 6.4.2 mainly due to readout and photon noise. The readout process can cause a fluctuation of the signal and of the sky background which is manifested as photon noise (Thronson et al. 1995). While the readout noise can be regarded as constant, photon noise varies from place to place over the sky because the photon noise depends upon the amount of photon flux from the sky background.

To create an accurate observing simulation for the far-IR all sky survey in the ASTRO-F mission, we have written a suite of software, FIS Virtual Instrument (FISVI) which takes into account many realistic detector effects including noise characteristics based upon laboratory measurements (Jeong et al. 2003; ; Jeong et al. 2004b). Using this simulator, we generate realistic images including instrumental noise, which allow us to determine realistic detection limits in order to check the effect of the instrumental noise depending on the amount of background emission. Taking the instrumental parameters of the ASTRO-F satellite, we calculate the instrumental noise  $\sigma_{\text{inst}}$  over the sky brightness including the readout noise (see Jeong et al. 2003 for details).

$$\sigma_{\text{inst}} = \sqrt{\sigma_{\text{ph}}^2 + \sigma_{\text{r}}^2}, \quad (6.14)$$

where  $\sigma_{\text{ph}}$  and  $\sigma_{\text{r}}$  are the fluctuations due to the photon and readout noise, respectively.

Assuming that the detection limit estimated by the photometry (see figure 6.17) reflects the sky confusion noise, we estimate the total noise  $\sigma_{\text{tot}}$  by the summation of these noise sources.

$$\sigma_{\text{tot}} = \sqrt{\sigma_{\text{inst}}^2 + \sigma_{\text{sc}}^2}, \quad (6.15)$$

where  $\sigma_{\text{sc}}$  is the sky confusion noise estimated by photometry.

Figure 6.18 shows a comparison between the photometric results and the estimated sky confusion noise. The detection limit including the instrumental noise slowly deteriorates as the sky brightness increases because the instrumental noise dominates in the

dark fields. The total noise as summation of the sky confusion noise and the instrumental noise agrees with the detection limits determined by the photometry. Therefore, we can estimate the detection limits including the sky confusion and the instrumental noise for other space missions taking the detailed information of the instrumental noise.

## 6.7 SUMMARY AND DISCUSSION

Based on the observed  $100\ \mu\text{m}$  dust map and the models of a dust spectrum, we generated a high resolution background map at other wavelengths. Using these simulated patches of the cirrus map, we estimated the sky confusion noise for various IR space missions such as ISO, Spitzer, ASTRO-F, Herschel and SPICA, through statistical analysis. Since we have the observation results which are currently available only from ISO, we compared the results of our simulation with the ISO observation data. We found that the sky confusion noise estimated with our simulated patches are consistent with the ISO results. However, in the dark fields the sky confusion noise is less dependent upon the beam separation parameter than in the bright fields in the case of the ISO observation. We conclude that this is due to the dominant instrumental noise in the dark regions or alternatively, the CFIRB fluctuation. We also found that the sky confusion predicted from the IRAS data is significantly overestimated in the case of the large aperture telescopes, except in the dark fields.

We have confirmed our results through a realistic simulation. We performed photometry on simulated images including point sources with a sparse source distribution in order to avoid the effects of confusion due to crowded point sources. The detection limits obtained from the photometric analysis agree with the estimated sky confusion noise except for ISO and ASTRO-F. This discrepancy is due to the large detector pixel size compared with the FWHM of the beam size. We also obtained photometric results including the instrumental noise for ASTRO-F mission utilizing specific detailed information of the instruments. The estimated detection limits are consistent with the summation of the instrumental noise and the sky confusion noise.

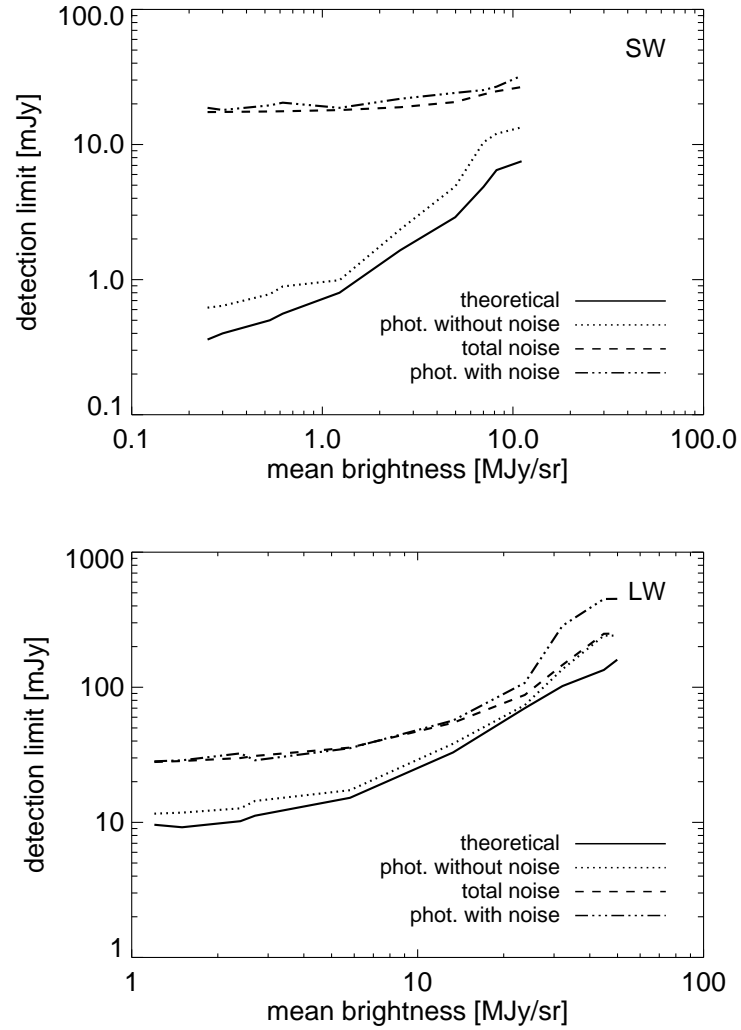


FIG. 6.18: The comparison between the photometric results and the estimated sky confusion noise. The lines are same as given in figure 6.17. The dashed dotted line is the photometric results including the instrumental noise and the dashed line is the total noise estimated from equation 6.15.

The mean brightness of the cirrus emission usually decreases with increasing galactic latitude (Boulanger & Péroult 1988). Boulanger & Péroult (1998) also derived a simple formula for the mean brightness of the cirrus emission in fitting to the galactic latitude distribution of the cirrus emission. In order to estimate the detection limits as a function of galactic latitude distribution of the cirrus emission, we also derived this simple formula for each wavelength band. Because the cirrus emission is extremely strong near the galactic centre, we confined our galactic latitudes to above  $10^\circ$ . Figure 6.19 shows the detection limits as a function of galactic latitude. The detection limits for all missions appear to saturate by a galactic latitude of  $\sim 30^\circ$ .

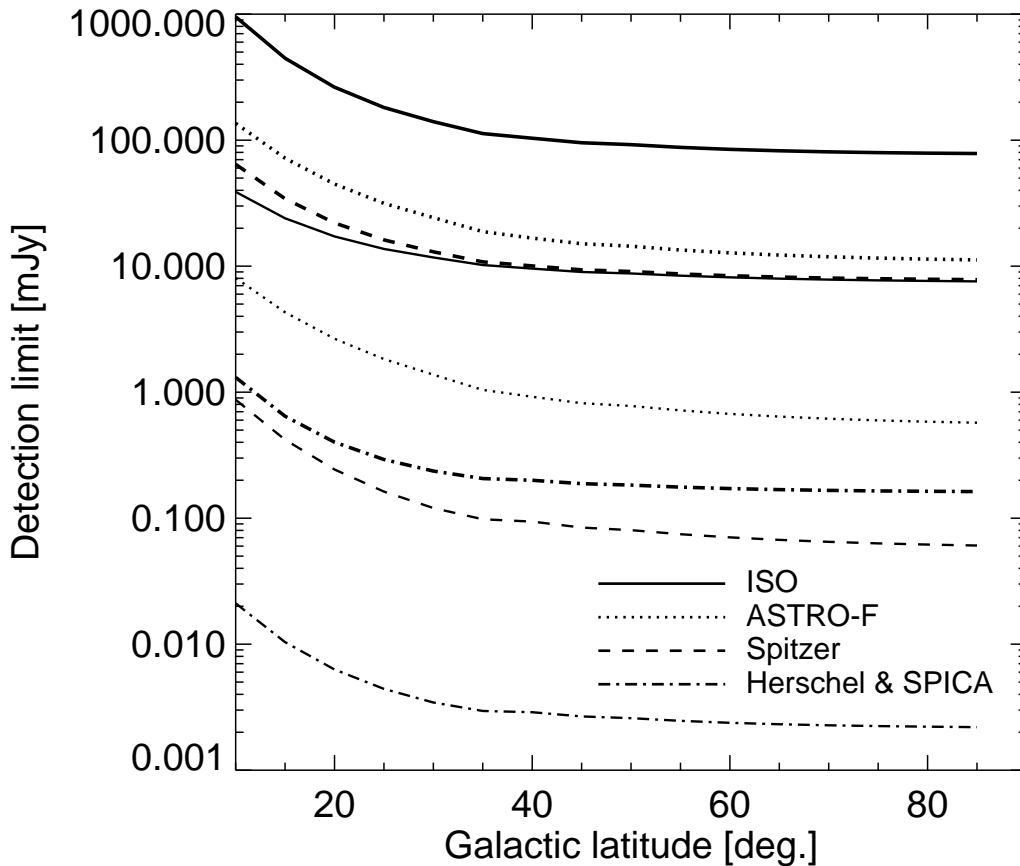


FIG. 6.19: Detection limits due to the Galactic cirrus as a function of Galactic latitude. The two line plotted for each mission are for the SW band (lower line) and the LW band (upper line).

Figure 6.20 summarises the final detection limits for point sources at mean and low sky brightness due to the Galactic cirrus. In addition, we also plot the current  $5\sigma$  assumed detection limit for a point source for each mission. This detection limit does not include the confusion noise (both source confusion and sky confusion). The integration time is 500 sec for the Spitzer mission (Spitzer Observer's Manual<sup>1</sup>) and 1 hour for the Herschel mission (Pilbratt 2003). As shown in figure 6.20, sky confusion almost approaches the detection limit in the LW band of the ASTRO-F and Spitzer missions. Though the sky confusion does not severely affect the detection limits of Herschel mission, it can affect the detection limit of the SPICA mission because the SPICA mission will have a large aperture telescope cooled to very low temperatures in order to achieve exceptional sensitivity in the far-IR (see Nakagawa 2004 for the detailed information of the SPICA mission).

---

<sup>1</sup>Further information on the sensitivity of Spitzer mission can be found at the following url: <http://ssc.spitzer.caltech.edu/mips/sens.html>

W.-S. Jeong was financially supported by the BK21 Project of the Korean Government. This work was financially supported in part by the KOSEF Grant R14-2002-058-01000-0. Chris Pearson acknowledges a European Union Fellowship to Japan. We thank Kyung Sook Jeong for careful reading our manuscript and fruitful suggestions.

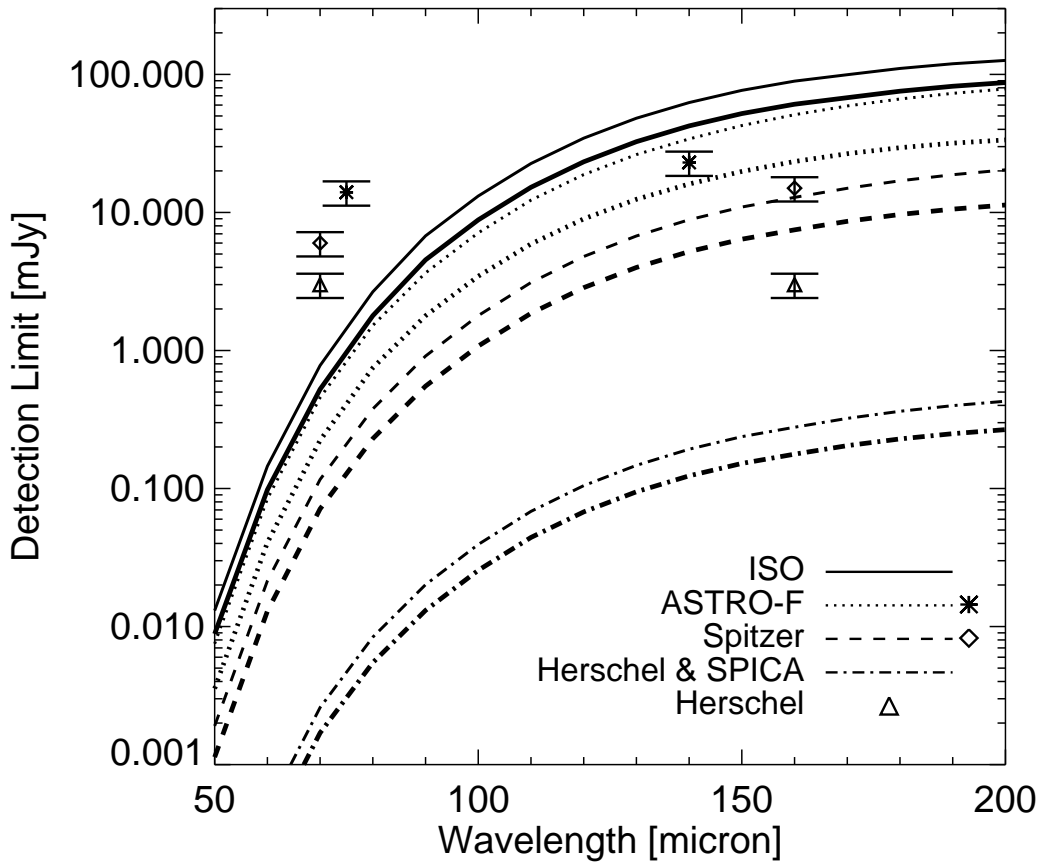


FIG. 6.20: Detection limits due to Galactic cirrus at mean and low sky brightness in each band. The mean sky brightness in the SW and LW bands is set to  $1 \text{ MJy sr}^{-1}$  and  $15 \text{ MJy sr}^{-1}$ , respectively. The lower value for each detection limit corresponds to the detection limit at low sky brightness usually at high Galactic latitudes. The symbol shows the  $5\sigma$  sensitivity for the ASTRO-F, Spitzer, Herschel missions without confusion and the error bar corresponds to  $1\sigma$  sensitivity.

## REFERENCES

- Ábrahám P., Leinert C., Lemke D., 1997, *A&A*, 328, 702
- Aussel H., Cesarsky C.J., Elbaz D., Starck J.L., 1999, *A&A*, 342, 313
- Bertin E., Arnouts S., 1996, *A&AS*, 117, 393
- Boggess N. W. et al., 1992, *ApJ*, 397, 420
- Boulanger F., Péroult M., 1988, *ApJ*, 330, 964
- Condon J. J., 1974, *ApJ*, 188, 279
- Draine B. T., Lee H. M., 1984, *ApJ*, 285, 89
- Efstathiou A. et al., 2000, *MNRAS*, 319, 1169
- Finkbeiner D. P., Davis M., Schlegel D. J., 1999, *ApJ*, 524, 867
- Franceschini A., Toffolatti L., Danese L., De Zotti G., 1989, *ApJ*, 344, 35
- Gallagher D. B., Irace W. R., Werner M. W., 2003, *SPIE*, 4850, 17
- Gautier T. N. III, Boulanger F., Péroult M., Puget J. L., 1992, *AJ*, 103, 1313
- Gott J. R., Park C., 1990, *ApJ*, 352, 1
- Guiderdoni B. et al., 1997, *Nature*, 390, 257
- Helou G., Beichman C. A., 1990, *Proc. of the 29th Liege International Astrophysical Coll.*, ESA Publ., 117

- Herbstmeier U., Ábrahám P., Lemke D., Laureijs R. J., Klaas U. et al., 1998, *A&A*, 332, 739
- Hughes D. et al., 1998, *Nature*, 394, 241
- Jeong W.-S., Pak S., Lee H. M. et al., 2003, *PASJ*, 55, 717
- Jeong W.-S., Pak S., Lee H. M. et al., 2004a, *Adv. Space Res.*, in press
- Jeong W.-S., Pak S., Lee H. M. et al., 2004b, *Adv. Space Res.*, in press
- Jeong W.-S., C. P. Pearson et al., 2004c, in preparation (Paper II)
- Juvela M., K. Mattila, D. Lemke, 2000, *A&A*, 360, 813
- Kawara K. et al., 1998, *A&A*, 336, L9
- Kelsall T. et al., 1998, *ApJ*, 508, 44
- Kiss C., Ábrahám P., Klaas U., Juvela M., Lemke D., 2001, *A&A*, 379, 1161
- Kiss C., Ábrahám P., Klaas U. et al., 2003, *A&A*, 399, 177
- Lagache G., Haffner L.M., Reynolds R.J., Tufte S.L., 2000, *A&A*, 354, 247
- Laureijs R. J., Klaas U., Richards P.J., Schulz B., Ábrahám P., 2000, *The ISO Handbook*, vol. V, PHT-Imaging Photo-Polarimeter, SAI/99-069/Dc, Version 1.2, ISO Data Centre, Villafranca del Castillo
- Low F. J., Beintema T. N., Gautier F. C. et al., 1984, *ApJ*, 278, 19L
- Matsuhara H. et al., 2000, *A&A*, 361, 407
- Miville-Deschênes M.-A., Lagache G., Puget J.-L., 2002, *A&A*, 293, 749
- Murakami H., 1998, *SPIE*, 3356, 471

- Nakagawa T., 2001, in the Proc of The Promise of the Herschel Space Observatory, ed. G. L. Pilbratt, J. Cernicharo, A.M. Heras, T. Prusti, & R. Harris, ESA-SP, 460, pp. 67-74
- Nakagawa T., 2004, *Adv. Space Res.*, in press
- Oliver S. J. et al., 1997, *MNRAS*, 289, 471
- Park C., Vogeley M. S., Geller M. J., Huchira J. P., 1994, *ApJ*, 431, 569
- Peacock J. A., 1999, *Cosmological Physics* (Cambridge: Cambridge University Press)
- Pearson C. P. et al., 2004, *MNRAS*, 347, 1113
- Peebles P. J. E., 1980, *The Large-Scale Structure of the Universe* (Princeton: Princeton University Press)
- Pilbratt G. L., 2003, *SPIE*, 4850, 586
- Poglitsch A., Waelkens C., Geis N., 2003, *SPIE*, 4850, 662
- Pollack J. B., Hollenbach D., Beckwith S., Simonelli D. P., Roush T. et al., 1994, *ApJ*, 421, 615
- Puget J. L. et al., 1999, *A&A*, 345, 29
- Reach W. T. et al., 1995, *Nature*, 374, 521
- Schlegel D. J., Finkbeiner D. P., Davis M., 1998, *ApJ*, 500, 525 (SFD98)
- Scott S.E. et al., 2000, *MNRAS*, 331, 817
- Serjeant S. B. G. et al., 2000, *MNRAS*, 316, 768
- Shibai H., 2000, in *IAU Symp. 204, The extragalactic background and its cosmological implications*, ed. M. Harwit & M. G. Hauser (Michigan: Astronomical Society of the Pacific), 455

Smail I., Ivison R.J., Blain A.W., 1997, ApJ, 490, L5

Thronson H. A., Rapp D., Bailey B., Hawarden T. G., 1995, PASP, 107, 1099

Wheelock S. L. et al., 1994, IRAS Sky Survey Atlas: Explanatory Supplement (Pasadena: JPL 94-11)

White M., Carlstrom J. E., Dragovan M. et al., 1999, ApJ, 514, 12

# Chapter 7

## Probing Confusion Including Source Confusion<sup>#</sup>

### Abstract

We investigate the confusion limit due to both Galactic cirrus and the superposition of extragalactic point sources for the current  $\sim 60\text{--}90$  cm aperture missions such as Spitzer (SIRTF) and ASTRO-F. We consider whether the theoretical estimates are realistic and discuss the competing necessities of reliability and completeness. We find the best estimator for representing the source confusion. By our definition of source confusion, we estimate the confusion using the source count models considering the galaxy evolution. We also discuss the effect of confusion on future large aperture missions such as the ESA Herschel mission and Japanese SPICA mission. From the confusion limits, we obtain the expected redshift distribution for our source count models. Finally, we predict the Cosmic Far-Infrared Background (CFIRB) which includes the information about the number and distribution of contributing sources.

---

<sup>#</sup>W.-S. Jeong, C. P. Pearson, H. M. Lee, et al., 2004, MNRAS, in preparation

## 7.1 INTRODUCTION

The absolute sensitivity of a given space born instrument/telescope system is governed by 2 basic classes of noise; instrumental & photon noise and sky confusion noise. Instrumental noise is intrinsic to the system and is contributed to by such factors as readout noise, dark current fluctuations, flat-fielding uncertainties etc. On the other hand, sky confusion noise is observational dependent and can arise from both the superposition of sources in crowded fields and from extended structures which vary in surface brightness on scales of the telescope and instrument resolution. At infrared wavelengths, the major components are the sky confusion due to interplanetary dust bands (zodiacal light, in the range  $5 < \lambda < 60\mu\text{m}$ ), the sky confusion due to dust emission from irregular interstellar clouds at high galactic latitudes known as the infrared galactic cirrus Low et al. 1984, confusion due to stars at near infrared wavelengths and the confusion due to the fluctuation of the extragalactic background built up by the superposition of individual faint sources below the resolution of the telescope beam. In the far-infrared range, the sky confusion due to galactic cirrus structure and the source confusion due to the unresolved extragalactic sources are the most important two factors to limit the astronomical observations.

Confusion can cause centroid position shifts and flux uncertainties leading to positional errors and spurious sources. Therefore, a careful consideration must be given to the treatment of confusion noise and the confusion limit, as in reality, the confusion noise is a convolution of the observational phenomenon and the observing instrument.

Though the confusion is the fundamental limit to detect the point sources, the sources and cirrus structure below the confusion limit make the background fluctuation. The measurement of background fluctuations is the key to reveal the information about the contributing source distribution and the cirrus structure. There have been the measurement of the background fluctuation from the observational data in the far-infrared range Lagache et al. 2000, Matsuhara et al. 2000. Since the resolution and the sensitivity of instruments will be improved, it is required to understand the contribution of the background fluctuation with these instruments. Based on the source

counts models, we obtain the expected Cosmic Far-Infrared Background (CFIRB).

This paper is organized as follows. In section 7.2, we briefly describes the sky confusion noise due to sky brightness fluctuations and the source confusion due to the extragalactic point sources. We explain our source count models including galaxy evolutions and the simulated images in section 7.3. Based upon the specifications of each IR mission, we estimate the source confusion noise through the fluctuation and photometric analysis in section 7.4. We present in section 7.5 the expected results from our estimation. Our conclusions are summarised in section 7.6.

Throughout this work we assume a concordance cosmology of  $H_0 = 72 \text{ km s}^{-1}\text{Mpc}^{-1}$ ,  $\Omega_m = 0.3$ , and  $\Omega_\Lambda = 0.7$ , unless otherwise explicitly stated.

## 7.2 SOURCES OF CONFUSION FOR EXTRA-GALACTIC SURVEYS

### 7.2.1 Confusion due to Infrared Cirrus

The fluctuations in the surface brightness of extended structure on similar scales as the resolution of the telescope/instrument beam can produce spurious events that can be easily mistaken for genuine point sources, since the existence of a source is usually simply derived from the difference in signal between the on source and some background position. Such extended structure is observed in wispy neutral interstellar dust in the Milky Way that is heated by the interstellar radiation field and is known as the infrared cirrus (Low et al. 1984), which is the main noise source in the far-IR range. Cirrus emission peaks at far-IR wavelengths ( $100\mu\text{m}$ ) but was detected in all 4 IRAS bands (Helou & Beichman 1990). The Galactic cirrus is a function of Galactic latitude and is serious for wavelengths longer than  $60\mu\text{m}$ . We have already discussed in detail the effects of sky confusion in Jeong et al. (2004). Here, we discuss the composite effect of sky confusion and source confusion.

### 7.2.2 Confusion due to Extragalactic Sources

The galaxy confusion limit is defined as the threshold of the fluctuations in the background sky brightness below which sources cannot be discretely detected in the telescope beam  $\sim \lambda/D$ . Thus, the fluctuation noise arises from the same origin as the galaxies that one is aiming to detect! If we assume galaxies are distributed as a power law in flux,  $S$ , down to some detection limit  $S_{\text{lim}}$ ,

$$N(> S_{\text{lim}}) = N_{\text{lim}} \left( \frac{S}{S_{\text{lim}}} \right)^{-\alpha}, \quad (7.1)$$

where  $\alpha$  is the slope of the integral source counts (where  $\alpha = 1.5$  for a Euclidean Universe) and  $N_{\text{lim}}$  is the number density at the limiting sensitivity  $S_{\text{lim}}$ . Assuming that the counts flatten at some faint flux,  $S_0$ , i.e.  $\alpha(S_0) = 0$ , then the intensity of the background (in Jy/sr) up to some maximum flux,  $S_{\text{max}}$ , corresponding to these sources is given by,

$$I = \int_{S_0}^{S_{\text{max}}} S \frac{dN}{dS} dS, \quad (7.2)$$

The fluctuations contributed by sources below the detection limit  $S_{\text{lim}}$  are given by the second moment of the differential source counts  $dN/dS$ ,  $\sigma$  in MJy/sr,

$$\sigma^2 = \int_{S_0}^{S_{\text{lim}}} S^2 \frac{dN}{dS} dS, \quad (7.3)$$

Assuming the power law distribution of sources given in equation 7.1 and 7.3 can be evaluated to give,

$$\sigma^2 = N_{\text{lim}} S_{\text{lim}}^2 \frac{\alpha}{2 - \alpha} \left[ 1 - \left( \frac{S_0}{S_{\text{lim}}} \right)^{2-\alpha} \right], \quad (7.4)$$

For the Euclidean case, the dominant sources contributing to the background intensity are those just below the detection limit  $S_{\text{lim}}$  (Matsuhara et al. 2000; Lagache et al. 2000b). However, the strong evolution detected in the galaxy population steepens the source counts and produces super Euclidean slopes in excess of  $\alpha > 1.5$  and the

sources around the detection limit also contribute significantly to the fluctuations in the background intensity.

Rigorous theoretical definitions of confusion have been presented by Scheuer (1957) and Condon (1974). Hogg (2001) has highlighted the more practical aspects of galaxy confusion noise limitations. An analytical derivation broadly following Franceschini et al. (1989) is given below. Note that the clustering of sources will complicate the confusion noise [e.g., as in the case of radio sources, Condon (1974)] although here, for clarity, we do not treat this effect [see Franceschini et al. (1989) and Takeuchi & Ishii (2004) for discussions on the effect on the confusion limit of the clustering of sources].

Assuming that the sources are distributed randomly over the sky described by a power law form  $N(S) \propto S^{-\alpha}$  and a corresponding differential distribution given by  $n(S) = kS^{-\gamma}$  where  $\gamma = \alpha - 1$ , then the detector response to a source of flux  $S$ , at a position  $(\theta, \phi)$  from the axis of a detector beam of profile (point spread function)  $f(\theta, \phi)$  is given by  $x = Sf(\theta, \phi)$ . Hence the mean number of responses with amplitudes between  $x$ ,  $x + dx$  in a solid angle  $d\Omega$  is given by;

$$R(x) = \int_{\Omega_b} \frac{n(x/f(\theta, \phi))}{f(\theta, \phi)} d\Omega, \quad (7.5)$$

where  $\Omega_b$  is the solid angle of the beam in steradians. Note that for the power law distribution of sources discussed above, equation 7.5 can be rewritten as,

$$R(x) = kx^{-\gamma} \int_{\Omega_b} f(\theta, \phi)^{\gamma-1} d\Omega = kx^{-\gamma} \Omega_e, \quad (7.6)$$

where  $\Omega_e = \int f(\theta)^{\gamma-1} d\Omega$  is the effective beam size (Condon 1974). Taking the second moment of the  $R(x)$  distribution (the variance) gives the fluctuation of the response,  $\sigma$  ;

$$\sigma^2 = \int_0^{x_c} x^2 R(x) dx, \quad (7.7)$$

where  $x_c$  is a cut off response introduced to stop the variance from diverging at bright source fluxes. More practically the confusion limit  $x_c$  (corresponding to a cut off flux  $S_c$ ) is set to some factor of the confusion noise such that  $x_c = q\sigma$ , where the

factor  $q$  limits the largest response included in the evaluation of the confusion noise  $\sigma$  [values of  $\sim 5$  are assumed in the calculations of Franceschini et al. (1991)]. The difference in assuming a cut off in the response as opposed to a cut off in flux is that weak contributions from strong sources are not neglected, as even a strong source far from the axis of the beam may contribute significantly to the point spread function of the beam.

Assuming for clarity in the calculations, a circular Gaussian beam profile,  $f(\Theta) = f((\theta/\theta_o)^2) = e^{-4(\theta/\theta_o)^2 \ln 2}$  such that  $d\Theta = 2\theta d\theta/\theta_o^2$  where  $\theta_o$  is the Full Width at Half Maximum (FWHM) of the beam, integrating equation 7.7 over the solid angle of the beam gives;

$$\sigma_c^2(x_c) = \pi\theta_o^2 P(x_c) \quad (7.8)$$

or

$$\theta_o = \sqrt{\frac{\sigma_c^2}{\pi P(x_c)}}, \quad (7.9)$$

where  $P$ , effectively the power in the fluctuations, is given by,

$$P(x_c) = \int_0^{x_c} x^2 dx n(x/f(\Theta)) e^{4\Theta \ln 2} d\Theta, \quad (7.10)$$

Thus the confusion limit can be directly related to the FWHM of the instrument beam. For the simple power law representation of the distribution of extragalactic sources given previously and the definitions of equations 7.5 and 7.6, the confusion limit is given by,

$$\sigma_c = \sqrt{\frac{k\Omega_e}{3-\gamma}} x_c^{(3-\gamma)/2}, \quad (7.11)$$

Therefore, the confusion noise limit will be a complex function of the beam size  $\theta_o$ , the source counts  $N(S)$ , the cut off in flux  $S_c$  or response  $x_c$  and the factor  $q$ . For the assumed symmetric Gaussian beam profile,  $\sigma_c \propto \theta_o^{2/(\gamma-1)}$ .

Note that the beam size  $\theta$  (or FWHM,  $\theta_o$ )  $\propto \lambda/D$  where  $\lambda$  is the observation wavelength and  $D$  is the telescope diameter. Therefore, the confusion due to faint

galaxies will be worse at longer wavelengths and smaller telescope diameters. Since the confusion noise is related to the mean number of responses (the source density) and the cut off response  $q/x_c$ , a useful, practical benchmark for the confusion limit can be set by limiting the number sources per beam before the beam becomes confused. Ideally, the confusion limit would be determined by the flux at which the source density becomes 1 source per beam although more realistically a limit of between 1/20-1/50 sources per beam (20-50 beams per source) is assumed [e.g., Hogg (2001)].

### 7.3 THE INPUT CATALOGUES AND SIMULATED IMAGES

The input catalogues are prepared using the models of Pearson (2001) (hereafter CPP). CPP is an infrared model based on the IRAS colours and luminosity function of galaxies [see also Pearson & Rowan-Robinson (1996)]. The model incorporates a 4 component parameterization of galaxy SEDs segregated by IRAS colours (Rowan-Robinson & Crawford 1989). A normal galaxy population modelled on the cool 100  $\mu\text{m}/60 \mu\text{m}$  colours identified with infrared cirrus (Low et al. 1984; Efstathiou & Rowan-Robinson 2002). A starburst population based upon the warm 100  $\mu\text{m}/60 \mu\text{m}$  colours of IRAS galaxies with the archetypical starburst galaxy M82 as a template SED (Efstathiou, Rowan-Robinson & Siebenmorgen 2000). An ultraluminous galaxy population (Sanders & Mirabel 1996) representing the high luminosity tail of the IRAS starburst galaxy population and representative of the archetypical ULIG ARP220 (Efstathiou, Rowan-Robinson & Siebenmorgen 2000). An AGN (Seyfert 1 & Seyfert 2) population modelled on a 3-30 $\mu\text{m}$  dust torus component (Rowan-Robinson 1995) defined by hot 25  $\mu\text{m}/60 \mu\text{m}$  colours. The input spectral energy distributions are shown in figure 7.1.

To produce the input source distributions, we calculate the total number of sources per steradian at observation wavelength,  $\lambda_o$ , down to some flux limit  $S_{\lambda_o}$ ;

$$N(S_{\lambda_o}) = \int_0^\infty \int_0^{z(L,S)} \phi(L/f(z)) \frac{dV(z)}{dz} e(z) d \lg L dz, \quad (7.12)$$

where  $f(z)$  &  $g(z)$  are evolutionary factors as described by equations 7.19 & 7.20

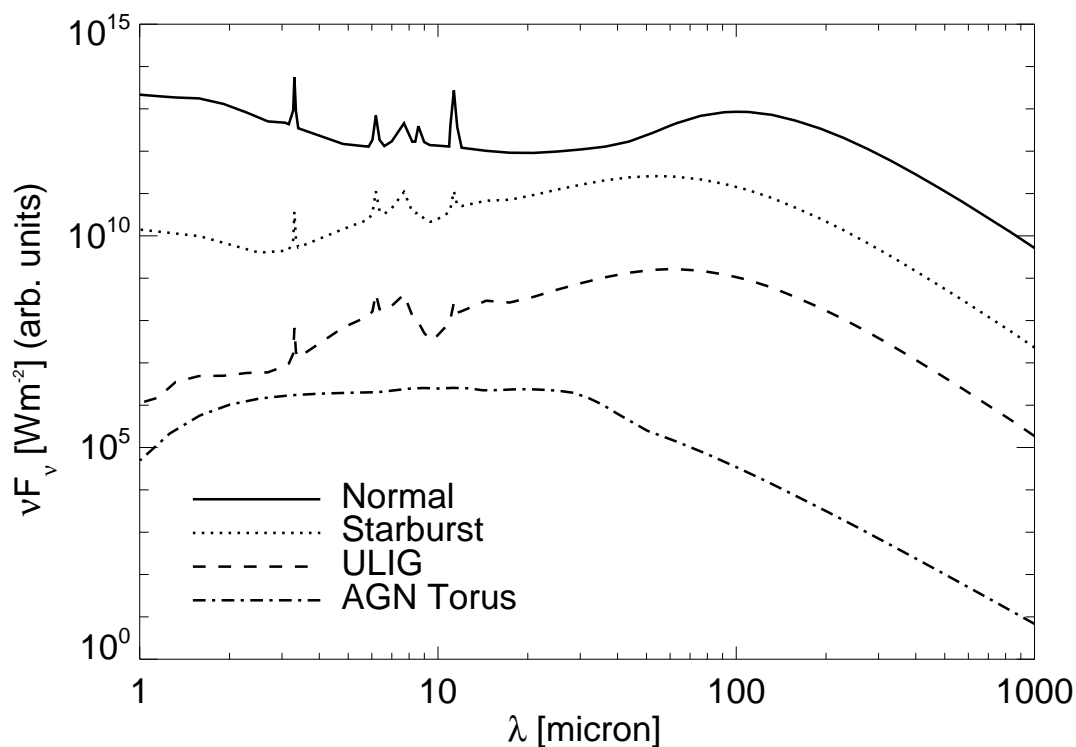


FIG. 7.1: Model input spectral energy distributions used for input catalogues to the simulation. A four component model comprising of a normal galaxy, starburst galaxy, ultraluminous galaxy and AGN dust torus are included. The source spectral energy distributions are based on the models of Efstathiou et al. (2001), Efstathiou & Rowan-Robinson (2002), Rowan-Robinson (1995).

and 7.21 & 7.22 respectively. The integration is made over the luminosity function (number density of objects as a function of luminosity),  $\phi(L)$  and the cosmological volume  $V$ , enclosed inside a limiting redshift  $z(L, S)$  defined as the redshift at which a source of luminosity,  $L$ , falls below the sensitivity,  $S(\lambda_o)$  of a given observation, where  $S(\lambda_o)$  is given by;

$$S(\lambda_o) = \frac{d\lambda_e}{d\lambda_o} \frac{L_{\lambda_e}}{4\pi D_L^2} = \frac{L_{\lambda_o}}{4\pi D_L^2} \frac{\lambda_e L_{\lambda_e}}{\lambda_o L_{\lambda_o}} f(z), \quad (7.13)$$

where the suffix *o* & *e* correspond to the observation frame and emission rest frame respectively and  $D_L$  is the luminosity distance in a flat, vacuum energy dominated universe ( $\Omega_m = 0.3, \Omega_\Lambda = 0.7$ ) given by;

$$D_L(z) = \left( \frac{c}{H_o} \right) \int_0^z \frac{(1+z)}{\sqrt{(1+z)^2(1+\Omega_m z) - z(2+z)\Omega_\Lambda}}, \quad (7.14)$$

corresponding to differential volume per steradian required in equation 7.12 of;

$$\frac{dV(z)}{dz} = \left( \frac{c}{H_o} \right) \frac{(1+z)^{-2} D_L^2}{\sqrt{(1+z)^2(1+\Omega_m z) - z(2+z)\Omega_\Lambda}}, \quad (7.15)$$

Luminosity functions are determined from the IRAS PSCz catalogue at  $60\mu\text{m}$  (equation 7.16) (Saunders et al. 2000). Saunders (1990) subdivided the luminosity function of IRAS galaxies into *warm* and *cool* components following colour criteria akin to those of Rowan-Robinson & Crawford (1989). Similarly, the *hot* AGN population is well represented by the  $12\mu\text{m}$  sample of Rush et al. (1993) using the luminosity function of Lawrence et al. (1986) (equation 7.17). Finally we introduce an log exponential luminosity function, defined at  $60\mu\text{m}$ , to represent the ULIG population (equation 7.18, referred to as the Burst model) modelled by CPP which was originally implemented to address the paradigms of the strong evolution in the galaxy source counts observed with the Infrared Space Observatory (ISO) in the mid-far infrared, at sub-mm wavelengths with SCUBA and the detection of the CIRB at  $\sim 170\mu\text{m}$  (Oliver et al. 1997; Smail, Ivison & Blain 1997; Kawara et al. 1998; Hughes et al. 1998; Flores et al. 1999; Altieri et al. 1999; Aussel et al. 1999; Gruppioni et al. 1999; Puget et al. 1999; Efstathiou et al. 2000b; Biviano et al. 2000; Elbaz et al. 2000; Serjeant et al. 2000;

Lagache et al. 2000a; Matsuhara et al. 2000; Scott et al. 2002). This model was found to provide a good fit to both the number counts and redshift distributions of galaxies from sub-mm to near infrared wavelengths as well as the cosmic infrared background.

$$\phi(PSCz(L_{60})) = \frac{d\Phi}{dL} = \phi^* \left( \frac{L}{L^*} \right)^{1-\alpha} \exp \left[ -\frac{1}{2\sigma^2} \lg^2 \left( 1 + \frac{L}{L^*} \right) \right] \quad (7.16)$$

$$\phi(AGN(L_{12})) = \frac{d\Phi}{dL} = \phi^* L^{1-\alpha} \left( 1 + \frac{L}{L^* \beta} \right)^{-\beta} \quad (7.17)$$

$$\phi(Burst(L_{60})) = \frac{d\Phi}{dL} = \phi^* \exp \left[ -\frac{1}{2\sigma^2} \lg^2 \left( \frac{L}{L^*} \right) \right] \quad (7.18)$$

To shift the luminosity function from the wavelength at which the luminosity function is defined,  $\lambda_{LF}$ , to the observation wavelength,  $\lambda_{obs}$ , the ratio  $L(\lambda_{obs})/L(\lambda_{LF})$  is obtained via the model template spectra.

We assume that the populations may evolve in both luminosity (luminosity evolution) and number density (density evolution) and parameterize these as two functions  $f(z)$  and  $e(z)$  respectively (see equations 7.12 and 7.13). Furthermore, we characterize two flavours of evolution. A power law parameterization similar to the models of Pearson & Rowan-Robinson (1996) given by;

$$f(z) = (1 + z)^k \quad (7.19)$$

$$e(z) = (1 + z)^g \quad (7.20)$$

or an exponential parameterization (i.e. as introduced in CPP) given by

$$f(z) = 1 + k \exp \left[ -\frac{(z - z_p)^2}{2\omega^2} \right], \quad (7.21)$$

$$e(z) = 1 + g \exp \left[ -\frac{(z - z_p)^2}{2\omega^2} \right], \quad (7.22)$$

where  $k$ ,  $g$ , and  $\omega$  are parameters determined by the best fit to observations and  $z_p$  is some peak redshift in the evolution.

We prepare 3 types of input catalogues and produce many versions of each to reduce statistical errors.

1. *No-Evolution Model* - No evolution is assumed for any galaxy component.
2. *Luminosity Evolution Model* - Luminosity evolution is included following Pearson & Rowan-Robinson (1996).
3. *Burst Evolution Model* - Luminosity and density evolution is included following the CPP model.

Tables 7.1, 7.2 and 7.3 summarizes the information for each of the input catalogues and evolutionary models listed above respectively.

Based upon these input catalogues, we generated the simulated images in each band of various space missions. The image size for distributed source simulation is 2.3 square degree. In order to check the effect of sky confusion noise, we include the high resolution cirrus map by using the method described in Jeong et al. (2004).

## 7.4 SIMULATION RESULTS FOR CONFUSION

As we described in section 7.2, there are many definitions for the source confusion. We compare between these definitions and propose an appropriate definition for source confusion.

### 7.4.1 Definition by ‘Beams per Source’

First, we estimate the classical definition of source confusion, beams per source. We check the source confusion by changing beams per source from 20 to 50. The estimated source confusion varies within a factor of  $\sim 2$ . In table 7.4, we list the source confusion estimated with a definition of 40 per source for each evolution model and mission. Hogg (2001) showed that 30 beams per source is the minimum photometric criterion where source counts is steep, and suggested 50 beams per source in the definition of source confusion. Rowan-Robinson (2001) adopted 40 beams per source.

TABLE 7.1: Parameters for the No Evolution Model

1	Type	Normal	Starburst	ULIG	Seyfert 1	Seyfert 2
Luminosity Functions						
2	LF	PSCz	PSCz	PSCz	AGN	AGN
3	Lmin	8	8	11.5	8	8
4	Lmax	11.5	11.5	14	14	14
5	L*	9.62	9.99	9.99	9.552	9.952
6	$\alpha$	1.15	1.27	1.27	1	1
7	$\sigma$	0.463	0.626	0.626	—	—
8	$\beta$	—	—	—	2.1	2.5
Luminosity Evolution						
9	$z_p$	-	-	-	-	-
10	$f(z) < z_p$	-	-	-	-	-
11	$k$	-	-	-	-	-
12	$\omega$	-	-	-	-	-
13	$f(z) > z_p$	-	-	-	-	-
14	$k$	-	-	-	-	-
15	$\omega$	-	-	-	-	-
Density Evolution						
16	$z_p$	-	-	-	-	-
17	$e(z) < z_p$	-	-	-	-	-
18	$g$	-	-	-	-	-
19	$\omega$	-	-	-	-	-
20	$e(z) > z_p$	-	-	-	-	-
21	$g$	-	-	-	-	-
22	$\omega$	-	-	-	-	-

1: Galaxy SED type.

2: Luminosity function type.

3: Lower limit to population luminosity ( $L_\lambda/L_\odot$ ).

4: Upper limit to population luminosity ( $L_\lambda/L_\odot$ ).

5: Luminosity function ( $L^* = L_\lambda/L_\odot$ ).

6,7,8: Luminosity function parameters.

9: Peak redshift for luminosity evolution.

10: Form of luminosity evolution for  $z < z_p$ , pow=power law, exp=exponential, c=constant.

11,12: Luminosity evolution parameters.

13: Form of luminosity evolution for  $z > z_p$ , pow=power law, exp=exponential, c=constant.

14,15: Luminosity evolution parameters.

16: Peak redshift for density evolution.

17: Form of density evolution for  $z < z_p$ , pow=power law, exp=exponential, c=constant.

18,19: Density evolution parameters.

20: Form of density evolution for  $z > z_p$ , pow=power law, exp=exponential, c=constant.

21,22: Density evolution parameters.

TABLE 7.2: Parameters for the Luminosity Evolution Model

1	Type	Normal	Starburst	ULIG	Seyfert 1	Seyfert 2
Luminosity Functions						
2	LF	PSCz	PSCz	PSCz	AGN	AGN
3	Lmin	8	8	11.5	8	8
4	Lmax	11.5	11.5	14	14	14
5	L*	9.62	9.99	9.99	9.552	9.952
6	$\alpha$	1.15	1.27	1.27	1	1
7	$\sigma$	0.463	0.626	0.626	—	—
8	$\beta$	—	—	—	2.1	2.5
Luminosity Evolution						
9	$z_p$	-	2.5	2.5	2.5	2.5
10	$f(z) < z_p$	-	pow	pow	pow	pow
11	$k$	-	3.1	3.1	3.1	3.1
12	$\omega$	-	-	-	-	-
13	$f(z) > z_p$	-	$c = f(z_p)$	$c = f(z_p)$	$c = f(z_p)$	$c = f(z_p)$
14	$k$	-	3.1	3.1	3.1	3.1
15	$\omega$	-	-	-	-	-
Density Evolution						
16	$z_p$	-	-	-	-	-
17	$e(z) < z_p$	-	-	-	-	-
18	$g$	-	-	-	-	-
19	$\omega$	-	-	-	-	-
20	$e(z) > z_p$	-	-	-	-	-
21	$g$	-	-	-	-	-
22	$\omega$	-	-	-	-	-

See table 7.1 for explanation of columns.

TABLE 7.3: Parameters for the Burst Evolution Model

1	Type	Normal	Starburst	ULIG	Seyfert 1	Seyfert 2
Luminosity Functions						
2	LF	PSCz	PSCz	Burst	PSCz	AGN
3	Lmin	8	8	11.4	11.6	8
4	Lmax	11.5	11.5	11.6	14	14
5	L*	9.62	9.99	11.6	9.99	9.552
6	$\alpha$	1.15	1.27	—	1.27	1
7	$\sigma$	0.463	0.626	0.1	0.626	—
8	$\beta$	—	—	—	—	2.1
Luminosity Evolution						
9	$z_p$	-	2.5	2.5	2.5	2.5
10	$f(z) < z_p$	-	pow	exp	pow	pow
11	$k$	-	3.1	40	3.1	3.1
12	$\omega$	-	-	0.58	-	-
13	$f(z) > z_p$	-	exp	exp	exp	exp
14	$k$	-	1	40	1	1
15	$\omega$	-	10	5	10	10
Density Evolution						
16	$z_p$	2	-	0.8	-	-
17	$e(z) < z_p$	-	-	exp	-	-
18	$g$	-	-	250	-	-
19	$\omega$	-	-	0.2	-	-
20	$e(z) > z_p$	exp	-	exp	-	-
21	$g$	1	-	250	-	-
22	$\omega$	0.2	-	0.32	-	-

See table 7.1 for explanation of columns.

TABLE 7.4: Source confusion estimated by the definition of 40 beams per source.

Space Mission	No evolution		Luminosity evolution		Burst evolution	
	(mJy)		(mJy)		(mJy)	
	SW	LW	SW	LW	SW	LW
Spitzer	1.0	16	3.1	24	10	57
ASTRO-F <sup>a</sup>	4.0	24	7.9	33	21	71
Herschel & SPICA	0.027	1.5	0.26	4.6	0.35	15

<sup>a</sup> Wide-S band for SW and Wide-L band for LW.

## 7.4.2 Definition by Fluctuation

A second criterion for the source confusion can be defined by the fluctuation from beam to beam due to the point sources. Since the beam size is large while the source counts are steep, the usual definition by 'beams per source' may not be valid in far-IR photometry. Numerous authors (Condon 1974; Franceschini et al. 1989, 1991; Hacking & Soifer 1991; Vaisanen et al. 2001; Xu et al. 2001) have used the fluctuation due to unresolved faint sources in the definition of source confusion. As we described in section 7.2.2, source confusion is obtained from the iteration procedure until  $q$  parameter satisfy the condition  $q = S_c/\sigma(S_c)$ , where  $q$  is usually chosen with the values between 3 and 5. To see the iteration procedure, we plot  $S_c/\sigma(S_c)$  ratio as a function of  $S_c$  for Spitzer and Herschel & SPICA missions (see figure 7.2). For the SW band of Herschel & SPCIA mission,  $S_c/\sigma$  ratio is always greater than 5, which means that we can not obtain the well-defined solution for source confusion, even  $q = 5$  chosen.

In table 7.5, we list the source confusion estimated from the definition by fluctuation for the case of  $q = 5$ . If we choose the constant  $q = 5$  in the estimation of source confusion, there are no source confusion in SW band of Herschel & SPICA mission. However, when we try photometry on the simulated image including the point sources

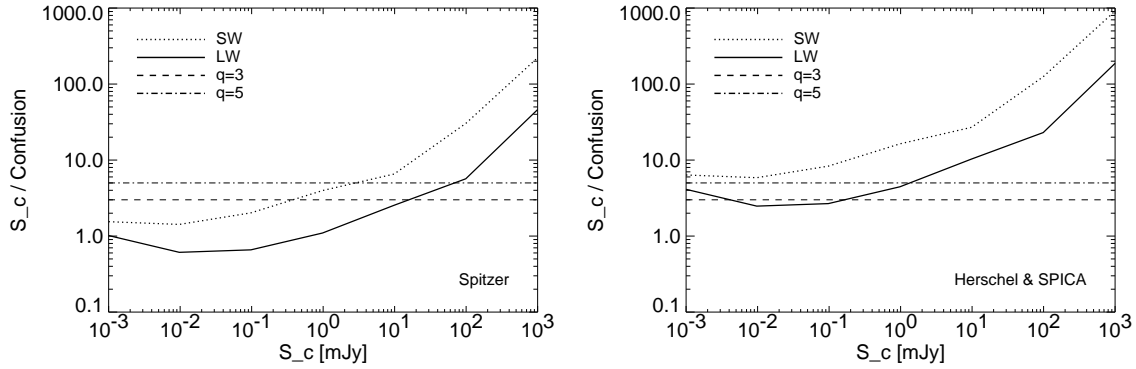


FIG. 7.2:  $S_c/\sigma$  ratio as a function of  $S_c$  for Spitzer (left) and Herschel & SPICA (right) missions. We also plot  $S_c/\sigma = 3$  (dashed line) and 5 (dashed dotted line). In the case of Herschel & SPICA mission in SW band,  $S_c/\sigma$  is always greater than 3.

following each source count model, there should be some limits in the source detection. Therefore, we conclude that we can not apply the constant  $q$  to the estimation of source confusion.

### 7.4.3 Definition by Composition of Fluctuation and Photometry

We generated the simulated image following each source count model. On these images, we try photometry in order to find the appropriate source confusion limits. It is not easy to define the source confusion from the simulated data. Since the detection becomes increasingly difficult for sources below some source confusion limits, we first define the detection limits reflecting the source confusion. The definition of completeness and reliability are widely used in the photometry. The ‘completeness’ is a fraction of detected sources to original input catalogue sources and the ‘reliability’ is a fraction of real sources to all detected sources (real and spurious). An excess of sources near the detection limit, or more likely an overestimation of the flux of sources at or near the detection limit may be caused by a step effect where the underlying, unresolved sources

TABLE 7.5: Source confusion estimated by the definition of fluctuation.

Space Mission	No evolution		Luminosity evolution		Burst evolution	
	(mJy)		(mJy)		(mJy)	
	SW	LW	SW	LW	SW	LW
Spitzer	0.21	9.3	1.6	28	3.0	70
ASTRO-F	2.0	21	9.5	51	23	121
Herschel & SPICA	...	0.28	...	1.2	...	1.4

are entering the PSF and effecting the sky-subtraction. In the case of the 'reliability' definition, we assume that the flux of the correctly detected source is the measured flux from the photometry, and agrees with the input flux within a 20% error as well. We carried out aperture photometry on the simulated images using the SExtractor software *v2.0.0* (Bertin & Arnouts 1996). The most influential parameters are the size of background mesh and the threshold for the source detection in this aperture photometry. We set the size of the background mesh to 2.5 times of the measuring aperture, and the detection threshold as 4, which is optimized for better reliability of the detected sources and reducing false detection rate.

As we discussed in section 7.4.2, we can not use the constant  $q$  in the estimation of source confusion. In the current or incoming space missions, we will detect much fainter sources with high sensitivity. Therefore, we expect that we can observe the high source density even in faint detectable flux range. In this situation, the significant contribution factor to the source detection can be both the faint sources below the detection limit and the high source density above the detection limit. With this assumption, we estimate the fluctuation considering the contribution from the sources above the detection limit as well. We set the limiting flux  $S_c$  to be the flux that both the completeness and the reliability reach 90% by the photometric criterion. We can assume that the sources above this flux level never affect the source confusion. We obtain the final source confusion from 4 fluctuation in order to coincide with the

TABLE 7.6: Source confusion estimated by the definition of the composition of fluctuation and photometry.

Space Mission	No evolution		Luminosity evolution		Burst evolution	
	(mJy)		(mJy)		(mJy)	
	SW	LW	SW	LW	SW	LW
Spitzer	2.1	19	3.8	38	10	67
ASTRO-F	4.1	23	11	48	25	105
Herschel & SPICA	0.035	1.5	0.21	4.2	0.58	10

threshold used in the photometry. In table 7.6, we list the source confusion estimated by our best estimator.

Though we can not obtain the results for SW band of Herschel & SPICA mission with the definition of the fluctuation with constant  $q$ , we can obtain the results by our best estimator, which are similar with the definition of ‘beams per source’. We also find that the source confusion by our definition is usually consistent with the completeness of 75%  $\sim$  80% for all missions. Therefore, we conclude that our definition can explain the behaviour of source confusion well, regardless of the mission.

#### 7.4.4 Predicted Confusion Limits for Current and Future Missions

Applying the estimation method of sky confusion by Jeong et al. (2004), we list the results of sky confusion for assumed range of average brightness  $\langle B_\lambda \rangle$  in table 7.7.

For comparison with the source confusion, we list the ratio of source confusion for each model to the sky confusion for each mission in table 7.8 – 7.10. From table 7.8 – 7.10, it is clear that sky confusion should be ignorable problem for Herschel & SPICA mission, however care must be exercised when considering Spitzer & ASTRO-F mission in the mean brightness  $\langle B_\lambda \rangle \gtrsim 15$  MJy/sr and the case for no evolution model. For

TABLE 7.7: Estimated confusion limits due to Galactic cirrus for each mission.

Space Mission	Sky Confusion Limits (mJy) for $\langle B_\lambda \rangle$					
	0.5 MJy/sr		5 MJy/sr		15 MJy/sr	
	SW	LW	SW	LW	SW	LW
Spitzer	0.08	3.2	1.0	8.2	3.0	22
ASTRO-F	0.5	9.2	2.3	13	9.5	32
Herschel & SPICA	0.002	0.1	0.02	0.16	0.08	0.22

TABLE 7.8: Ratio of source confusion to sky confusion for no evolution model.

Space Mission	Ratio of source confusion to sky confusion					
	0.5 MJy/sr		5 MJy/sr		15 MJy/sr	
	SW	LW	SW	LW	SW	LW
Spitzer	26	5.9	2.0	2.3	0.68	0.86
ASTRO-F	8.2	2.5	1.8	1.8	0.43	0.72
Herschel & SPICA	18	15	1.75	9.4	0.44	6.8

a cosmological study, i.e., the observation of the high Galactic latitude region, we can only consider the source confusion irrespective of the source count model.

Although the sky confusion noise itself is not a dominant noise source in the high resolution mission, the structure of the cirrus make us distinguish the background fluctuations by the unresolved sources below the confusion limit through the comparative study of the power spectrum. In addition, we can discriminate the evolution scenario through both this fluctuation analysis and the source count results.

TABLE 7.9: Ratio of source confusion to sky confusion for luminosity evolution model.

Space Mission	Ratio of source confusion to sky confusion					
	0.5 MJy/sr		5 MJy/sr		15 MJy/sr	
	SW	LW	SW	LW	SW	LW
Spitzer	48	12	3.8	4.6	1.3	1.7
ASTRO-F	21	5.2	4.6	3.7	1.1	1.5
Herschel & SPICA	105	42	11	26	2.6	19

TABLE 7.10: Ratio of source confusion to sky confusion for burst evolution model.

Space Mission	Ratio of source confusion to sky confusion					
	0.5 MJy/sr		5 MJy/sr		15 MJy/sr	
	SW	LW	SW	LW	SW	LW
Spitzer	125	21	10	8.2	3.3	3.0
ASTRO-F	50	11	11	8.0	2.6	3.3
Herschel & SPICA	290	100	29	63	7.3	45

TABLE 7.11: Final confusion limit considering both source confusion and sky confusion.

Space Mission	Sensitivity <sup>a</sup>		No evolution		Luminosity evolution		Burst evolution	
	(mJy)		(mJy)		(mJy)		(mJy)	
	SW	LW	SW	LW	SW	LW	SW	LW
Spitzer	6	15	2.1	19	3.8	38	10	67
ASTRO-F	14	23	4.1	25	11	49	25	105
Herschel & SPICA	3	3	0.035	1.5	0.21	4.2	0.58	10

<sup>a</sup>  $5\sigma$  sensitivity without source confusion and sky confusion. In the case of the Herschel & SPICA mission, we commonly use the  $5\sigma$  sensitivity of Herschel mission (Poglitsch et al. 2003).

## 7.5 EXPECTED RESULTS

### 7.5.1 Expected Redshift Distribution

We summarize the confusion limits including both source confusion and sky confusion for each mission in table 7.11, though confusion is dominated by the source confusion. The mean brightness for estimation of sky confusion is 0.5 MJy/sr and 1.0 MJy/sr for SW and LW bands, respectively.

Once the detection limits are determined, we can obtain the expected redshift distribution for each model. The number-redshift distribution at limiting flux  $S_c$ , can be obtained from the integration of the evolving luminosity function and is given by:

$$\frac{dN_\nu(S_c, z)}{dz} = \int d \log L \int_{\circ}^{z(L, S_c, \nu)} \phi(L, z) \frac{dV}{dz}. \quad (7.23)$$

In figure 7.3 – 7.5, we show the expected redshift distributions for each mission. Since the outstanding number of sources below  $z < 1.0$  is detected in LW bands for no evolution model, the redshift distribution for each mission have significant difference

whether there is the evolution or not. However, in order to distinguish between two evolution scenario distinctly, higher sensitivity mission (e.g., Spitzer, Herschel and SPICA) have more advantage over the low resolution mission (e.g., ASTRO-F).

### 7.5.2 Expected Cosmic Far-Infrared Background

One of the outstanding challenges in modern cosmology is to explain the formation of structure in the universe. The cosmic infrared background records much of the radiant energy released by processes of structure formation that have occurred since the decoupling of matter and radiation following the Bing Bang. In the past study from infrared missions, the measurements of this background are carried out. At the same time, there has been a rapid progress in resolving a significant fraction of this background with the deep galaxy counts at infrared wavelengths.

The flux levels of extragalactic sources below the detection limits create the fluctuation in the background. The Cosmic Far-Infrared Background (CFIRB) intensity  $I_{\text{CFIRB}}$  produced by all sources with the flux below maximum flux  $S_{\text{max}}$ , is obtained from:

$$I_{\text{CFIRB}} = \int_0^{S_{\text{max}}} S \frac{dN}{dS} dS. \quad (7.24)$$

In addition, the CFIRB fluctuations  $P_{\text{CFIRB}}$  from sources with the uniform distribution below the a given detection limit  $S_c$  can be estimated by the power spectrum,

$$P_{\text{CFIRB}} = \int_0^{S_c} S^2 \frac{dN}{dS} dS. \quad (7.25)$$

The detection limit  $S_c$  is already obtained in table 7.11. In table 7.12 – 7.13, we show the expected CFIRB intensity and CFIRB fluctuation, respectively.

Lagache, Dole & Puget proposed that Spitzer mission can resolve  $\sim 20\%$  of the CFIRB at  $160 \mu\text{m}$  on their source count model. According to our estimation with our source count model, we can resolve  $\sim 15\%$  and  $\sim 22\%$  of the CFIRB for burst evolution model and luminosity evolution model, respectively. ASTRO-F mission can reach the resolving level of  $\sim 9\%$  and  $\sim 17\%$  of the CFIRB for two evolution models. We also expect that more than  $87\%$  and  $65\%$  of the CFIRB at  $70 \mu\text{m}$  and  $160 \mu\text{m}$

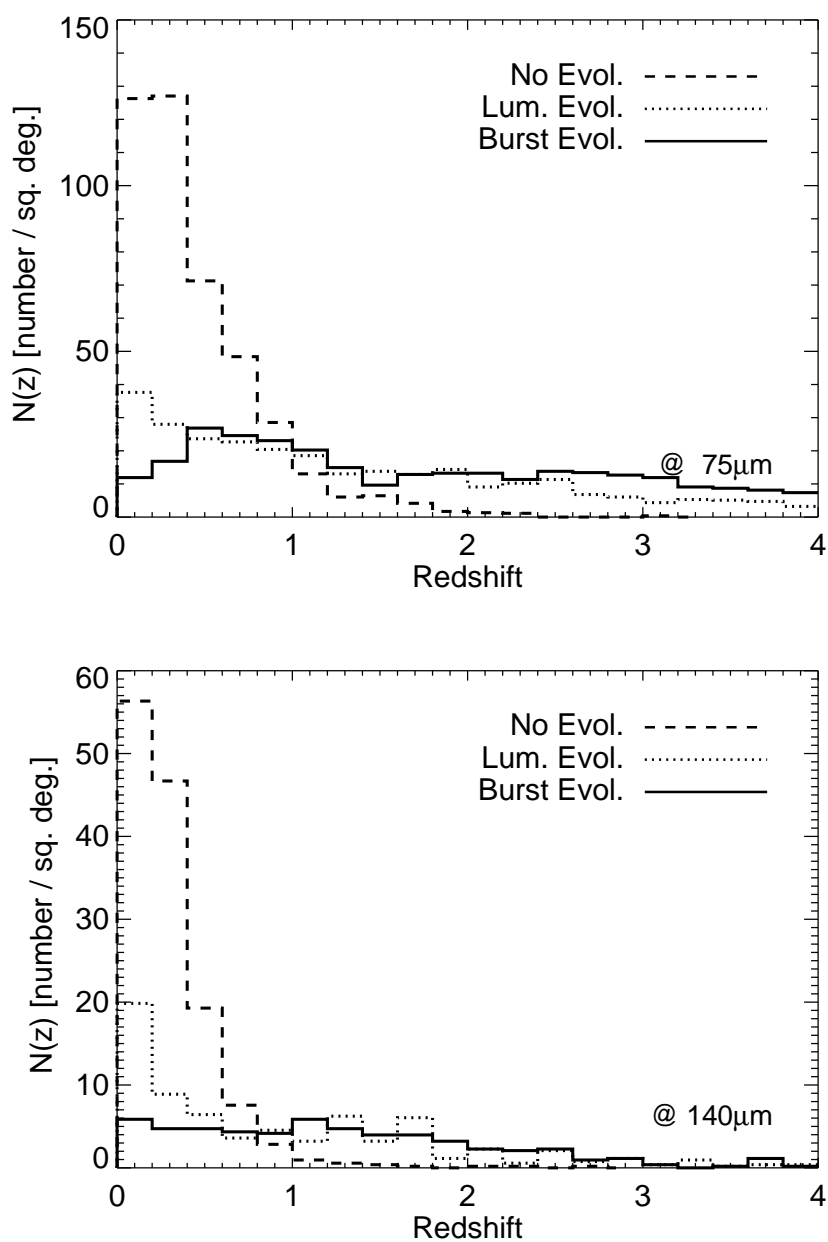


FIG. 7.3: Expected redshift distribution for ASTRO-F mission.

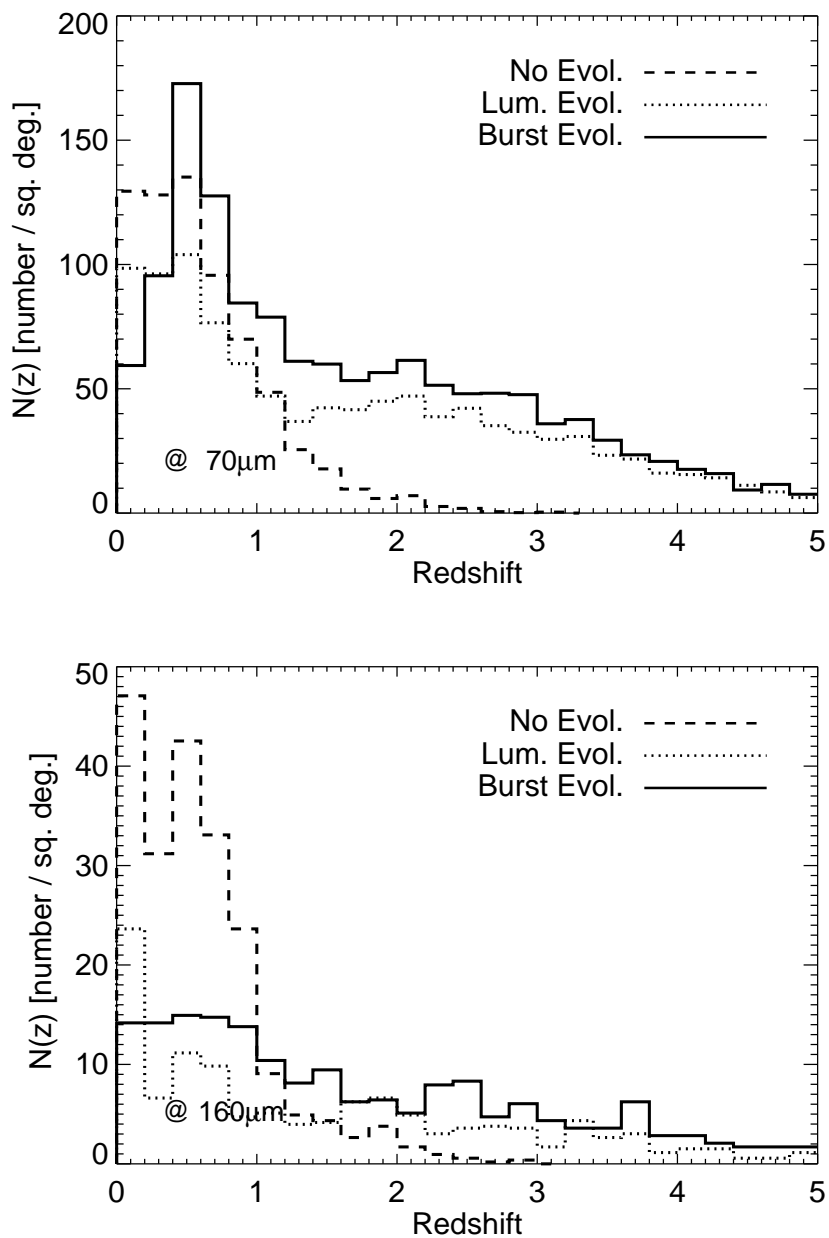


FIG. 7.4: Expected redshift distribution for Spitzer mission.

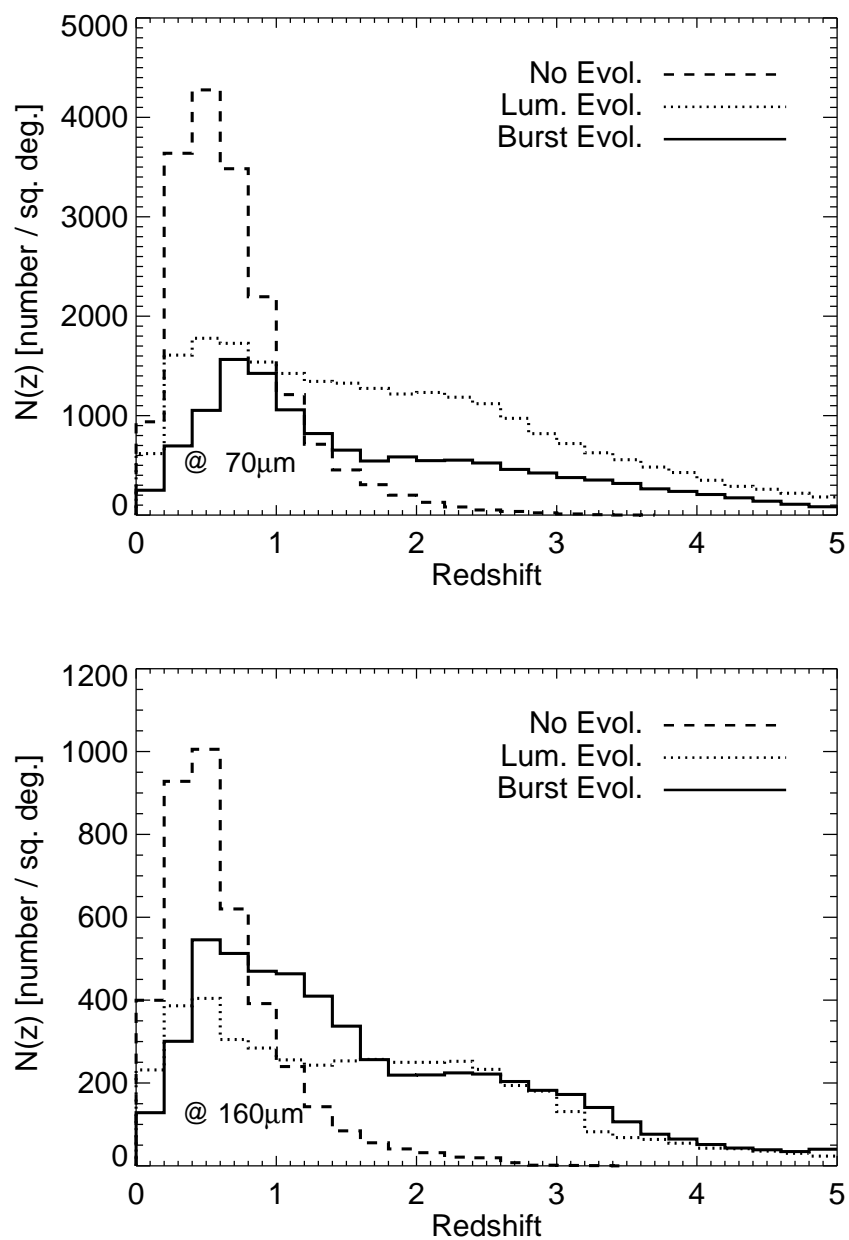


FIG. 7.5: Expected redshift distribution for Herschel &amp; SPICA mission.

TABLE 7.12: Expected CFIRB intensity for each mission. The upper flux is set to be the final confusion limits.

Space Mission	Luminosity evolution		Burst evolution	
	(MJy/sr)		(MJy/sr)	
	SW	LW	SW	LW
Spitzer	0.07	0.31	0.17	0.61
ASTRO-F	0.11	0.33	0.20	0.65
Herschel & SPICA	0.065	0.18	0.038	0.28

respectively will be resolved by the Herschel & SPICA mission due to much higher sensitivity compared with that of ASTRO-F and Spitzer missions.

In the far-IR range, Lagache & Puget (2000) and Matsuhara et al. (2000) have studied the detection of the CFIRB fluctuation in Marano 1 region and Lockman Hole, respectively. For comparison, we list estimated fluctuation on our model in table 7.14. The predicted fluctuation shows more consistent results with the fluctuation from the burst evolution model. The power spectrum of cirrus emission in the high Galactic latitude ( $> 60$  degree) have the fluctuation  $10^6$  Jy<sup>2</sup>/sr at  $0.01$  arcmin<sup>-1</sup> and the power index of  $-2.9 \pm 0.5$ . In order to segregate the CFIRB fluctuation from the estimated power spectrum including features of the cirrus emission effectively, we need the area larger than  $10^2$ ,  $11^2$ ,  $4.5^2$  square arcmin for Spitzer, ASTRO-F, Herschel & SPICA mission, respectively in the case of burst evolution model (see figure 7.6).

## 7.6 CONCLUSIONS

In order to probe the confusion, we generated the source catalogue assuming a concordance (i.e. flat, dark energy dominated) cosmological world model ( $H_o = 72$ ,  $\Omega = 0.3$ ,  $\Lambda = 0.7$ ) for 2 evolutionary scenarios defined as the luminosity evolution models and burst models of Pearson (2001) and Pearson et al. (2001), respectively. We also consid-

TABLE 7.13: Expected CFIRB fluctuations for each mission.

Space Mission	Luminosity evolution		Burst evolution	
	(Jy <sup>2</sup> /sr)		(Jy <sup>2</sup> /sr)	
	SW	LW	SW	LW
Spitzer	62	1600	650	9200
ASTRO-F	205	2000	1060	~12000
Herschel & SPICA	1.8	220	8	900

TABLE 7.14: Comparison of CFIRB fluctuations.

$\lambda$	$\theta$	$S_{\max}$	$P_{\text{CFIRB}}$	Predicted $P_{\text{CFIRB}}$ <sup>a</sup>
( $\mu\text{m}$ )	(arcmin)	(mJy)	(Jy <sup>2</sup> /sr)	(Jy <sup>2</sup> /sr)
90	0.4 – 20	150	13000 $\pm$ 3000	2500 – 6000
170	0.6 – 4	100	7400	4000 – 11000
170	0.6 – 20	250	12000 $\pm$ 2000	5000 – 18000

<sup>a</sup> Lower value is estimated from luminosity evolution model and upper value from burst evolution model.

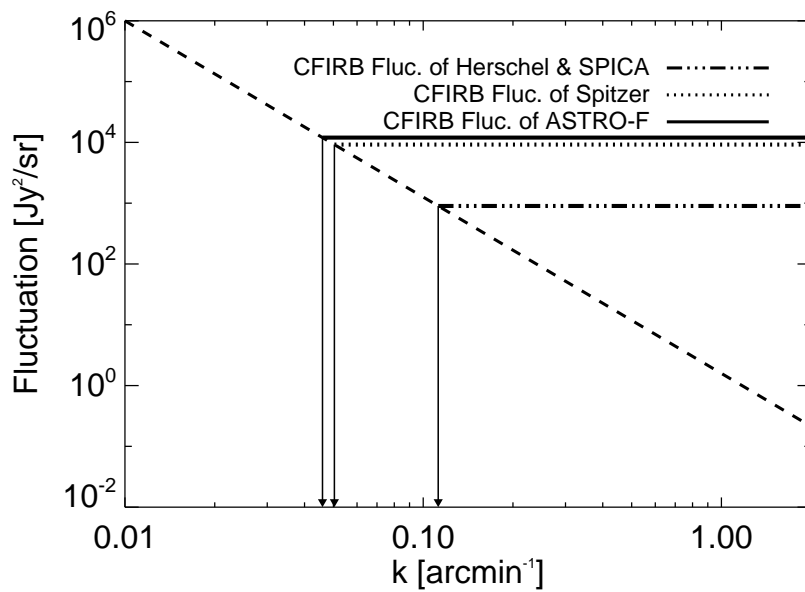


FIG. 7.6: Expected CFIRB fluctuation for each mission and burst evolution model. The corresponding spatial scale is 20, 22, 9 arcmin for Spitzer, ASTRO-F and Herschel & SPICA missions, respectively.

ered the sky confusion due to the cirrus. Though the sky confusion is not a dominant noise source at high Galactic latitude, we should take into account the effects of sky confusion for large area survey. In addition, in order to obtain the CFIRB fluctuations, we need to analyze the fluctuation of cirrus emission even in high Galactic latitude regions.

Based upon the fluctuation and the photometry on the simulated images, we found the best estimator for source confusion. From our analysis of source confusion, we obtained source confusion limits of 10 mJy and 67 mJy at 70  $\mu\text{m}$  and 160  $\mu\text{m}$  for Spitzer mission, 25 mJy and 105 mJy at 75  $\mu\text{m}$  and 140  $\mu\text{m}$  for ASTRO-F mission, and 0.58 mJy and 10 mJy at 70  $\mu\text{m}$  and 160  $\mu\text{m}$  for Herschel & SPICA mission. If the source distribution follows the evolution models, the planned and current infrared missions is mostly limited by source confusion. We also obtain the expected redshift distribution for each source count model. The redshift distribution for each mission have significant difference between no evolution model and evolution models. However, in order to distinguish between two evolution scenario distinctly, higher sensitivity mission (e.g., Herschel and SPICA) have more advantage over relatively low resolution mission (e.g., ASTRO-F). From the study for the CFIRB, we found that CFIRB can be resolved 87% and 65% at 70  $\mu\text{m}$  and 160  $\mu\text{m}$  by next generation infrared mission Herschel & SPICA which are corresponding to the CFIRB intensity of 0.038 MJy/sr and 0.28 MJy/sr for the burst evolution model.

---

W.-S. Jeong was financially supported by the BK21 Project of the Korean Government. This work was financially supported in part by the KOSEF Grant R14-2002-058-01000-0. Chris Pearson acknowledges a European Union Fellowship to Japan.



## REFERENCES

- Altieri B. et al., 1999, *A&A*, 343, L65
- Aussel H., Cesarsky C.J., Elbaz D., Starck J.L., 1999, *A&A*, 342, 313
- Biviano et al., 2000, in: Mezure A., Le Fevre O., Le Brun V., eds., *ASP Conf.Ser.*, Clustering at High Redshifts, Astron.Soc.Pac., San Fransisco, p.101
- Condon J.J., 1974, *ApJ*, 188, 279
- Efstathiou A., Rowan-Robinson M., Siebenmorgen R., 2000, *MNRAS*, 313, 734
- Efstathiou A., Rowan-Robinson M., 2002, *MNRAS*, *submitted*
- Efstathiou,A. et al., 2000b, *MNRAS* 319, 1169
- Elbaz D, 2000, In: Lemke D, Stickel M.K. (Ed.)*ISO Surveys of a Dusty Universe*, Springer-Verlag, 121
- Flores H. et al., 1999, *A&A*, 343, 389
- Franceschini A., Toffolatti L., Danese L., De Zotti D., 1989, *ApJ*, 344, 35
- Franceschini A., Toffolatti L., Mazzei P., Danese L., De Zotti D., 1991, *A&AS*, 89, 285
- Gautier T.N., Boulanger F., Perault M., Puget J.L., 1992, *AJ*, 103, 1313
- Gruppioni C. et al., 1999, *MNRAS*, 305, 297
- Hacking P., Soifer B.T., 1991, *ApJ*, 367, L49

- Helou G., Beichman C.A., 1990, The confusion limits to the sensitivity of sub-mm telescopes, In: From Ground-Based to Space-Borne Sub-mm Astronomy, Proc. of the 29th Liege International Astrophysical Coll., ESA pub. 117
- Herbstmeier U. et al., 1998, A&A, 332, 739
- Hogg D., 2001, AJ, 121, 1207
- Hughes D. et al., 1998, Nature, 394, 241
- Jeong W.-S. et al. 2003, PASJ, 55, 717
- Jeong W.-S. et al. 2004, MNRAS, submitted
- Kawara K. et al., 1998, A&A, 336, L9
- Kiss Cs., Abraham P., Klaas U., Juvela M., Lemke D., 2001, A&A, 379, 1161
- Lagache G., Haffner L.M., Reynolds R.J., Tufte S.L., 2000a, A&A, 354, 247
- Lagache G., Puget J.L., 2000a, A&A, 355, 17
- Lagache G., Dole H., Puget J.L., 2003, MNRAS, 338, 555
- Lawrence A., Walker D., Rowan-Robinson M., Leech K.J., Penston M.V., 1986, MNRAS, 219, 687
- Low F.J. et al., 1984, ApJ 278, L19
- Matsuhara H. et al., 2000, A&A, 361, 407
- Oliver S.J. et al., 1997, MNRAS, 289, 471
- Pearson C.P., Rowan-Robinson M., 1996, MNRAS, 283, 174
- Pearson C.P., 2001, MNRAS 325, 1511 (CPP)
- Pearson C.P., Matsuhara H., Onaka T., Watarai H., Matsumoto T., 2001b, MNRAS, 999, 1014

- Pearson C.P. et al., 2004, MNRAS, 347, 1113
- Puget J.L. et al., 1999, A&A, 345, 29
- Rowan-Robinson M., Crawford P. 1989, MNRAS, 238, 523
- Rowan-Robinson M., 1995, MNRAS, 272, 737
- Rowan-Robinson M., 2001, ApJ, 549, 745
- Rush B., Malkan M., Spinoglio L., 1993, ApJSS, 89, 1
- Sanders D.B., Mirabel I.F., 1996, ARAA, 34, 725
- Saunders W., Rowan-Robinson M., Lawrence A., Efstathiou G., Kaiser N., Ellis, R.S., 1990, MNRAS, 242, 318
- Saunders W., et al., 2000, MNRAS, 317, 55
- Scheuer P.A., 1957, Proc. Cambridge Phil. Soc., 53, 764
- Scott S.E. et al., 2000, MNRAS, 331, 817
- Serjeant S.B.G. et al., 2000, MNRAS, 316, 768
- Smail I., Ivison R.J., Blain A.W., 1997, ApJ, 490, L5
- Takeuchi T.T., Ishii T.T., 2004, ApJ, 604, 40
- Vaisanen P., Tollestrup E.V., Fazio G.G., 2001, MNRAS, 325, 1241
- Xu C. et al., 2001, ApJ, 562, 179



# Chapter 8

## Conclusions

We have described the observing simulation for present or incoming infrared missions, e.g., Spitzer, ASTRO-F, Herschel, and SPICA. The algorithm and the method used in simulation are described in appendices A and B. In the observing simulation, a special care was taken by introducing the “Compiled PSF (Point Spread Function)” to optimise inevitable, but time-consuming, convolution processes. With the optimal algorithm, we reduce the computation time by an order of magnitude.

In chapter 2, we estimated the detection limits under various circumstances for ASTRO-F mission. We found that the readout noise is usually more important than the photon noise for dark patches of the sky by a factor of 1.3 to 2.5 in the case of a non-crowded source distribution. This means that the bright parts of the sky can be easily dominated by photon noise. The emission from the telescope is less than the interstellar background as long as the telescope temperature remains less than 6 K, but it could contribute significantly to the long-wavelength band if the temperature becomes larger than 6.5 K (see figure 2.4).

In crowded fields, source confusion becomes important in identifying sources. Our definition of the confusion-dominated detection limit from the photometry on the simulated images gives very similar values of the confusion limit based on a simple formula. The source confusion becomes larger than the detection limits by photon and readout noise only if the number of faint sources becomes much larger than a simple extension

of the IRAS source counts down to around 10 mJy, assuming no luminosity or density evolution. Recent models of source counts based on ISO and SCUBA observations (Matsuhara et al.(2000); Dole et al.(2001); Franceschini et al.(2001); Pearson(2001)), however, predict the source distribution that is subject to significant confusion at the longest wavelength band (WIDE-L). Other bands appear to be noise-limited. The source confusion also could change the slope in  $\log N$ - $\log S$  plots. The estimation with realistic source count model including the evolution model are described in chapter 7.

We have investigated the instrumental noise and the confusion in the far-infrared which are most important factors contributing to the detection limits. Since the detector used in far-infrared exhibit many characteristics, we have carried out simulations including transients, glitches and crosstalk effects for the detectors of ASTRO-F/FIS, as we described in chapter 4. Based upon simple models for these effects from laboratory measurements, the corrections were applied to the simulated time series data. Though we could accurately recover the input flux down to the detection limit, the actual behavior of the detector is affected by a combination of many detector characteristics that do not follow simple models.

In chapter 5, we have implemented the source count model by Rowan-Robinson (2001) in order to consider the realistic source distribution. The input model consists of a catalogue of extragalactic point sources generated from the luminosity function at  $60 \mu\text{m}$ , and a redshift distribution incorporating pure luminosity evolution ( $\Omega_0 = 1$ ,  $\Lambda = 0$ ). Source detection is mainly limited by photon and readout noise in the SW bands. Since the source confusion severely affects source detection in the LW bands due to the crowded beams, its limiting flux is not so different from that of the SW bands. We have obtained the expected source count results from the FIS survey and estimate the limiting redshift as  $\sim 2.5$  in the Wide-S band ( $75 \mu\text{m}$ ) and  $\sim 3$  in the Wide-L band ( $140 \mu\text{m}$ ).

In chapter 6, we generated a high resolution background map at other wavelengths based upon the observed  $100 \mu\text{m}$  dust map and the models of a dust spectrum. Using these simulated patches of the cirrus map, we estimated the sky confusion noise for various IR space missions such as ISO, Spitzer, ASTRO-F, Herschel and SPICA, through

statistical analysis. From the comparison with the results from ISO observation data, we found that the sky confusion noise estimated with our simulated patches are consistent with the ISO results. However, in the dark fields the sky confusion noise is less dependent upon the beam separation parameter than in the bright fields in the case of the ISO observation. We conclude that this is due to the dominant instrumental noise in the dark regions or alternatively, the CFIRB fluctuation. Since the CFIRB fluctuation strongly depends on the source distribution, we have discussed the contribution CFIRB in chapter 7. We also found that the sky confusion predicted from the IRAS data is significantly overestimated in the case of the large aperture telescopes, except in the dark fields.

For confirmation of our results through a realistic simulation, we performed photometry on simulated images including point sources with a sparse source distribution in order to avoid the effects of confusion due to crowded point sources. The detection limits obtained from the photometric analysis agree with the estimated sky confusion noise except for ISO and ASTRO-F. This discrepancy is due to the large detector pixel size compared with the FWHM of the beam size. We also obtained photometric results including the instrumental noise for ASTRO-F mission utilizing specific detailed information of the instruments. The estimated detection limits are consistent with the summation of the instrumental noise and the sky confusion noise.

We have estimated the sky confusion limits for point sources at mean and low sky brightness. We found that the sky confusion almost approaches  $5\sigma$  sensitivity level without confusion in the LW band of the ASTRO-F and Spitzer missions. Though the sky confusion does not severely affect the detection limits of Herschel mission, it can affect the detection limit of the SPICA mission because the SPICA mission will have a large aperture telescope cooled to very low temperatures in order to achieve exceptional sensitivity in the far-IR. However, since source confusion is also dominant noise source in the far-IR, we should compare sky confusion with source confusion with various source count models.

In chapter 7, we have probed both source confusion and sky confusion by using the generated source catalogue assuming a concordance cosmological world model

( $H_o = 72$ ,  $\Omega = 0.3$ ,  $\Lambda = 0.7$ ) for 2 evolutionary scenarios defined as the luminosity evolution model and burst evolution model of Pearson (2001) and Pearson et al. (2001), respectively. We also considered the sky confusion due to the cirrus as we discussed in chapter 6. Though the sky confusion is not a dominant noise source at high Galactic latitude, we should take into account the effects of sky confusion for large area survey. In addition, in order to segregate the CFIRB fluctuations, we need to analyze the fluctuation of cirrus emission even in high Galactic latitude regions.

We have investigated various definition for source confusion. Based upon the fluctuation and the photometry on the simulated images, we found the best estimator for source confusion. From our analysis of source confusion, we obtained source confusion limits of 10 mJy and 67 mJy at 70  $\mu\text{m}$  and 160  $\mu\text{m}$  for Spitzer mission, 25 mJy and 105 mJy at 75  $\mu\text{m}$  and 140  $\mu\text{m}$  for ASTRO-F mission, and 0.58 mJy and 10 mJy at 70  $\mu\text{m}$  and 160  $\mu\text{m}$  for Herschel & SPICA mission. At the limiting flux level, we have also obtained the expected redshift distribution for each source count model. ASTRO-F, Spitzer, Herschel & SPICA missions can discriminate whether source distribution follows the evolution model or not. However, higher resolution mission is required to distinguish two evolution models from the redshift distribution. Finally, we found that CFIRB can be resolved 87% and 65% at 70  $\mu\text{m}$  and 160  $\mu\text{m}$  by next generation infrared mission Herschel & SPICA.

# Appendix A

## Optimal Convolution

### A.1 Compiled PSF

#### A.1.1 PSF Convolution

The PSF of ASTRO-F/FIS, including the entire optical path, was computed using the ZEMAX optical simulation software package (Focus Software, Inc.). The resulting PSF at  $\lambda = 200 \mu\text{m}$  is shown in figure A.1, together with a circular aperture Airy pattern. The difference between the simulated PSF and the Airy pattern is very small, but noticeable. The simulated PSF is slightly narrower than the Airy pattern, and the side-lobe is more significant. Since FIS detectors do not lie on the optical axis of ASTRO-F, the PSF is slightly elongated with an ellipticity of  $\sim 0.05$ , but we assume the circular PSF in the present simulations. Since the FIS covers a wide range of wavelengths, the PSFs have been computed from 40 to 200  $\mu\text{m}$  at 5  $\mu\text{m}$  intervals. Except ASTRO-F/FIS mission, we use an ideal circular aperture Airy pattern corresponding to the aperture size of telescopes for the PSF of other missions.

Using the simulated PSF, we first obtain the PSF-convolved image  $I_{\lambda,i}$  on the focal plane at wavelength  $\lambda$ , contributed solely by the  $i$ -th point source:

$$I_{\lambda,i}(\mathbf{r}) = F_{\lambda,i} h_{\lambda}(\mathbf{r}; \mathbf{r}'_i) \quad (\text{A.1})$$

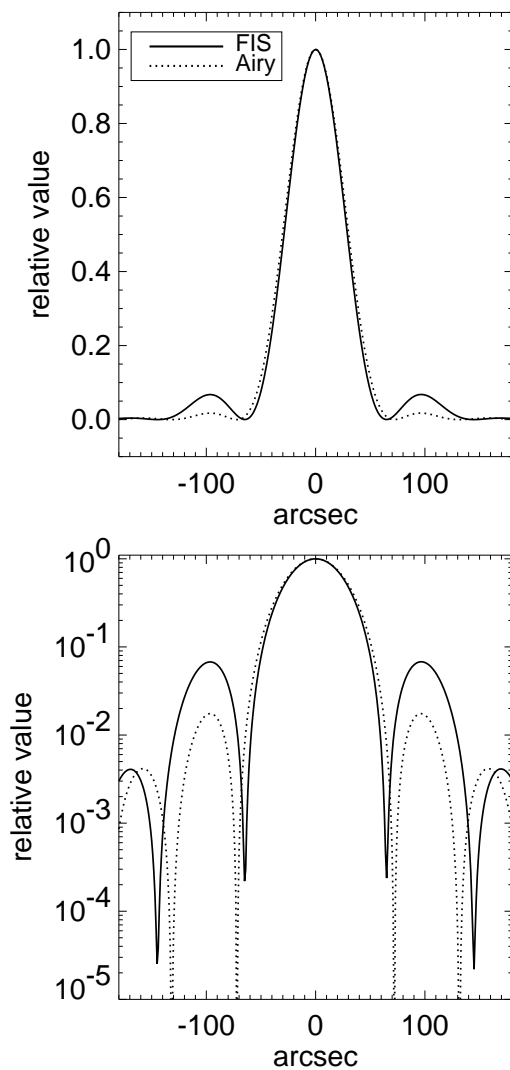


FIG. A.1: PSF of the ASTRO-F/FIS at  $200 \mu\text{m}$  in a linear scale (upper panel) and a logarithmic scale (lower panel). The solid line shows the PSF simulated by using ZEMAX and the dotted line shows the Airy pattern with the assumption of a single circular aperture system.

and

$$1 = \int_{\Omega} h_{\lambda}(\mathbf{r}; \mathbf{r}'_i) d\Omega, \quad (\text{A.2})$$

where  $\mathbf{r}$  is the position vector on the focal plane,  $F_{\lambda,i}$  is the flux density (at the wavelength  $\lambda$ ) of the  $i$ -th source, and  $h_{\lambda}(\mathbf{r}; \mathbf{r}'_i)$  is the simulated PSF at wavelength  $\lambda$  located centered at the position of the  $i$ -th source  $\mathbf{r}'_i$ . The PSF is normalised in such a way that the integration over the entire solid angle becomes unity. The intensity distribution on the focal plane,  $I_{\lambda}(\mathbf{r})$ , can then be obtained by

$$I_{\lambda}(\mathbf{r}) = \sum_i F_{\lambda,i} h_{\lambda}(\mathbf{r}; \mathbf{r}'_i). \quad (\text{A.3})$$

### A.1.2 Filter Transmittance and Detector Response

As the detector sweeps the sky, it integrates the charge generated by photons that fall onto the detector. For a given intensity distribution on the focal plane,  $I_{\lambda}(\mathbf{r})$ , the power,  $P_{\lambda}(\mathbf{r})$ , at the wavelength interval  $d\lambda$  is

$$P_{\lambda}(\mathbf{r})d\lambda = \int_{\Omega_{\text{pixel}}} I_{\lambda}(\mathbf{r}) A_{\text{tel}} \tau(\lambda) d\Omega d\lambda, \quad (\text{A.4})$$

where  $A_{\text{tel}}$  is the effective collecting area of the telescope, and  $\tau(\lambda)$  is the filter transmittance along the photon path within FIS (Takahashi et al.(2000)). The integration is performed over the solid angle subtended by the pixel.

The detector transforms the photons into charges. The total charge,  $D$ , integrated from  $t_1$  to  $t_2$  is

$$D(t_1 \rightarrow t_2) = \int_{\lambda} \int_{t_1}^{t_2} P_{\lambda}(\mathbf{r}(t)) \xi(\lambda) dt d\lambda, \quad (\text{A.5})$$

where  $\xi(\lambda)$  is the detector response function in units of  $\text{A W}^{-1}$ . We use the following convention:

$$\xi(\lambda) \equiv \xi_0 \tilde{\xi}(\lambda), \quad (\text{A.6})$$

where  $\xi_0$  is a constant in units of  $\text{A W}^{-1}$  and  $\tilde{\xi}$  is a function normalised to unity at the peak value for SW (short wavelength) and LW (long wavelength) detectors.

The normalised detector response functions,  $\tilde{\xi}$ , of LW and SW bands are shown in figures A.2 and A.3, respectively. We use these curves and the measured detector responsivity,  $\xi_r$ , to determine the normalisation constant,  $\xi_0$ . Measurements are done using a blackbody source, a filter that cuts off the photons below a certain wavelength, a Winston cone, and a detector in a perfectly reflecting cavity. The LW detector has long wavelength cut-off at 200  $\mu\text{m}$  and SW detector at 110  $\mu\text{m}$ . A low-pass filter was used to cut off the photons at wavelength below the FIS band. The short wavelength limits were 140  $\mu\text{m}$  for the LW detector and 40  $\mu\text{m}$  for the SW detector. The measured responsivity is represented by

$$\xi_r = \xi_0 \frac{\int_{\lambda} \tilde{\xi}(\lambda) B_{\lambda}(T) d\lambda}{\int_{\lambda} B_{\lambda}(T) d\lambda}, \quad (\text{A.7})$$

where  $B_{\lambda}(T)$  is the Planck function at the temperature  $T$ . In this estimation, we use  $T = 40$  K. From the measured value of  $\xi_r \approx 20 \text{ A W}^{-1}$  for LW, and  $\xi_r \approx 7 \text{ A W}^{-1}$  for SW, we can determine the normalisation constant,  $\xi_0$ . The normalisation constants are  $\xi_0 = 30 \text{ A W}^{-1}$  for the LW and  $\xi_0 = 10 \text{ A W}^{-1}$  for the SW detectors, respectively.

In the case of Herschel and SPICA missions, the detailed hardware specifications of each mission are not determined yet. Therefore, we do not try the calculation of noise for other missions except ASTRO-F/FIS. For Spitzer mission, we only consider the total response function (see figure A.4).

### A.1.3 Improved PSF Convolution

#### PSF Convolution

In observing simulation, we perform two convolution: PSF convolution and the pixel convolution in the scanning procedure. We modified the part of PSF convolution by using the FFT convolution. The FFT convolution is performed through frequency-domain multiplication by the product of their frequency domain functions Press et al. 1992. We call the convolution used in previous simulation ‘conventional method’ in this document.

Using the known positions, we assign fluxes to the grid points. In order to reduce

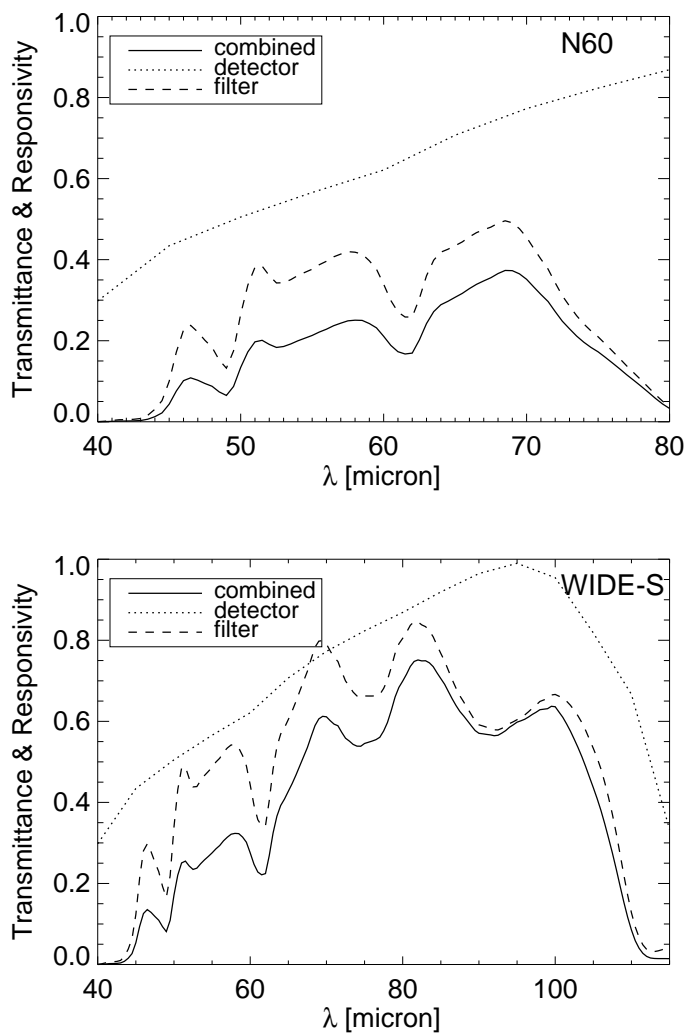


FIG. A.2: Filter transmission,  $\tau(\lambda)$ , (dashed lines) and the detector's response function,  $\tilde{\xi}(\lambda)$ , (dotted lines) for the N60 band (upper) and the Wide-S band (lower). The combined responsivities are shown as solid lines in arbitrary units.

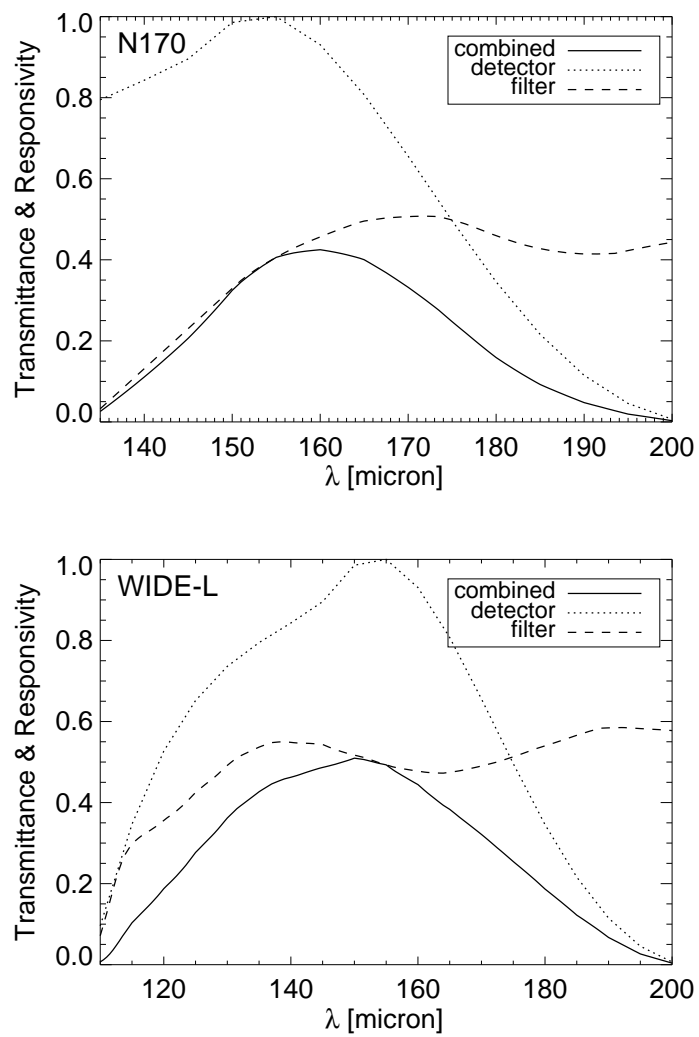


FIG. A.3: Same as figure A.2, except for the N170 band (upper) and the WIDE-L band (lower).

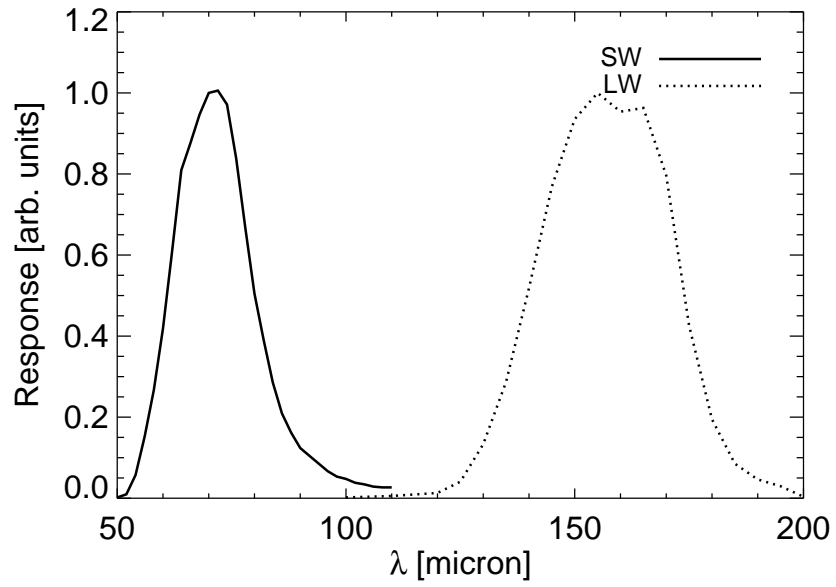


FIG. A.4: Total response function for Spitzer mission. Filter transmittance and the detector's response function are included.

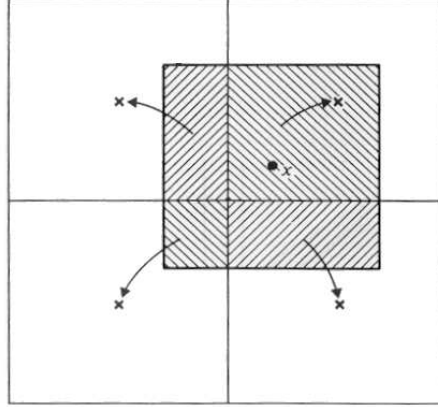


FIG. A.5: CIC (Cloud-In-Cell) scheme used in FFT convolution. In assigning the flux in some position, we calculate the flux at the neighboring grid points.

the position error in assigning the flux, we thus find the ‘flux field’ at the neighboring grid points. To assign fluxes to the grid points, the Cloud-In-Cell (CIC) interpolation scheme is used Hockney & Eastwood 1988 (see Fig. A.5).

### Computation Time

The computation time mainly depends on the number of sources and the size of PSF array in the conventional method. We use the same size of image array for various source distribution model and exclude the computation time to perform a image reconstruction. As the number of sources are increasing, the PSF convolution takes much more time in total process.

In the case of the FFT convolution, the computation time are mainly dependent of the size of the image to convolve PSF and the number of SED. We have to perform the FFT convolution to the image for each Compiled PSF repeatedly because we use different Compiled PSF for each type of SED.

We improved the performance of the PSF-convolution by using the FFT convolution and CIC interpolation scheme. We have totally reduced the computation time by 30 ~ 70%.

### A.1.4 Compiled PSF

If we use the same spectral energy distribution (SED) for each source, the flux density of the source can be defined as

$$F_{\lambda,i} = \mathcal{F}_i S_\lambda, \quad (\text{A.8})$$

where  $S_\lambda$  is the spectral energy distribution (SED) normalised to unity over the wavelength band and  $\mathcal{F}_i$  is the flux integrated over the bandwidth. We can rewrite equation (A.3) as

$$I_\lambda(\mathbf{r}) = \sum_i \mathcal{F}_i S_\lambda h_\lambda(\mathbf{r}; \mathbf{r}'_i). \quad (\text{A.9})$$

Since  $\lambda$  is independent of  $\mathbf{r}$  and  $\mathbf{r}'_i$ , we can introduce a new function,  $H(\mathbf{r}; \mathbf{r}'_i)$ , by integrating over the wavelength as

$$H(\mathbf{r}; \mathbf{r}'_i) = A_{\text{tel}} \int_\lambda h_\lambda(\mathbf{r}; \mathbf{r}'_i) S_\lambda \tau(\lambda) \xi(\lambda) d\lambda. \quad (\text{A.10})$$

We define this  $H(\mathbf{r}; \mathbf{r}'_i)$  as the ‘Compiled PSF’. If we perform convolution to the image plane by using this Compiled PSF, we can avoid repeated wavelength integration. Finally, equation (A.5) can be rewritten as

$$D(t_1 \rightarrow t_2) = \int_{t_1}^{t_2} \int_{\Omega_{\text{pixel}}} \sum_i \mathcal{F}_i H(\mathbf{r}; \mathbf{r}'_i) d\Omega dt. \quad (\text{A.11})$$

This concept of the Compiled PSF is effective only when the number of SED type is limited. The calculation time is reduced by a factor of  $N_\lambda$  by using the Compiled PSF, where  $N_\lambda$  is the number of wavelength grids. With a wavelength interval of  $\Delta\lambda = 5 \mu\text{m}$ , a typical  $N_\lambda$  lies between 10 and 20. In order to carry out simulations over four square degrees in the WIDE-S band, we need about 15 hours of computing time with Pentium IV 1 GHz machines. By introducing Compiled PSF, we can accomplish such a simulation within an hour.

### A.1.5 Spectral Energy Distribution of the Sources

We expect that the majority of faint point sources detected by present/next infrared missions will be external galaxies. Each object will have its own SED, but most

extragalactic point sources in the infrared band can be classified into four types of galaxies, i.e., the cirrus type representing typical spiral galaxies, the M 82 type starbursts, the Arp 220 type starbursts and the AGN dust torus type (Rowan-Robinson 2001). Four Compiled PSFs are required to accommodate these four types of SEDs in the simulations. The observed SEDs are further affected by the redshifts. We need redshifted-dependent SEDs for each type of source.

We expect that the Compiled PSF will be changed with the SED types and the redshift for wide bands, but the difference was found to be very small, even for the WIDE-S and WIDE-L bands, as shown in figure A.6. Since our main purpose is to examine the general performance of the ASTRO-F/FIS, we concentrate on simple models for the nature of the sources. We will deal with the SED types of sources, redshift distributions, and the luminosity function in the next paper in order to understand the cosmological model and the galaxy evolution through the observing simulation. Though the difference between the Compiled PSFs computed from the flat SED and other SEDs is severe at some extreme cases ( $\sim 10\%$  difference over the area), we use the Compiled PSF computed for galaxies with the flat SED in section 2 (i.e.,  $F_\lambda = \text{constant}$ ) (see figure A.6). In the flat SED's case, the Compiled PSF does not depend on the redshift.

In order to check the difference of the Compiled PSF over the SED and redshift, we plot the variation of FWHM for each SED in figures A.8-A.9. The variation depends on the shape of the SED of galaxy type and the total response curve. Since the shape of total response curve is more variant than that of Spitzer mission, the variation of FWHM for ASTRO-F/FIS mission is larger than that for Spitzer mission.

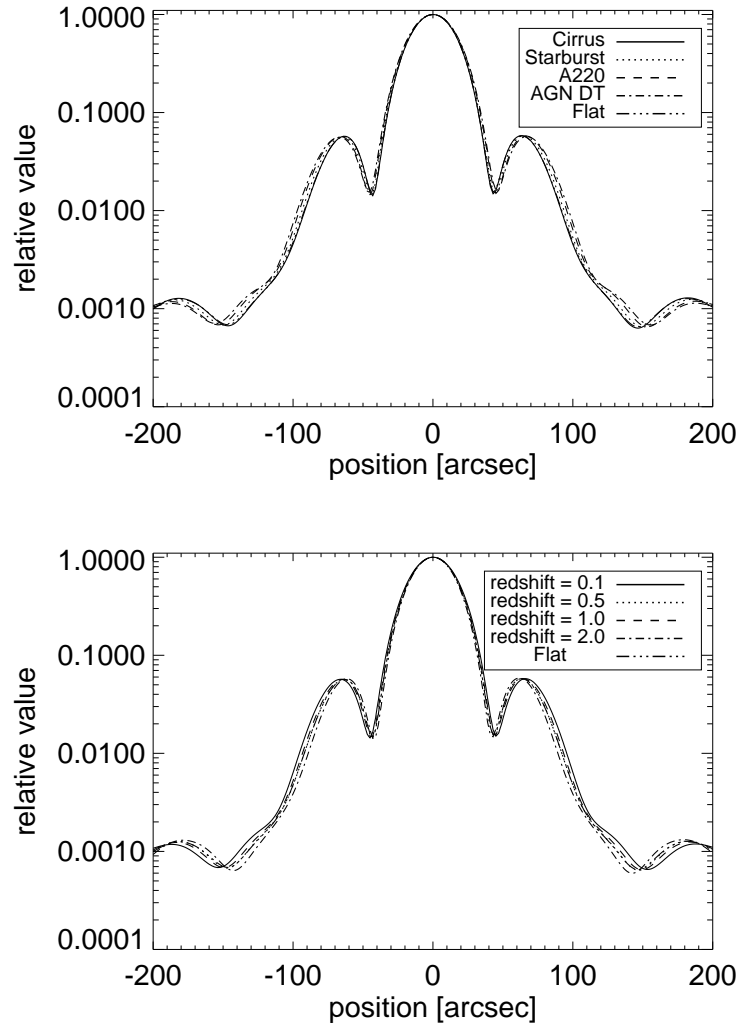


FIG. A.6: Normalised Compiled PSFs in the WIDE-L band. The upper panel is the Compiled PSFs over SED for redshift 1.0 and the lower panel is the Compiled PSFs over redshift for the cirrus type. For a comparison, we also plot the Compiled PSF computed for galaxies with the flat SED used in this work.

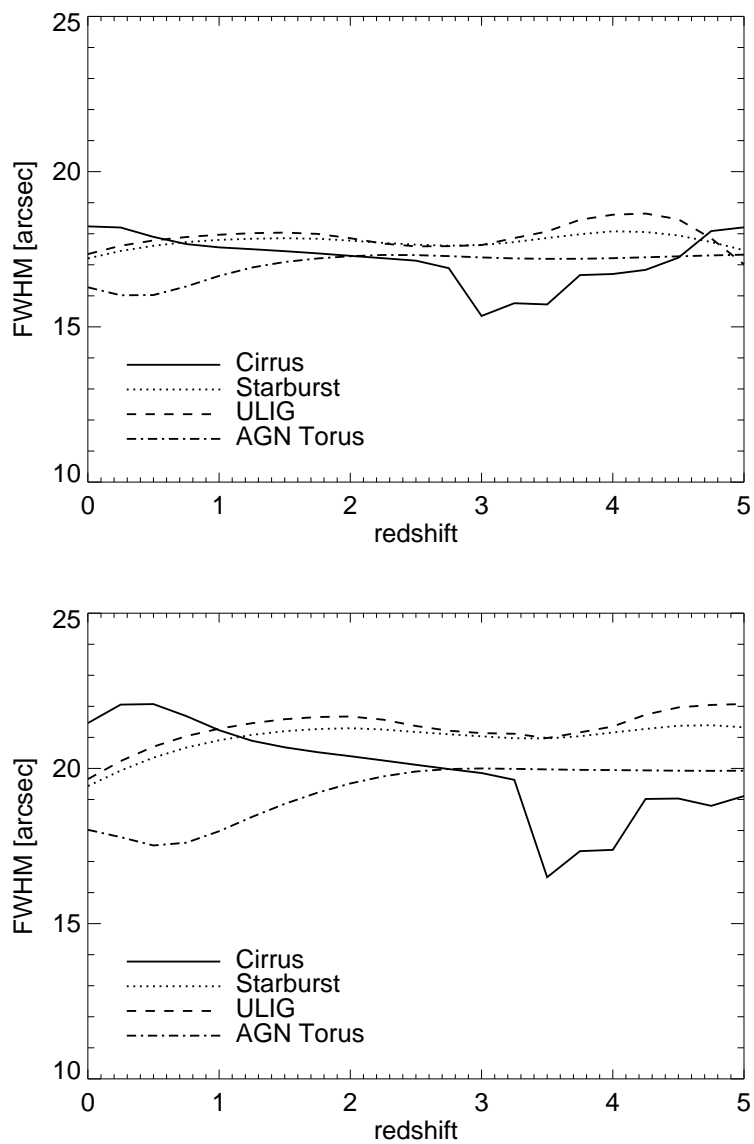


FIG. A.7: Variation of FWHM for ASTRO-F/FIS mission. N60 (upper) and Wide-S (lower) are shown.

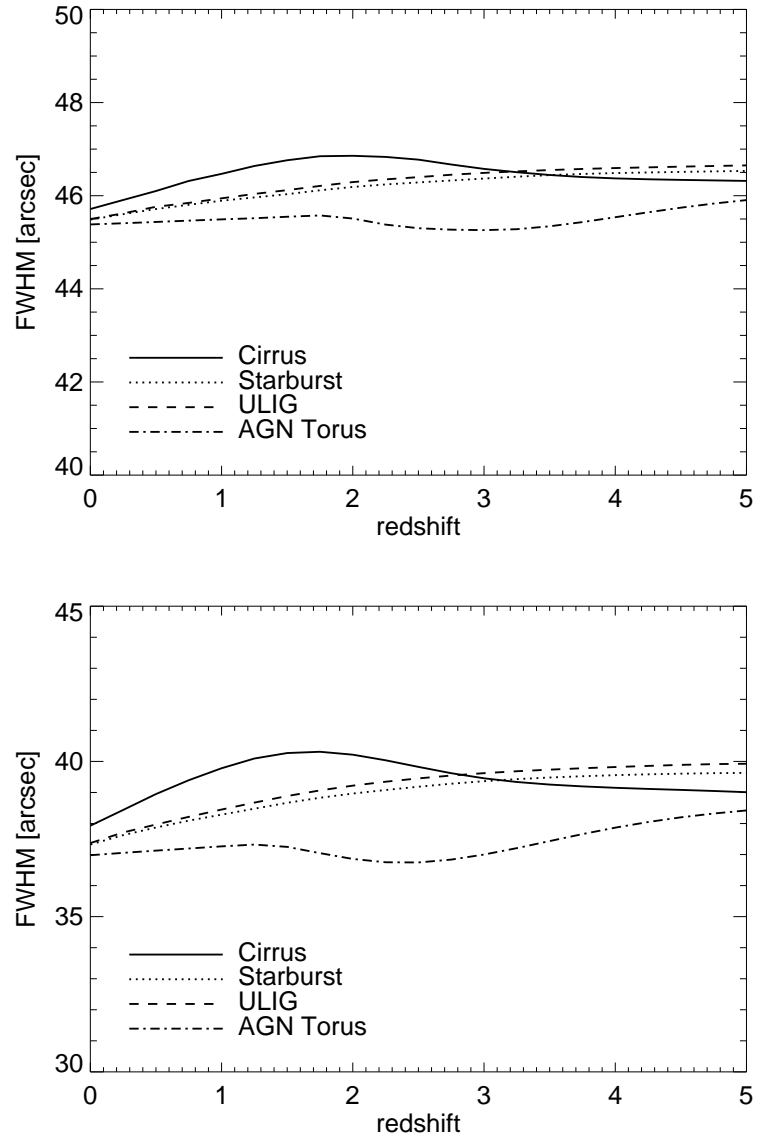


FIG. A.8: Variation of FWHM for ASTRO-F/FIS mission. N170 (lower-left) and Wide-L (lower-right) bands are shown.

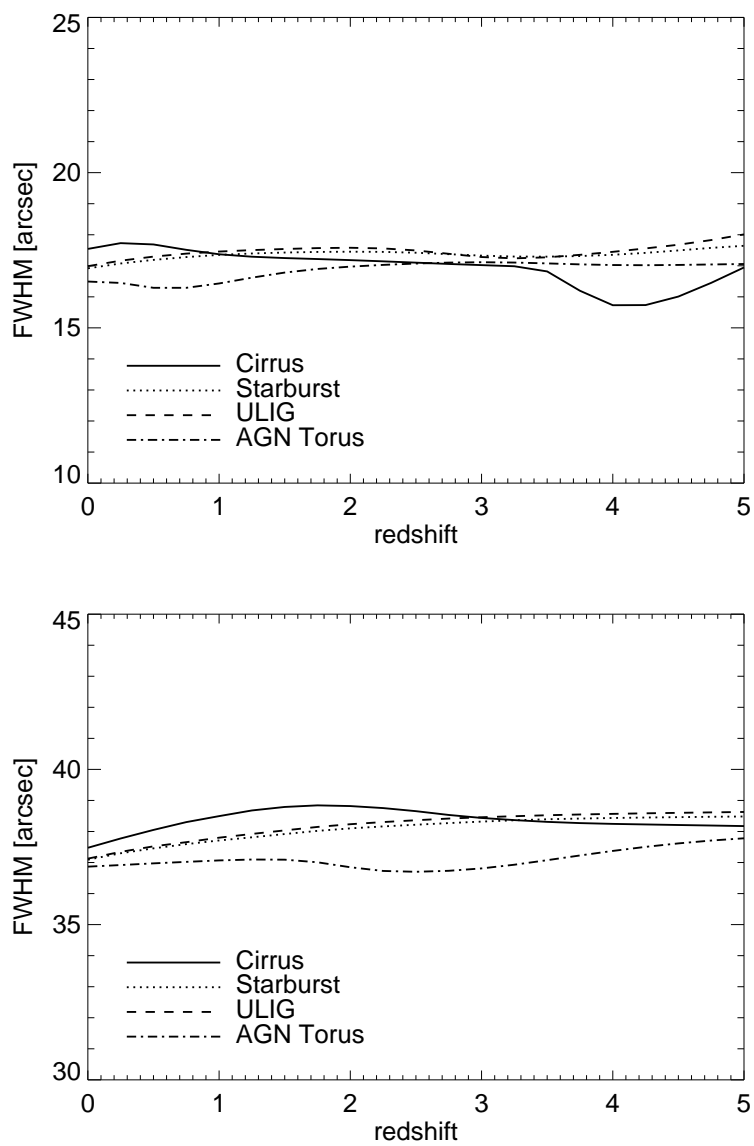


FIG. A.9: Variation of FWHM for Spitzer mission. SW (left) and LW (right) bands are shown.

# Appendix B

## Simulation for Scan Mode Observation

### B.1 Procedures of Scanning and Data Sampling

A PSF-convolved image is generated on grids where the scanning procedure is performed. To scan a PSF-convolved image, we need to know the position of the detector pixels. We set the array of the starting point to scan on the  $x$  (cross-scan direction) and the  $y$  (in-scan direction) frame in the image. The FIS detector arrays have 2 or 3 rows and 15 or 20 columns, and is tilted by an angle  $\theta = 26.^\circ 5$  from the cross-scan direction in order to assure Nyquist sampling (Takahashi et al.(2000); Matsuura et al.(2001)). We denote  $i$  as the index for the sampling sequence, and  $j$  and  $k$  as the indices for the row and column of the detector array, respectively (see figure B.1). By denoting  $(x_0, y_0)$  as the position vector of the center of upper left pixel of the array at the beginning of the scan (i.e.,  $i = j = k = 0$ ), we have the following formulae for the position vectors of the  $(j, k)$  pixel at the  $(i + 1)$ -th sampling:

$$x(i, j, k) = x_0 + p(k \cos \theta + j \sin \theta) \quad (\text{B.1})$$

and

$$y(i, j, k) = y_0 + i v \Delta t + p(j \cos \theta - k \sin \theta), \quad (\text{B.2})$$

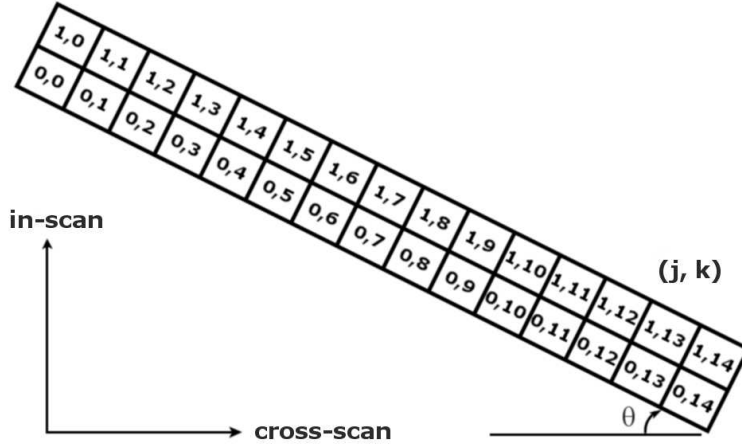


FIG. B.1: Layout of the detector array for the N170 band and definition of the scan directions.

where  $p$  is the size of the pixel pitch (see table 2.1),  $v$  is the scanning angular speed (which is  $3.60 \text{ arcmin s}^{-1}$ ) of the satellite, and  $\Delta t$  is the increment of the detector motion in the scan direction during the sampling interval. Note that the  $x$  position of each pixel does not depend on  $i$  in this coordinate system. We show one example for the passage of the detector in figure B.2.

## B.2 Integrating over the Detector Pixel

The integration of equation (A.11) over  $\Omega_{\text{pixel}}$  was carried out by summing up the image convolved with Compiled PSF on fine grids. The image convolved with Compiled PSF was constructed on grids of  $4''$  resolution, but the accuracy of the  $\Omega_{\text{pixel}}$  integration was not good enough on such grids ( $\sim$  a few percent error), partly because of the tilted configuration of the detector arrays. In order to improve the accuracy of the integration, we laid finer grids over the area where the integration would be performed. We were able to reduce the integration error down to 1% by taking a three-times finer grid over the integration area. If we use a smaller grid, we can improve the accuracy

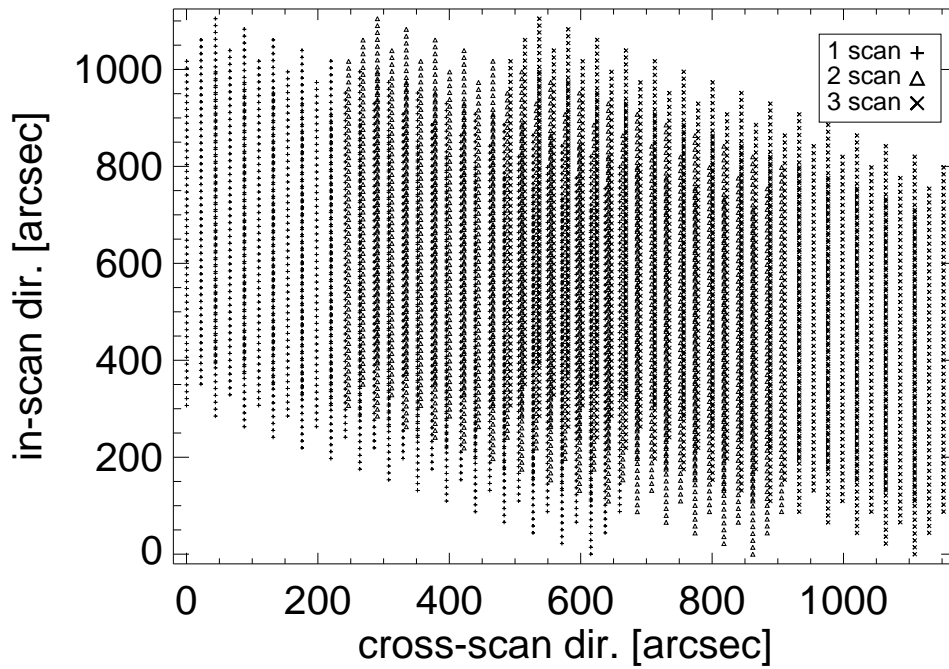


FIG. B.2: Passage of the detector for the WIDE-L band. We display the footprints of the detector pixels scanned three times.

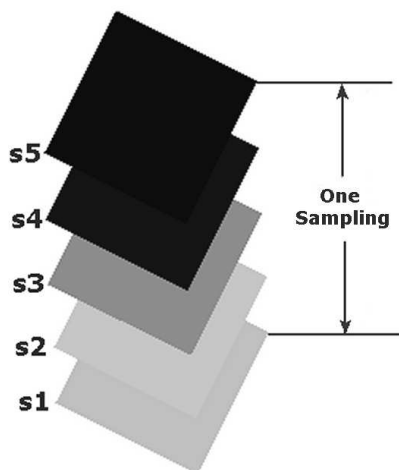


FIG. B.3: Each sampling is composed of several subsamples in order to ensure accurate integration over the region where the intensity varies. s1–s5 mean the subsamples. In actual simulations, we used only two subsamples.

of the flux and the position further, but we would need more computing time.

The time integration of equation (A.11) was made by dividing one sampling interval to shorter subsampling intervals in order to mimic the continuous scanning of the detector and applying the trapezoidal rule to the subsampled time series data. As the detector moves, one detector pixel integrates the signal during the subsample interval (see figure B.3). The number of subsample determines the resolution of integrated signal values. The sampling rate of 15.2 Hz for LW bands corresponds to  $14''.2$  which is much smaller than the pixel size, and we found that we need only two subsamples to ensure the integration accuracy over time becomes smaller than 1%.